**ISSN** 1949-8470 (online)

# World Journal of *Radiology*

*World J Radiol* 2015 November 28; 7(11): 361-420

Published by Baishideng Publishing Group Inc

WJR World Journal of Radiology

A peer-reviewed, online, open-access journal of Radiology

# Editorial Board

2014-2017

The *World Journal of Radiology* Editorial Board consists of 365 members, representing a team of worldwide experts in radiology. They are from 36 countries, including Afghanistan (1), Argentina (2), Australia (5), Austria (7), Belgium (2), Brazil (8), Canada (6), Chile (1), China (43), Croatia (1), Denmark (4), Egypt (6), France (5), Germany (22), Greece (10), India (12), Iran (6), Ireland (2), Israel (3), Italy (47), Japan (13), Netherlands (1), New Zealand (1), Pakistan (1), Poland (2), Portugal (1), Serbia (1), Singapore (3), Slovakia (1), South Korea (18), Spain (4), Sweden (2), Switzerland (4), Thailand (1), Turkey (26), United Kingdom (11), and United States (82).

Yue-Qi Zhu, *Shanghai*

**Croatia**

*Goran Kusec, Osijek*

**Denmark**

Poul E Andersen, *Odense*
Lars J Petersen, *Aalborg*
Thomas Z Ramsoy, *Frederiksberg*
Morten Ziebell, *Copenhagen*

**Egypt**

Mohamed F Bazeed, *Mansoura*
Mohamed Abou El-Ghar, *Mansoura*
Reem HA Mohamed, *Cairo*
Mohamed R Nouh, *Alexandria*
Ahmed AKA Razek, *Mansoura*
Ashraf A Zytoon, *Shebin El-Koom*

**France**

Sabine F Bensamoun, *Compiègne*
Romaric Loffroy, *Dijon*
Stephanie Nougaret, *Montpellier*
Hassane Oudadesse, *Rennes*
Vincent Vinh-Hung, *Fort-de-France*

**Germany**

Henryk Barthel, *Leipzig*
Peter Bannas, *Hamburg*
Martin Beeres, *Frankfurt*
Ilja F Ciernik, *Dessau*
A Dimitrakopoulou-Strauss, *Heidelberg*
Peter A Fasching, *Erlanegn*
Andreas G Schreyer, *Regensburg*
Philipp Heusch, *Duesseldorf*
Sonja M Kirchhoff, *Munich*
Sebastian Ley, *Munich*
Adel Maataoui, *Frankfurt am Main*
Stephan M Meckel, *Freiburg*
Hans W Muller, *Duesseldorf*
Kay Raum, *Berlin*
Dirk Rades, *Luebeck*
Marc-Ulrich Regier, *Hamburg*
Alexey Surov, *Halle*
Martin Walter, *Magdeburg*
Axel Wetter, *Essen*
Christoph Zilkens, *Düsseldorf*

**Greece**

Panagiotis Antoniou, *Thessaloniki*
Nikos Efthimiou, *Athens*
Dimitris Karnabatidis, *Patras*
George Latsios, *Athens*
Stylianos Megremis, *Iraklion*
Alexander D Rapidis, *Athens*
Kiki Theodorou, *Larissa*
Ioannis A Tsalafoutas, *Athens*
Evanthia E Tripoliti, *Ioannina*
Athina C Tsili, *Ioannina*

**India**

Ritesh Agarwal, *Chandigarh*
Chandan J Das, *New Delhi*
Prathamesh V Joshi, *Mumbai*
Naveen Kalra, *Chandigarh*
Chandrasekharan Kesavadas, *Trivandrum*
Jyoti Kumar, *New Delhi*
Atin Kumar, *New Delhi*
Kaushala P Mishra, *Allahabad*
Daya N Sharma, *New Delhi*
Binit Sureka, *New Delhi*
Sanjay Sharma, *New Delhi*
Raja R Yadav, *Allahabad*

**Iran**

Majid Assadi, *Bushehr*
SeyedReza Najafizadeh, *Tehran*
Mohammad Ali Oghabian, *Tehran*
Amir Reza Radmard, *Tehran*
Ramin Sadeghi, *Mashhad*
Hadi Rokni Yazdi, *Tehran*

**Ireland**

Tadhg Gleeson, *Wexford*
Frederik JAI Vernimmen, *Cork*

**Israel**

Dafna Ben Bashat, *Tel Aviv*
Amit Gefen, *Tel Aviv*
Tamar Sella, *Jerusalem*

**Italy**

Adriano Alippi, *Rome*
Dante Amelio, *Trento*
Michele Anzidei, *Rome*
Filippo F Angileri, *Messinas*
Stefano Arcangeli, *Rome*
Roberto Azzoni, *San Donato milanese*
Tommaso V Bartolotta, *Palermo*
Tommaso Bartalena, *Imola*
Livia Bernardin, *San Bonifacio*
Federico Boschi, *Verona*
Sergio Casciaro, *Lecce*
Emanuele Casciani, *Rome*
Musa M Can, *Napoli*
Alberto Cuocolo, *Napoli*
Michele Ferrara, *Coppito*
Mauro Feola, *Fossano*
Giampiero Francica, *Castel Volturno*
Luigi De Gennaro, *Rome*
Giulio Giovannetti, *Pisa*
Francesca Iacobellis, *Napoli*
Formato Invernizzi, *Monza Brianza*
Francesco Lassandro, *Naples*
Lorenzo Livi, *Florence*
Pier P Mainenti, *Napoli*
Laura Marzetti, *Chieti*
Giuseppe Malinverni, *Crescentino*
Enrica Milanesi, *Turin*
Giovanni Morana, *Treviso*
Lorenzo Monti, *Milan*
Silvia D Morbelli, *Genoa*
Barbara Palumbo, *Perugia*
Cecilia Parazzini, *Milan*
Stefano Pergolizzi, *Messina*
Antonio Pinto, *Naples*
Camillo Porcaro, *Rome*
Carlo C Quattrocchi, *Rome*
Alberto Rebonato, *Perugia*
Giuseppe Rizzo, *Rome*
Roberto De Rosa, *Naples*
Domenico Rubello, *Rovigo*
Andrea Salvati, *Bari*
Sergio Sartori, *Ferrara*
Luca M Sconfienza, *Milano*
Giovanni Storto, *Rionero*
Nicola Sverzellati, *Parma*
Alberto S Tagliafico, *Genova*
Nicola Troisi, *Florence*

**Japan**

Yasuhiko Hori, *Chiba*
Hidetoshi Ikeda, *Koriyama*
Masahito Kawabori, *Sapporo*
Tamotsu Kamishima, *Sapporo*
Hiro Kiyosue, *Yufu*
Yasunori Minami, *Osaka-sayama*
Yasuhiro Morimoto, *Kitakyushu*
Satoru Murata, *Tokyo*
Shigeki Nagamachi, *Miyazaki*
Hiroshi Onishi, *Yamanashi*
Morio Sato, *Wakayama Shi*
Yoshito Tsushima, *Maebashi*
Masahiro Yanagawa, *Suita*

**Netherlands**

Willem Jan van Rooij, *Tilburg*

**New Zealand**

W Howell Round, *Hamilton*

**Pakistan**

Wazir Muhammad, *Abbottabad*

**Poland**

Maciej S Baglaj, *Wroclaw*

Piotr Czauderna, *Gdansk*

**Portugal**

Joao Manuel RS Tavares, *Porto*

**Serbia**

Olivera Ciraj-Bjelac, *Belgrade*

**Singapore**

Gopinathan Anil, *Singapore*
Terence KB Teo, *Singapore*
Cher Heng Tan, *Singapore*

**Slovakia**

Stefan Sivak, *Martin*

**South Korea**

Ki Seok Choo, *Busan*
Seung Hong Choi, *Seoul*
Dae-Seob Choi, *Jinju*
Hong-Seok Jang, *Seoul*
Yong Jeong, *Daejeon*
Chan Kyo Kim, *Seoul*
Se Hyung Kim, *Seoul*
Joong-Seok Kim, *Seoul*
Sang Eun Kim, *Seongnam*
Sung Joon Kwon, *Seoul*
Jeong Min Lee, *Seoul*
In Sook Lee, *Busan*
Noh Park, *Goyang*
Chang Min Park, *Seoul*
Sung Bin Park, *Seoul*
Deuk Jae Sung, *Seoul*
Choongsoo Shin, *Seoul*
Kwon-Ha Yoon, *Iksan*

**Spain**

Miguel A De Gregorio, *Zaragoza*
Antonio Luna, *Jaén*
Enrique Marco de Lucas, *Santander*
Fernando Ruiz Santiago, *Granada*

**Sweden**

Dmitry Grishenkov, *Stockholm*
Tie-Qiang Li, *Stockholm*

**Switzerland**

Nicolau Beckmann, *Basel*
Christian Boy, *Bern*
Giorgio Treglia, *Bellinzona*

Stephan Ulmer, *Kiel*

**Thailand**

Sirianong Namwongprom, *Chiang Mai*

**Turkey**

Kubilay Aydin, *Istanbul*
Ramazan Akdemir, *Sakarya*
Serhat Avcu, *Ankara*
Ayse Aralasmak, *Istanbul*
Oktay Algin, *Ankara*
Nevbahar Akcar, *Meselik*
Bilal Battal, *Ankara*
Zulkif Bozgeyik, *Elazig*
Nazan Ciledag, Aakara
Fuldem Y Donmez, *Ankara*
Gulgun Engin, *Istanbul*
Ahmet Y Goktay, *Izmir*
Oguzhan G Gumustas, *Bursa*
Kaan Gunduz, *Ankara*
Pelin Ozcan Kara, *Mersin*
Kivanc Kamburoglu, *Ankara*
Ozgur Kilickesmez, *Istanbul*
Furuzan Numan, *Istanbul*
Cem Onal, *Adana*
Ozgur Oztekin, *Izmir*
Seda Ozbek (Boruban), *Konya*
Selda Sarikaya, *Zonguldak*
Figen Taser, *Kutahya*
Baran Tokar, *Eskisehir*
Ender Uysal, *Istanbul*
Ensar Yekeler, *Istanbul*

**United Kingdom**

Indran Davagnanam, *London*
M DC Valdés Hernández, *Edinburgh*
Alan Jackson, *Manchester*
Suneil Jain, *Belfast*
Long R Jiao, *London*
Miltiadis Krokidis, *Cambridge*
Pradesh Kumar, *Liverpool*
Peter D Kuzmich, *Derby*
Georgios Plataniotis, *Brighton*
Vanessa Sluming, *Liverpool*

**United States**

Garima Agrawal, *Saint Louis*
James R Brasic, *Baltimore*
Rajendra D Badgaiyan, *Buffalo*
Ulas Bagci, *Bethesda*
Anat Biegon, *Stony Brook*
Ramon Casanova, *Winston Salem*
Wenli Cai, *Boston*
Zheng Chang, *Durham*
Corey J Chakarun, *Long Beach*
Kai Chen, *Los Angeles*
Hyun-Soon Chong, *Chicago*
Marco Cura, *Dallas*
Ravi R Desai, *Bensalem*
Delia DeBuc, *Miami*
Carlo N De Cecco, *Charleston*
Timm-Michael L Dickfeld, *Baltimore*
Subba R Digumarthy, *Boston*
Huy M Do, *Stanford*
Todd A Faasse, *Grand Rapids*
Salomao Faintuch, *Boston*
Girish M Fatterpekar, *New York*
Dhakshinamoorthy Ganeshan, *Houston*
Robert J Griffin, *Little Rock*
Andrew J Gunn, *Boston*
Sandeep S Hedgire, *Boston*
Timothy J Hoffman, *Columbia*
Mai-Lan Ho, *San Francisco*
Juebin Huang, *Jackson*
Abid Irshad, *Charleston*
Matilde Inglese, *New York*
El-Sayed H Ibrahim, *Jacksonville*
Paul R Julsrud, *Rochester*
Pamela T Johnson, *Baltimore*
Ming-Hung Kao, *Tempe*
Sunil Krishnan, *Houston*
Richard A Komoroski, *Cincinnati*
Sandi A Kwee, *Honolulu*
King Kim, *Ft. Lauderdale*
Guozheng Liu, *Worcester*
Yiyan Liu, *Newark*
Venkatesh Mani, *New York*
Lian-Sheng Ma, *Pleasanton*
Rachna Madan, *Boston*
Zeyad A Metwalli, *Houston*
Yilong Ma, *Manhasset*
Hui Mao, *Atlanta*
Feroze B Mohamed, *Philadelphia*
Gul Moonis, *Boston*
John L Nosher, *New Brunswick*
Rahmi Oklu, *Boston*
Aytekin Oto, *Chicago*
Bishnuhari Paudyal, *Philadelphia*
Rajul Pandya, *Youngstown*
Chong-Xian Pan, *Sacramento*
Jay J Pillai, *Baltimore*
Neal Prakash, *Duarte*
Reza Rahbar, *Boston*
Ali S Raja, *Boston*
Gustavo J Rodriguez, *El Paso*
David J Sahn, *Portlsand*
Steven Schild, *Scottsdale*
Ali R Sepahdari, *Los Angeles*
Li Shen, *Indianapolis*
JP Sheehan, *Charlottesville*
Atul B Shinagare, *Boston*
Sarabjeet Singh, *Boston*
Charles J Smith, *Columbia*
Kenji Suzuki, *Chicago*
Monvadi Srichai-Parsia, *Washington*
Sree H Tirumani, *Boston*
Hebert A Vargas, *New York*
Sachit Verma, *Philadelphia*
Yoichi Watanabe, *Minneapolis*
Li Wang, *Chapel Hill*
Carol C Wu, *Boston*
Shoujun Xu, *Houston*
Min Yao, *Cleveland*
Xiaofeng Yang, *Atlanta*
Qingbao Yu, *Albuquerque*
Aifeng Zhang, *Chicago*
Chao Zhou, *Bethlehem*
Hongming Zhuang, *Philadelphia*

WJR World Journal of Radiology

Contents

Monthly Volume 7 Number 11 November 28, 2015

## REVIEW



## MINIREVIEWS



## ORIGINAL ARTICLE

### Case Control Study



### Observational Study

NAME OF JOURNAL
*World Journal of Radiology*

ISSN
ISSN 1949-8470 (online)

LAUNCH DATE
December 31, 2009

FREQUENCY
Monthly



EDITORIAL OFFICE
Jin-Lei Wang, Director
Xiu-Xia Song, Vice Director
*World Journal of Radiology*
Room 903, Building D, Ocean International Center,
No. 62 Dongsihuan Zhonglu, Chaoyang District,
Beijing 100025, China
Telephone: +86-10-59080039
Fax: +86-10-85381893
E-mail: editorialoffice@wjgnet.com
Help Desk: http://www.wjgnet.com/esps/helpdesk.aspx
http://www.wjgnet.com

PUBLISHER
Baishideng Publishing Group Inc
8226 Regency Drive,
Pleasanton, CA 94588, USA
Telephone: +1-925-223-8242
Fax: +1-925-223-8243
E-mail: bpgoffice@wjgnet.com
Help Desk: http://www.wjgnet.com/esps/helpdesk.aspx
http://www.wjgnet.com

PUBLICATION DATE
November 28, 2015



INSTRUCTIONS TO AUTHORS
Full instructions are available online at http://www.wjgnet.com/1949-8470/g_info_20100316162358.htm.

ONLINE SUBMISSION
http://www.wjgnet.com/esps/

World Journal of Radiology

Submit a Manuscript: http://www.wjgnet.com/esps/
Help Desk: http://www.wjgnet.com/esps/helpdesk.aspx
DOI: 10.4329/wjr.v7.i11.361

*World J Radiol* 2015 November 28; 7(11): 361-374
ISSN 1949-8470 (online)


REVIEW

# Role of magnetic resonance imaging in the detection and characterization of solid pancreatic nodules: An update

Najwa Al Ansari, Miguel Ramalho, Richard C Semelka, Valeria Buonocore, Silvia Gigli, Francesca Maccioni

Najwa Al Ansari, Valeria Buonocore, Silvia Gigli, Francesca Maccioni, Department of Radiological Sciences, Oncology and Pathology, Policlinico Umberto I Hospital Rome, Sapienza University of Rome, 00161 Rome, Italy

Miguel Ramalho, Department of Radiology, Hospital Garcia de Orta, 2801-951 Almada, Portugal

Miguel Ramalho, Richard C Semelka, Department of Radiology, University of North Carolina, Chapel Hill, NC 27599-7510, United States

Author contributions: All authors had contributed equally to this work in form of literature review, manuscript writing/editing, and figure collection/illustration/annotation/captioning.

Conflict-of-interest statement: There is no conflict of interest associated with any of the senior author or other co-authors contributed their efforts in this manuscript.



Correspondence to: Richard C Semelka, MD, Professor, Department of Radiology, University of North Carolina, UNC at Chapel Hill CB 7510 - 2001 Old Clinic Bldg., Chapel Hill, NC 27599-7510, United States. richsem@med.unc.edu
Telephone: +1-919-9669676
Fax: +1-919-8437147

Received: April 27, 2015
Peer-review started: April 28, 2015
First decision: August 4, 2015
Revised: September 8, 2015
Accepted: October 1, 2015
Article in press: October 8, 2015
Published online: November 28, 2015

## Abstract

Pancreatic ductal adenocarcinoma is the most common malignant tumor of the pancreas. The remaining pancreatic tumors are a diverse group of pancreatic neoplasms that comprises cystic pancreatic neoplasms, endocrine tumors and other uncommon pancreatic tumors. Due to the excellent soft tissue contrast resolution, magnetic resonance imaging (MRI) is frequently able to readily separate cystic from noncystic tumors. Cystic tumors are often easy to diagnose with MRI; however, noncystic non-adenocarcinoma tumors may show a wide spectrum of imaging features, which can potentially mimic ductal adenocarcinoma. MRI is a reliable technique for the characterization of pancreatic lesions. The implementation of novel motion-resistant pulse sequences and respiratory gating techniques, as well as the recognized benefits of MR cholangiopancreatography, make MRI a very accurate examination for the evaluation of pancreatic masses. MRI has the distinctive ability of non-invasive assessment of the pancreatic ducts, pancreatic parenchyma, neighbouring soft tissues, and vascular network in one examination. MRI can identify different characteristics of various solid pancreatic lesions, potentially allowing the differentiation of adenocarcinoma from other benign and malignant entities. In this review we describe the MRI protocols and MRI characteristics of various solid pancreatic lesions. Recognition of these characteristics may establish the right diagnosis or at least narrow the differential diagnosis, thus avoiding unnecessary tests or procedures and permitting better management.

**Key words:** Pancreatic nodules; Malignant; Lymphoma; Benign; Magnetic resonance imaging; Adenocarcinoma; Pancreas; Neuroendocrine; Solid pseudopapillary tumor; Metastases



**Core tip:** In addition to pancreatic ductal adenocarcinoma

other solid pancreatic lesions occur. Less common solid primary pancreatic tumors and non-neoplastic disease processes that may be diagnosed with relatively high specificity employing magnetic resonance imaging (MRI). The radiologist must be familiar with their MRI appearance to correctly diagnose them, or suggest them in the differential diagnosis when appropriate, since it may change substantially the approach, prognosis and patient management.

Al Ansari N, Ramalho M, Semelka RC, Buonocore V, Gigli S, Maccioni F. Role of magnetic resonance imaging in the detection and characterization of solid pancreatic nodules: An update. *World J Radiol* 2015; 7(11): 361-374 Available from: URL: http://www.wjgnet.com/1949-8470/full/v7/i11/361.htm DOI: http://dx.doi.org/10.4329/wjr.v7.i11.361

## INTRODUCTION

Pancreatic ductal adenocarcinoma is the most common malignant tumor of the pancreas, accounting for 85%-90% of all malignant pancreatic tumors and is the 4$^{th}$ most common cause of cancer death worldwide[1]. The remaining 10%-15% of pancreatic tumors is a varied group of neoplasms that comprises cystic pancreatic neoplasms, endocrine tumors and other uncommon pancreatic tumors. Magnetic resonance imaging (MRI) is reliable for the characterization of solid and cystic pancreatic lesions. Due to the excellent soft-tissue contrast resolution, MRI is able to readily separate cystic from noncystic tumors. Cystic tumors are frequently easier to diagnose since they often possess typical imaging findings allowing an accurate and reliable prospective diagnosis. Noncystic noncarcinoma tumors may show a wide spectrum of imaging features, which most often are distinct from the features of ductal adenocarcinoma. Infrequently they may possess features that simulate carcinoma, and therefore clinical history and laboratory parameters are always important to be aware of. In this review we describe the typical MRI characteristics of various solid pancreatic lesions, which will aid in differentiation of adenocarcinoma from other benign and malignant entities. Recognition of these characteristics often may establish the right diagnosis or at least narrow the differential diagnosis, which will allow better patient management and avoid unnecessary tests or procedures.

We herein describe the typical MRI findings of ductal adenocarcinoma, of less common solid primary pancreatic tumors, and of non-neoplastic disease processes that may simulate ductal adenocarcinoma.

## CLASSIFICATION OF PANCREATIC TUMORS

According to the World Health Organization classification, pancreatic tumors are classified depending on the cell lineage they arise from. The tumors may have an epithelial or nonepithelial origin.

Tumors with epithelial origin include the exocrine pancreas: (1) ductal cells, including ductal adenocarcinoma with its different histopathological variants, and mucinous and serous cystic tumors; (2) acinar cells, including acinar cell carcinoma (ACC) and mixed acinar-endocrine carcinoma; or (3) uncertain origin, including solid pseudopapillary tumor (SPT) and pancreatoblastoma or the endocrine pancreas (functioning and nonfunctioning tumors).

The nonepithelial tumors include neoplasms such as primary lymphoma and tumors of mesenchymal cell origin (hemangioma, lymphangioma, sarcoma, lipoma, *etc.*).

There are also nonpancreatic tumor lesions in origin that might involve the pancreas, including malignant lesions such as metastasis or secondary lymphoma, and benign lesions such as intrapancreatic splenule.

## MRI EVALUATION OF THE PANCREAS

MRI is a reliable technique for the characterization of pancreatic lesions. The implementation of novel motion-resistant pulse sequences and respiratory gating techniques, as well as the recognized benefits of MR cholangiopancreatography, make MRI a very accurate examination for the evaluation of pancreatic masses. MRI has the distinctive ability of non-invasive assessment of the pancreatic ducts, pancreatic parenchyma, neighbouring soft tissues, and vascular network in one examination.

MRI of the pancreas should be performed with state of the art scanners using high field strength (1.5T or 3T) units[2-4] with phased-array torso coils and parallel imaging to maximize signal to noise ratio and permit for superior spatial resolution and faster acquisition times.

3T systems allow higher spatial resolution and provide the highest post-contrast imaging quality and temporal resolution of the pancreas, which is important when evaluating small focal pancreatic lesions[4], and looking for vascular involvement or encasement.

The typical MRI protocol for the assessment of the pancreas commonly includes coronal and transverse T2-weighted single-shot echo train spin echo (SS-ETSE), transverse T2-weighted fat suppressed fast spin echo or SS-ETSE, transverse in-phase and out-of-phase T1-weighted spoiled gradient echo (GRE), and transverse T1-weighted fat suppressed three-dimensional (3D) GRE images, obtained before and after contrast injection during the late arterial, portal-venous and interstitial phases. Magnetic resonance cholangiopancreatography (MRCP) is routinely added to abdominal protocols to assess ductal obstruction, dilatation or luminal outline. This sequence combination provides comprehensive evaluation of a full range of pancreatic disease processes.

T2-weighted SS-ETSE sequences such as half-Fourier acquisition snapshot turbo spin-echo offer

anatomic display of the common bile duct (CBD) and pancreatic duct on coronal and transverse plane images. This sequence is important to evaluate fluid content, which most often allows clear separation of cystic and solid content lesions, as well as complications such as the assessment of the complexity of pancreatic fluid collections.

Pre- and post-contrast T1-weighted GRE sequences are typically obtained as a fat-suppressed 3D-GRE technique, allowing high-quality dynamic imaging of the pancreas. The main benefits of these sequences include the ability to obtain thinner slices (2-3 mm) and to perform multiplanar imaging, essential to assess and characterize focal pancreatic masses with < 1 cm in size and to evaluate diffuse pancreatic disease[3,5-10].

3D MRCP images are obtained in an oblique coronal projection following the plane of the main pancreatic duct, with the complementary benefit of being able to generate multiplanar maximum intensity projection and volume rendering imaging. This approach delineates longer segments of the pancreatic duct. MRCP depicts well the biliary and pancreatic ducts allowing optimal evaluation of ductal contour and dilatation, as well as abnormal duct pathways[7-9]. The combination of tissue imaging sequences and MRCP generate comprehensive information on pancreatic disease.

For the diagnosis of biliary disease, the secretin enhanced MRCP is routinely performed as part of the workup of patients with known or suspected pancreatic disease such as acute and chronic pancreatitis, congenital variants of the pancreaticoduodenal junction, and intraductal papillary mucinous neoplasms and follow-up of patients after pancreatectomy, in many centers. Secretin is well tolerated, and side effects are rarely seen[11-13].

MRI is a non-ionizing cross-sectional imaging method with a safer intra-venous contrast profile in comparison to computed tomography (CT). This is especially important in patients at higher risk of radiation injury (*e.g.*, younger patients) especially those requiring repeated imaging follow-up.

Some gadolinium based contrast agents (GBCAs) are associated with nephrogenic systemic fibrosis. Avoidance of GBCAs exposure is the best approach for high-risk patients[14] including patients with acute or advanced chronic kidney disease. Also, is has been reported that the incidence of immediate hypersensitivity reactions to MR GBCAs was 0.079%, and the recurrence rate of hypersensitivity reactions was 30% in patients with prior reactions[15]. It is a very low percentage if we compare it to iodinate contrast media but however it should be considered.

New motion-resistant MRI techniques provide adequate images even in patients that are not able to suspend respiration[16]. Preliminary studies demonstrated that in patients who unable to suspend respiration, new imaging techniques for MRI, such as radial 3D-GRE acquired in a free breathing fashion, may be useful for pancreatic MR imaging and aid the radiologist in the detection and characterization of pancreatic focal lesions.

Normal pancreatic parenchyma displays high T1 signal intensity due to the presence of aqueous protein[3,4], which is accentuated on fat-suppressed GRE sequences. The normal pancreas typically shows uniform hyperintense enhancement on arterial phase images, fading overtime to become isointense to the liver on interstitial phase images (Figure 1)[6,17].

In the elderly, the high T1 signal intensity of the pancreas may be diminished and be lesser than that of the liver, reflecting fibrosis resultant from the aging process[5].

### *Pancreatic ductal adenocarcinoma*

Ductal adenocarcinoma is the most common malignant pancreatic neoplasm and accounts for almost 90% of all malignant pancreatic tumors. Males are affected twice as often as women and the peak age of occurrence is in the 7$^{th}$ to 8$^{th}$ decades of life[18]. At clinical presentation, 2/3 of patients have an advanced tumor stage. This may justify why pancreatic adenocarcinoma shows a poor prognosis, with a 5-year survival rate of 5%[19]. Despite advances in patient management and new chemotherapy regimens, surgery remains the only curative treatment[19].

The appearance of the typical ductal adenocarcinoma is an irregular, small focal solid mass (2-3 cm) without necrosis or hemorrhage. It is a heterogeneous and poorly enhancing mass with a tendency for local infiltration, including vascular encasement.

Near 60%-70% of ductal adenocarcinomas of the pancreas involve the pancreatic head, 10%-20% are found in the body and 5%-10% in the tail. Diffuse pancreatic involvement occurs in 5% of the cases[20].

Spin-echo images are limited in the detection of pancreatic adenocarcinoma. On T2-weighted images, tumors are usually slightly hypointense relative to the background pancreatic parenchyma and consequently challenging to visualize. Ductal adenocarcinomas appear as low signal intensity lesions on noncontrast fat-suppressed T1-weighted images and usually well delineated from normal background pancreas, which is high in signal intensity[17,21-24].

Detection of adenocarcinoma is better performed on the arterial phase images, where the lesion will enhance to a lesser degree than the adjacent background pancreas (Figures 2 and 3), due to the abundant fibrous stroma and scarce tumor vascularity[23]. The increased volume of the extracellular space and the venous drainage of tumors compared to normal pancreatic tissue are responsible for the near isointense appearance of ductal adenocarcinoma on the interstitial phase[23].

In general, large pancreatic tumors tend to persist low in signal intensity (Figure 2) on interstitial phase images, whereas the signal intensity of smaller tumors is more variable and may range from hypointense to minimally hyperintense on this phase (Figure 3).

Obstruction of the main pancreatic duct by the pancreatic adenocarcinoma, which may be seen even

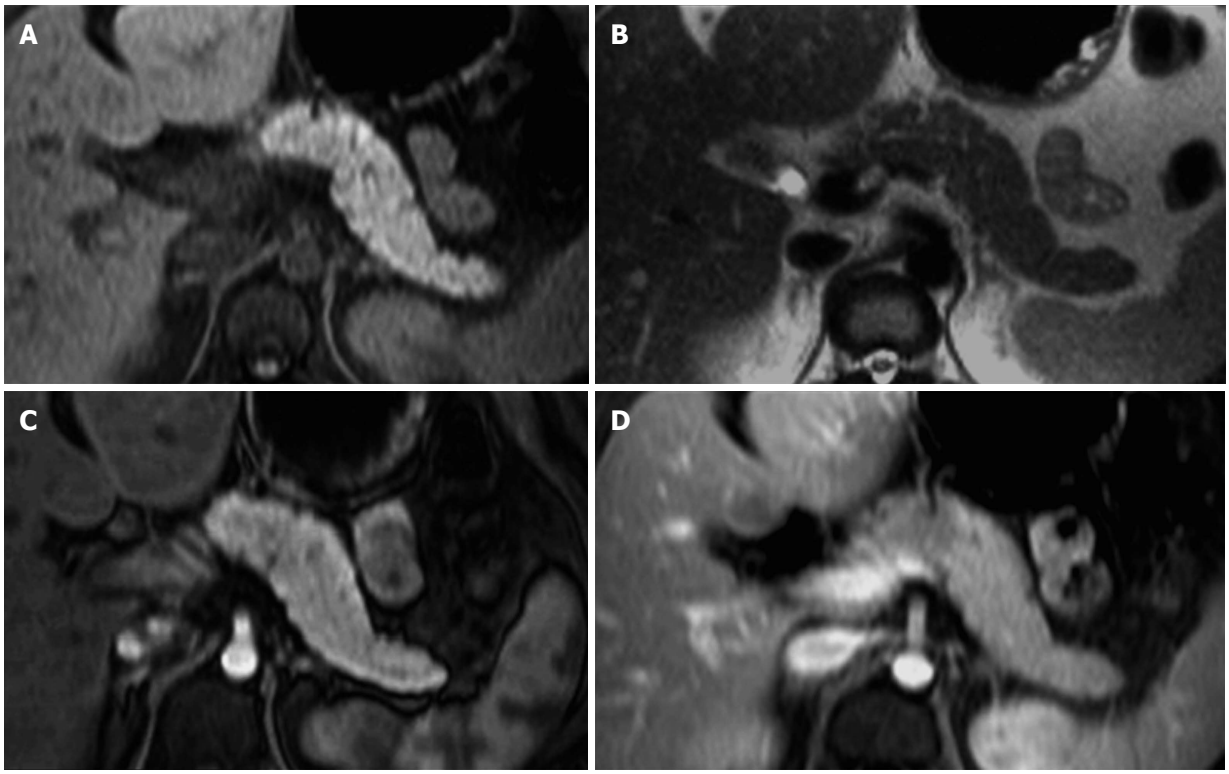


**Figure 1 Normal pancreas.** Axial T2-weighted SS-ETSE (A), pre-contrast fat-suppressed T1-weighted (B) GRE and post-gadolinium fat-suppressed T1-weighted gradient echo images acquired in the arterial (C) and venous (D) phases of enhancement. The normal pancreas is high in signal intensity on T1-weighted images (B) due to the presence of aqueous protein in the pancreatic acini. A uniform capillary blush is apparent on the immediate post-gadolinium image (C). T2-weighted sequences allow the depiction of the pancreatic duct. SS-ETSE: Single-shot echo train spin echo; GRE: Gradient echo.

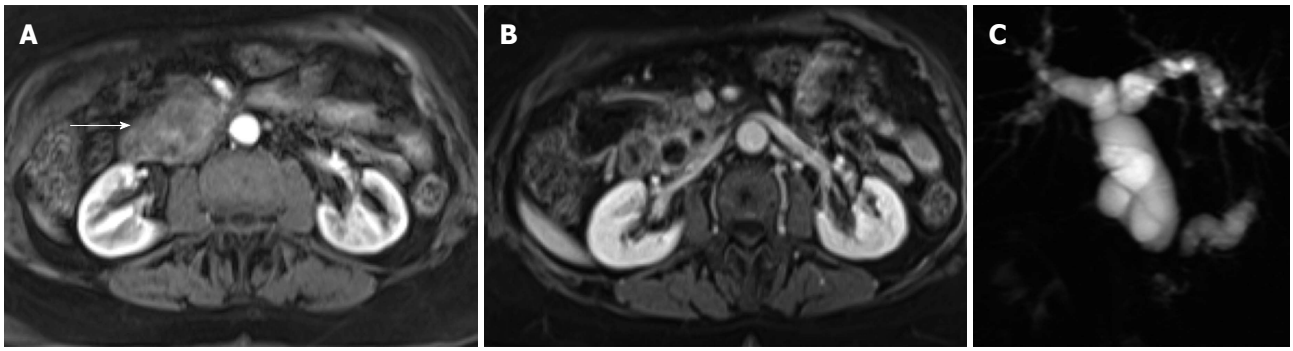


**Figure 2 Pancreatic ductal adenocarcinoma.** Axial post-gadolinium fat-suppressed T1-weighted images obtained in the arterial phase (A) and interstitial phase (B) image, and coronal maximum intensity projection image of MRCP (C). There is a hypovascular tumor arising in the pancreatic head (arrow, A) that obstructs the common bile duct and pancreatic duct (double duct sign). This sign is well depicted in the MRCP images (C). MRCP: Magnetic resonance cholangiopancreatography.

with small tumors, results in tumor-associated chronic pancreatitis. Many times, the pancreatic parenchyma distal to pancreatic adenocarcinoma is atrophic and low in signal intensity compared to normal pancreas, due to chronic inflammation, progressive fibrosis and diminished proteinaceous fluid of the gland[23,24]. In these cases, depiction of the tumor is poor on noncontrast T1-weighted fat-suppressed images; nevertheless, arterial phase images are very helpful in the discrimination of the size and extent of pancreatic ductal adenocarcinomas, as tumors almost always enhance less than the adjacent chronically inflamed pancreas[23,24]. These imaging characteristics along with substantial increase of CA 19.9 levels are unique to ductal adenocarcinoma and allow correct diagnosis with high accuracy.

Although it is non-specific, obstruction of the main pancreatic duct is one of the most important signs of ductal adenocarcinoma. The concurrent dilatation of the pancreatic and hepatic duct may frequently occurs when the pancreatic cancer develops in the cephalic region, thus depicting the so called "double duct sign", in some cases this may be the only sign, if the pancreatic tumor is very small. Possible differential diagnosis in this case includes an acute or chronic papillitis[2,11] and the ampullary carcinoma[25].

Regarding tumor resectability, radiologists should

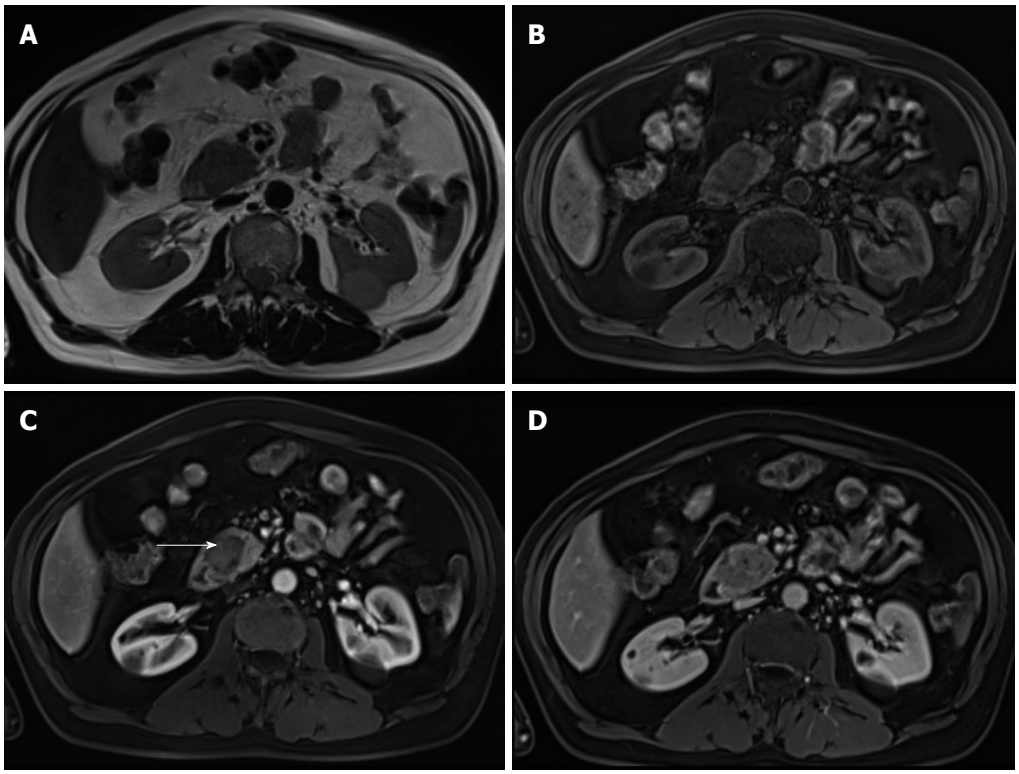


**Figure 3 Pancreatic ductal adenocarcinoma.** Axial T2-weighted single-shot echo train spin echo (A), pre-contrast fat-suppressed T1-weighted (B) gradient echo (GRE) and post-gadolinium fat-suppressed T1-weighted GRE images acquired in the arterial (C) and venous (D) phases of enhancement. There is a solid nodule in the head of the pancreas, which is more conspicuous in the pre-contrast and arterial phase T1-weighted images (B, arrow, C), consistent with ductal adenocarcinoma. Note that this lesion might be imperceptible on T2-weighted images (A) and venous phase images (D).

evaluate certain MRI findings and describe them in the MRI report: (1) distant metastases, frequently to the liver, peritoneum, lung and paraortic lymph nodes; (2) infiltration of neighboring structures, including stomach, colon, spleen; (3) invasion of the peripancreatic arteries, including celiac trunk, hepatic artery, superior mesenteric artery; and (4) invasion of the peripancreatic veins, including portal and superior mesenteric vein[2,14,22,26].

State of the art MRI is suitable to detect and characterize focal ductal adenocarcinoma smaller than 1 cm[2,21,22,27], which tend to appear as small non-contour-deforming pancreatic lesions. Detection of this early manifestation of disease is difficult or impossible to identify with multiphasic current-generation CT[28,29].

Endoscopy ultrasound has been widely used in detection of clinically suspected pancreatic lesion; together with fine needle aspiration, it has been reported to be the best diagnostic method for small pancreatic neoplasms. Unfortunately this is an invasive and an operator-dependent-technique and is not yet widely used[30].

It is very important to differentiate adenocarcinoma from other benign and malignant entities, because the clinical management and prognosis varies according to the type of pathology[2,31]. Some lesions require surgery or imaging follow-up, whereas other lesions are clinically irrelevant, not requiring further evaluation and/or treatment.

## BENIGN LESIONS THAT MAY SIMULATE DUCTAL ADENOCARCINOMA

### *Pancreatic lipomatosis*

Pancreatic lipomatosis is a condition related to fatty infiltration/replacement of the pancreatic parenchyma, and is commonly seen in the elder, especially in obese patients. Involvement is normally diffuse but occasionally it may simulate a neoplastic lesion. The anterior aspect of the head of the pancreas is the most common location for pancreatic lipomatosis (Figure 4).

The absences of mass effect, ductal or vascular displacement are important findings to establish the correct diagnosis.

MRI is highly specific for the detection of fat[32]. A moderate to marked signal loss in the out-of-phase relative to the in-phase images is distinctive of this condition (Figure 4)[33]. Macroscopic fatty replacement of the pancreas will show high T1 and T2 signal intensity, and marked signal loss on fat-suppressed sequences[32-34].

### *Acute pancreatitis*

Acute pancreatitis is defined as an acute inflammatory condition typically presenting with abdominal pain and elevation in pancreatic enzymes secondary mainly to alcoholism or cholelithiasis.

MRI is more sensitive than CT, supporting the use of MRI in the evaluation of patients with a nonconclusive

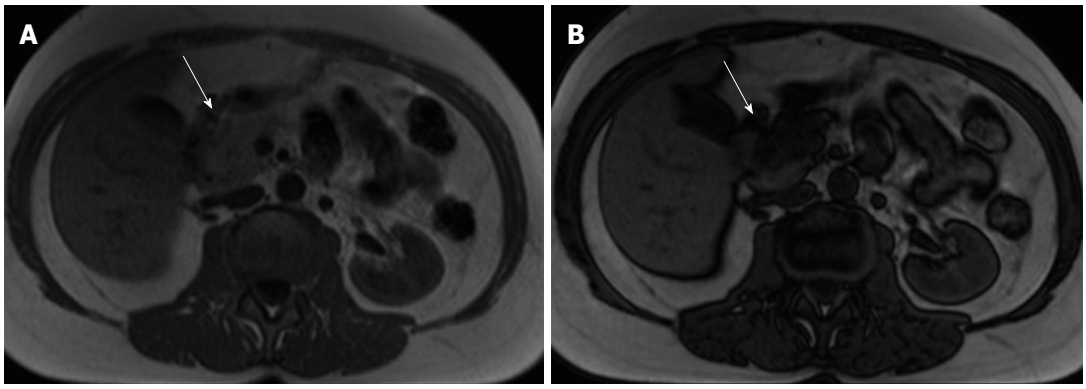


**Figure 4 Pancreatic lipomatosis.** Axial in-phase (A) and out-of-phase (B) T1-weighted GRE images. There is a focal fat infiltration in the region of the pancreatic head (arrows), only noticeable in the out-of-phase images, which is diagnostic for this entity. Focal fat infiltration is a benign condition that can simulate pancreatic adenocarcinoma especially on CT. GRE: Gradient echo; CT: Computed tomography.

CT or to differentiate pure inflammatory condition from neoplastic lesion of the pancreas.

The acutely inflamed pancreas shows either focal or diffuse enlargement of the parenchyma, with signal intensity comparable to that of normal pancreatic tissue in non-complicated mild to moderate pancreatitis. Peripancreatic fluid is an important sign visualized in acute pancreatitis, best displayed on fat-suppressed T2-weighted sequences, seen as high signal in a background of intermediate to low-signal pancreas and fat (Figure 5)[2,35,36].

### *Chronic pancreatitis*

Chronic pancreatitis is defined as a continuous or relapsing, chronic, inflammatory process of the pancreas, characterized by permanent morphologic changes and typically leads to diminishing of function. Distinction between focal pancreatitis and adenocarcinoma may be challenging because both entities may result in focal enlargement of the pancreatic head, atrophy of the tail of the pancreas and obliteration of the fat plane around the superior mesenteric artery. Ductal adenocarcinoma arising in the pancreatic head may cause obstruction of the CBD and pancreatic duct, with the MRCP appearance of a "double duct sign". This sign can be also appreciated, although less commonly, in patients with focal pancreatitis.

Focal chronic pancreatitis and adenocarcinoma may display comparable signal intensity changes of the enlarged region of pancreas on noncontrast T1- and T2-weighted images, including mild hypointensity on T1-weighted images and heterogeneous and mild hyperintensity on T2-weighted images.

On arterial phase images, focal chronic pancreatitis usually displays heterogeneous enhancement and may show signal voids from cysts and/or calcifications with no evidence of a definable mass. In this setting, the focally enlarged region of the pancreas preserve the glandular feathery texture, comparable to the remaining pancreas[37]. Conversely, in ductal adenocarcinoma, the focally enlarged region of the pancreas loses its usual anatomic detail.

Diffuse low T1 signal intensity and hypovascularity of the entire pancreas, including the region of focal enlargement, are distinctive for chronic pancreatitis. In the setting of ductal adenocarcinoma, the tumor enhances less than the adjacent chronically inflamed pancreatic parenchyma[38].

Several features favor a diagnosis of focal pancreatitis, including: (1) non-dilated or smoothly tapering pancreatic and bile ducts coursing through the mass ("duct penetrating sign")[38]; (2) parenchymal calcifications (seen as signal voids); (3) pancreatic duct beading and varying caliber; and (4) side branch dilatation. Instead, abrupt interruption of a smoothly dilated main pancreatic duct, minimal side-branch dilatation, upstream pancreatic atrophy and a high ratio of duct caliber to the pancreatic gland width are features typically observed in adenocarcinoma (Figure 2)[39].

A previous investigation evaluated the accuracy of MRI in the differentiation between ductal adenocarcinoma and chronic pancreatitis, in patients with focal pancreatic mass[37]; in this study, MR technique with the use of fat-suppressed T1-weighted 3D-GRE sequence was able to differentiate ductal adenocarcinoma from chronic pancreatitis with a sensitivity and specificity of 93% and 75%, respectively. The most critical finding for ductal adenocarcinoma of the pancreas was a relative delineation of the mass compared to the background pancreatic parenchyma. On the other hand, the most critical finding of chronic pancreatitis was an imprecise delineation with a mildly increased signal intensity and enhancement compared with the background pancreatic parenchyma on portal-venous phase images. These features reflect a more progressive enhancement of inflammatory tissue compared to ductal adenocarcinoma from arterial phase to portal-venous images. A further useful imaging feature is effacement of the fine, lobular architectural pattern of the pancreas in pancreatic adenocarcinoma[37].

The encasement of the celiac axis, superior mesenteric artery, lymphadenopathy and liver metastases

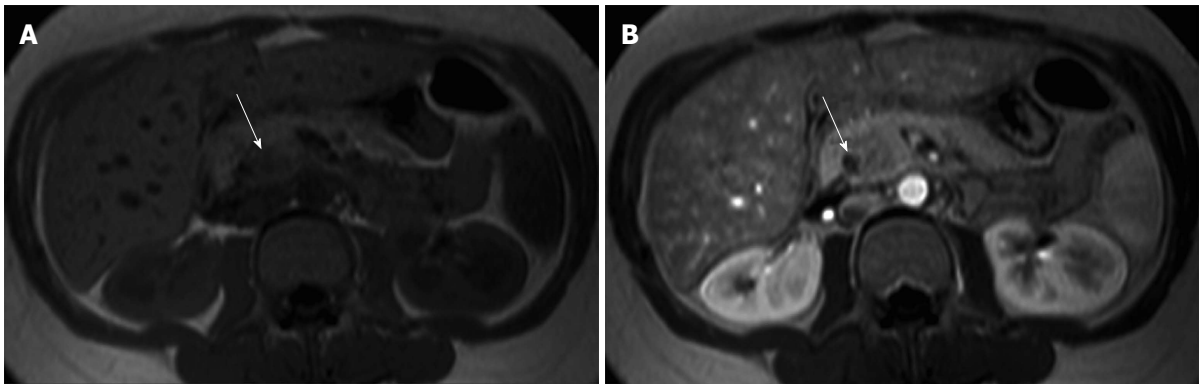


**Figure 5 Acute pancreatitis.** Axial in-phase (A) T1-weighted GRE image and arterial phase (B) fat-suppressed T1-weighted GRE image (B) in a patient with elevated amylase. There is a nodular area in the uncinate process showing mild T1-weighted hypointensity due to edema, however showing arterial enhancement (arrow, B) and with preservation of marbled pancreatic texture. This was compatible with focal acute pancreatitis. GRE: Gradient echo.

establish the diagnosis of ductal adenocarcinoma[26,40], with liver metastases representing the definitive distinction.

## OTHER SOLID PANCREATIC TUMORS WITH EPITHELIAL AND ENDOCRINE ORIGIN THAT MIGHT SIMULATE DUCTAL ADENOCARCINOMA

### *ACC*

ACC is a rare primary tumor of the exocrine gland of the pancreas, and although acinar cells comprise most of the pancreatic parenchyma, ACC represents only 1% of all exocrine pancreatic cancers. Tumors generally occur between the fifth and seventh decades[2]. It is defined as a carcinoma exhibiting pancreatic enzyme secretion by neoplastic exocrine cells, and its clinical presentation is usually related to either the local effects of the tumor or to metastases[41]. Presenting symptoms are frequently nonspecific. "Lipase hypersecretion syndrome" is related to hypersecretion of lipase by the ACC, which may result in subcutaneous fat necrosis, bone infarcts, and polyarthritis[42,43]. Hypoglycemia as a presenting symptom has also been observed in some patients.

These cancers are generally exophytic, oval or round, well marginated, and hypovascular. Small tumors are usually solid, whereas larger tumors almost invariably contain cystic areas representing regions of necrosis, hemorrhage, and occasionally amorphous intratumoral calcifications, seen as signal voids[38,39].

These tumors are frequently uniformly or partially well-defined, with thin, enhancing capsules, and enhance less than the adjacent normal background pancreas[38,39]. These tumors are predominantly low in signal intensity on T1-weighted images and iso- to moderately hyperintense on T2-weighted images.

ACC should always be considered when a large pancreatic mass with typical imaging is found a solid mass with variably sized central cystic areas or cystic masses[2,43-45]. The tumor marker CA 19.9, which is generally increased in pancreatic adenocarcinoma, is rarely elevated in ACC.

## UNCERTAIN ORIGIN

### *SPT*

SPT of the pancreas is an uncommon, low-grade epithelial malignancy of the exocrine pancreas that most often appears in young female patients[2,20,46], and accounts for about 1% to 2% of all pancreatic tumors[47].

This tumor is typically benign and is found mainly in young women between the 2nd and 3rd decades of life. This age presentation is rarely seen in ductal adenocarcinoma. This tumor shows a predilection for African-American and Asian women, despite rare cases having been reported in children and men. Malignant degeneration may occur, however most SPTs show benign behavior[48,49]. Complete surgical removal is the treatment of choice. Metastasis is rare but local recurrence has been described. The prognosis is excellent after resection.

The mass occurs most frequently in the head or tail. SPT is often discovered incidentally and appears as a large well-demarcated and encapsulated pancreatic mass, surrounded by a marginal thick capsule and with variable relative amounts of intralesional solid, cystic and hemorrhagic components. The peripheral capsule is often present and seen on MRI, with an incidence of 95%-100%[48]. Vascular encasement is exclusively seen in malignant types.

MR imaging characteristically shows a well-defined lesion with heterogeneous T1- and T2-weighted signal intensity, reflecting the complex nature of the mass. Regions of high T1 and low or inhomogeneous T2 signal intensity may be seen and are related with blood products and may help to differentiate SPTs from endocrine tumors, whose cystic components generally are not hemorrhagic and therefore not typically possessing moderately increased T1 signal intensity. Furthermore, the peripheral areas of SPTs are not

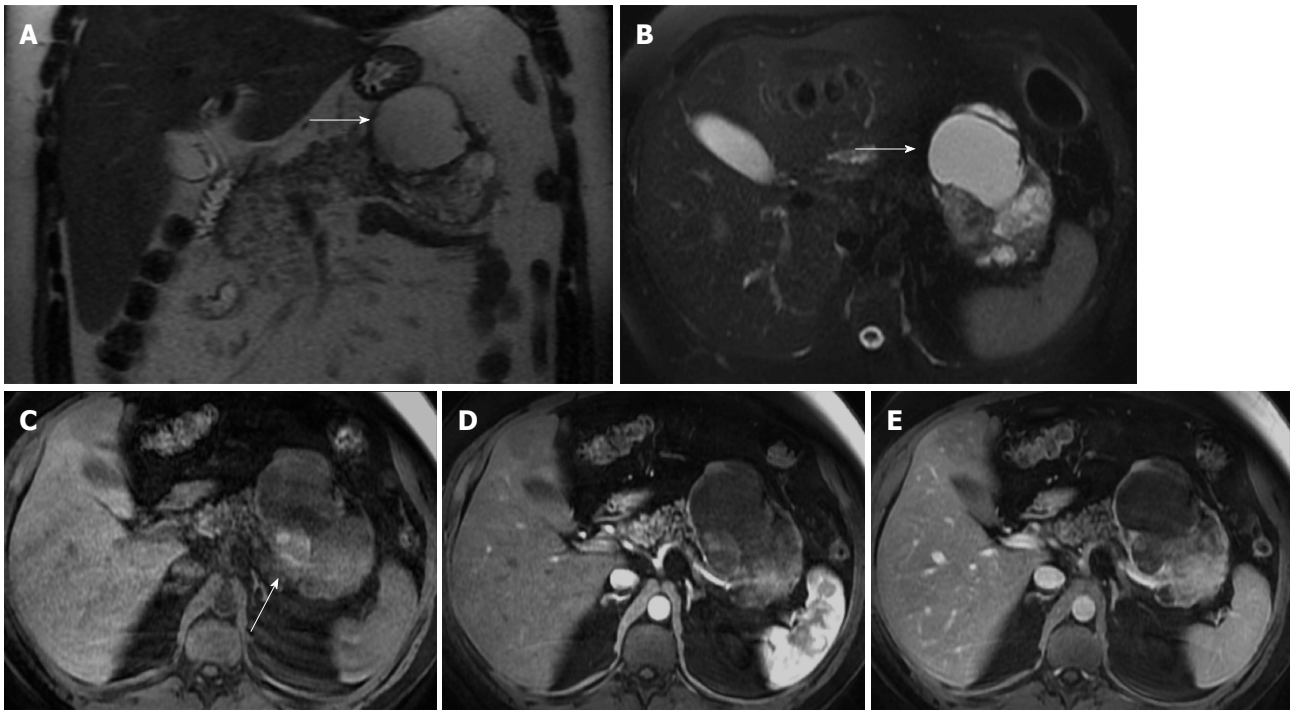


**Figure 6 Solid pseudopapillary tumor.** Coronal (A) and axial fat-suppressed (B) T2-weighted SS-ETSE, pre-contrast fat-suppressed T1-weighted (C) GRE and post-gadolinium fat-suppressed T1-weighted GRE images acquired in the arterial (D) and venous (E) phases of enhancement. A large well-demarcated and encapsulated mass is located in the tail and body of the pancreas. The mass shows heterogeneous signal intensity, with cystic (arrows, A and B) and hemorrhagic areas (arrow, C). The solid component of the lesion shows progressive enhancement over time. A mass with these characteristics, appearing in a young patient is most likely related with solid pseudopapillary tumor. SS-ETSE: Single-shot echo train spin echo; GRE: Gradient echo.

hypervascular, which is characteristically observed in islet cell tumors[2,46,48,49] (Figure 6).

## PANCREATIC NEUROENDOCRINE TUMORS

Pancreatic neuroendocrine tumors (NET) were previously called islet cell tumor, as it was believed that they derived from the islets of Langerhans. Recent evidence suggests that these tumors arise from pluripotential stem cells in the ductal epithelium[50]. They account for 1%-2% of all pancreatic neoplasms. The majority NETs are sporadic, but association with syndromes such as with Wermer syndrome, neurofibromatosis type 1, von Hippel-Lindau syndrome, and tuberous sclerosis have been reported. NETs are classified into functioning and non-functioning tumors. Functioning tumors may clinically present with an endocrine malfunction subsequent to hormone secretion[51]. The diagnosis of functioning NETs is almost always established biochemically, and the role of imaging is to depict the precise location of the tumor. Insulinomas and gastrinomas are the most common pancreatic NETs, followed by non-functional or untyped tumors.

Non-functional tumors account for 15%-20% of pancreatic NETs and tend to be symptomatic due to large tumor mass or metastatic disease. Functioning tumors manifest early in the course of disease when they are small, due to the clinical manifestations of excessive hormone secretion.

Malignancy cannot be determined based on the histological appearance of pancreatic NETs, instead it is established by the coexistence of metastases or local invasion. The liver is the most affected organ for metastatic spread.

Insulinomas are usually benign tumors, whereas gastrinomas are malignant in nearly 60% of cases. Nonfunctioning tumors are malignant in most cases.

Tumor morphology is variable. Small tumors are usually solid and homogeneous, whereas larger tumors are usually heterogeneous with cystic degeneration and calcifications.

On MRI, NETs are moderately low T1 and intermediate to high signal intensity on T2-weighted fat-suppressed images[52]. These tumors are typically highly hypervascular and therefore they enhance intensely on arterial/pancreatic phase after contrast administration. This distinctive feature must be interpreted cautiously, as although they may enhance more rapidly and avidly than the background pancreas, they may also appear iso-intense during the arterial phase, as the normal pancreatic parenchyma is also highly vascularized (Figure 7).

Insulinomas are usually seen as small tumors (< 2 cm), with intense and homogeneous enhancement on arterial phase images, whereas gastrinomas most commonly are larger lesions (3-4 cm approximately), with peripheral ring-like enhancement on arterial phase images[2,53]. Gastrinomas generally occur in a

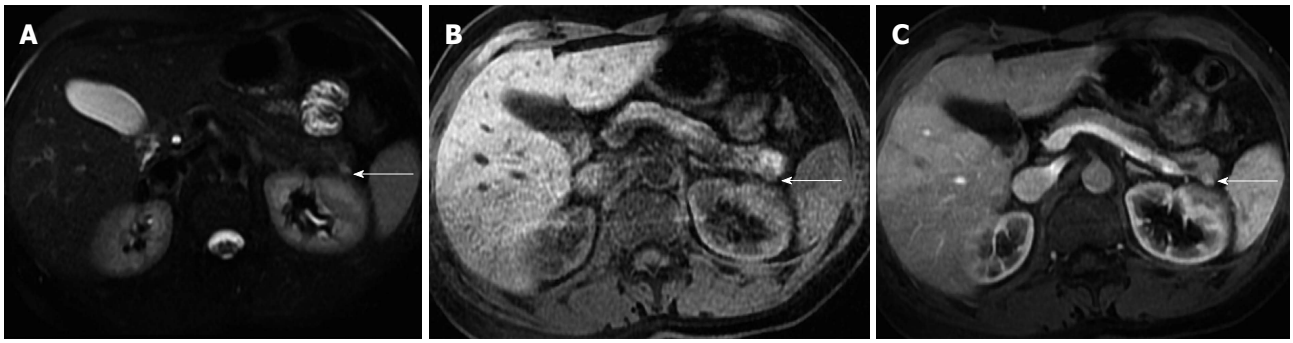


**Figure 7 Pancreatic neuroendocrine tumor.** Axial fat-suppressed T2-weighted SS-ETSE (A), pre-contrast fat-suppressed T1-weighted (B) GRE and arterial phase fat-suppressed T1-weighted GRE image (C). There is a small solid lesion in the tail of the pancreas (arrow, A-C), showing moderate signal intensity on T2-weighted images (arrow, A) and demonstrates marked enhancement in the arterial phase of enhancement (arrow, C). This was an insulinoma. SS-ETSE: Single-shot echo train spin echo; GRE: Gradient echo.

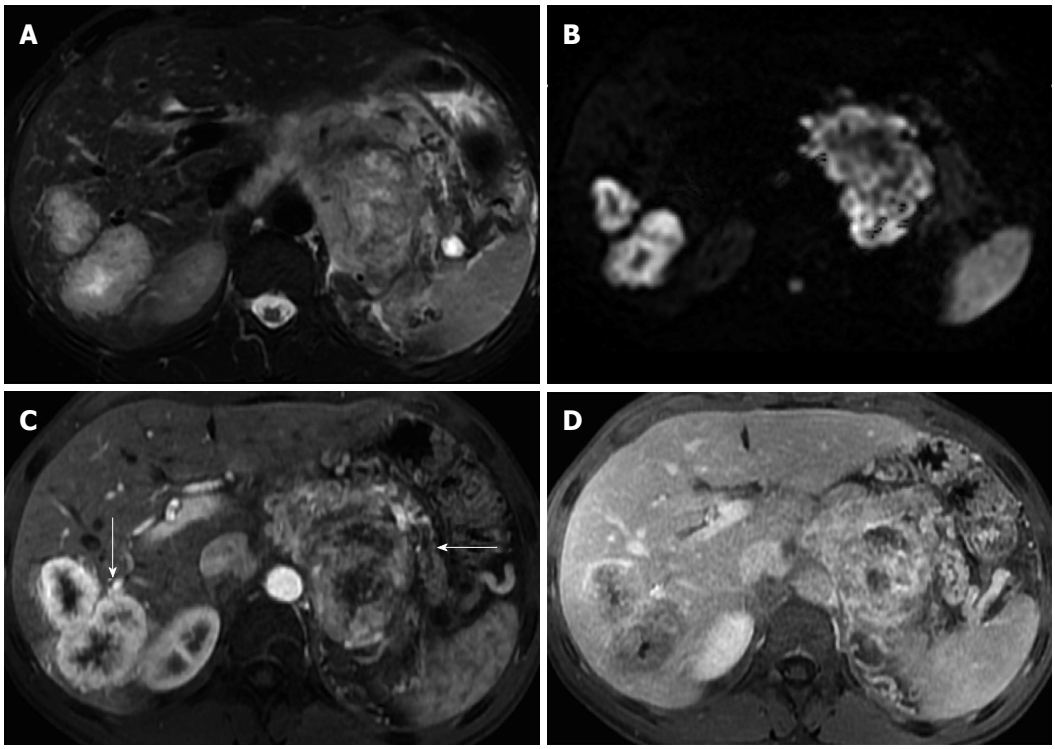


**Figure 8 Pancreatic neuroendocrine tumor and liver metastases.** Axial T2-weighted SS-ETSE (A), diffusion weighted images (b = 500) (B) and post-gadolinium fat-suppressed T1-weighted GRE images acquired in the arterial (C) and venous (D) phase of enhancement. A large mass is seen arising in the body and tail of the pancreas, showing moderate signal intensity on T2-weighted images (A) and restriction to diffusion (B). This lesion shows hypervascular characteristics (C). This mass was diagnosed as poorly differentiated neuroendocrine tumor. Note that the liver metastases show similar signal characteristics on T2- and diffusion-weighted images and demonstrate the characteristic arterial wash-in (arrow, C) and late washout (D) seen with neuroendocrine tumor metastases. SS-ETSE: Single-shot echo train spin echo; GRE: Gradient echo.

distinctive location, termed the gastrinoma triangle, bordered superiorly by the confluence of the cystic and CBDs; inferiorly, by the second and third portions of the duodenum; and medially, by the neck and body of the pancreas.

The likelihood of malignancy rises in parallel with tumor size, and tumors larger than 5 cm are frequently malignant. Even when malignant, these tumors are slow-growing and the prognosis is better than for ductal adenocarcinoma[18,54]. Metastases to lymph nodes and solid organs may have an enhancement pattern similar to that of the primary tumor (Figure 8).

It is essential to distinguish pancreatic NETs from other neoplasms, especially from ductal adenocarcinoma, as the prognosis and treatment options are usually substantially different for these two entities.

Features that discriminate most pancreatic NETs from pancreatic adenocarcinoma include the high T2 signal, increased homogeneous enhancement on arterial phase images, hypervascular liver metastases, and absence of pancreatic duct obstruction or vascular encasement[53]. On the other hand, venous thrombosis, peritoneal, and

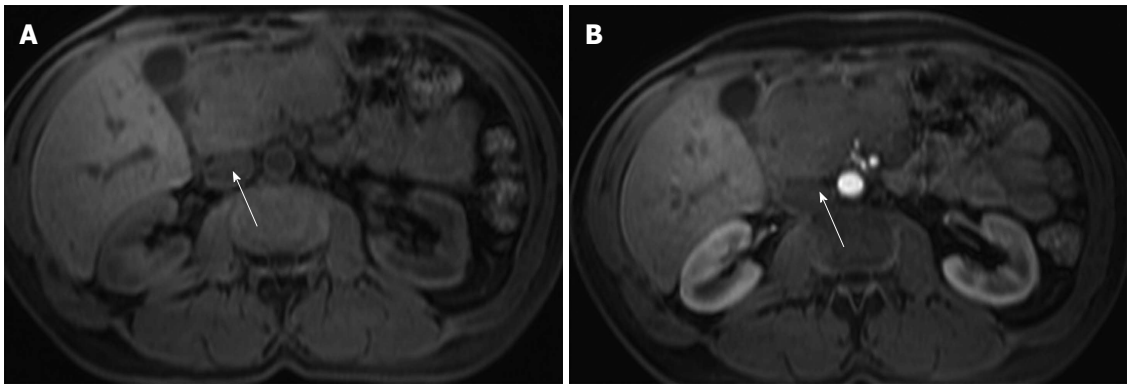


**Figure 9 Pancreatic lymphoma.** Pre-contrast fat-suppressed axial T1-weighted gradient - echo images (A) and acquired in the arterial phase after gadolinium injection (B). There is a large hypointence and hypovascular mass (arrows) localized in the pancreatic head, however showing no significant duct dilatation. There was evidence of enlarged lymph nodes. This mass was diagnosed as pancreatic lymphoma.

regional node enlargement are distinguishing features of pancreatic ductal adenocarcinoma, usually not seen in NETs.

## MESENCHYMAL TUMORS

Mesenchymal neoplasms of the pancreas are rare, accounting for 1% to 2% of all pancreatic tumors[55,56]. They derive from various connective tissue components and are classified according to their histologic origin.

Primary pancreatic lymphoma, although unusual, is the most common malignant mesenchymal tumor appearing in the pancreas. Benign mesenchymal adipose tissue tumors, such as lipomas or teratomas are extremely rare and show diagnostic features on MRI, with homogeneous encapsulated mature fat or with fat-fluid levels, respectively[55,56]. Other mesenchymal tumors, such as lymphangiomas, leiomyoma, leiomyosarcoma, schwannoma, hemangioma, or hemangioendothelioma, have also been reported; however, they are exceedingly rare, appearing described only in the form of isolated case reports.

### *Pancreatic lymphoma*

Non-Hodgkin lymphoma may involve peripancreatic lymph nodes or may directly infiltrate the pancreas. Peripancreatic lymph nodes show low to intermediate signal intensity on T1-weighted fat-suppressed images, which permit to be distinguished from the normal pancreas that shows high signal intensity[57].

Primary pancreatic lymphoma is a rare entity, accounting for less than 2% of extranodal lymphomas and 0.5% of pancreatic tumors[58].

Pancreatic lymphoma has a better prognosis than pancreatic ductal adenocarcinoma, as first-line treatment with chemotherapy is normally effective, allowing long-term disease regression or remission. Surgery is usually not required.

Two morphologic patterns are recognized: focal and diffuse form[59]. The focal form occurs in the pancreatic head in 80% of the cases and may mimic adenocarcinoma.

On MRI, lymphoma shows low T1 and intermediate T2 signal intensity. Several features may help discriminate pancreatic lymphoma from ductal adenocarcinoma such as the presence of a bulky confined tumor in the pancreatic head with absent or minimal main pancreatic duct dilatation, enlarged lymph nodes below the level of the renal vein, and a tendency to noninvasive tumor growth, which are characteristic for pancreatic lymphoma and atypical for pancreatic ductal adenocarcinoma (Figure 9). Vascular invasion is also less commonly seen in lymphoma[2]. Additionally, CA 19.9 levels are usually not elevated in primary or secondary pancreatic lymphoma.

## NONPANCREATIC TUMOR LESION

### *Metastases*

Metastases to the pancreas may be the result of direct invasion or hematogenous spread. Direct invasion from stomach and transverse colon carcinoma and GIST tumors are rare, but the most common forms of direct extension.

Metastases derive most frequently from renal cell carcinoma and lung cancer followed by breast, colon, prostate and malignant melanoma.

Three morphological patterns of metastatic involvement of the pancreas have been described: solitary lesion (50%-70% of cases), multifocal (5%-10%), and diffuse (15%-44%)[59].

Metastases generally show low T1 and mildly high T2 signal intensity. The enhancement of the majority of metastases follows a ring pattern, with a variable degree of enhancement depending on the angiogenic properties of the primary neoplasm (Figure 10)[60].

Renal cancer metastases resemble the appearance of NETs. Melanocytic melanoma metastases may display high T1 signal due to the paramagnetic properties of melanin pigment.

Ductal obstruction is uncommon, even with larger tumors, which is an important feature distinguishing

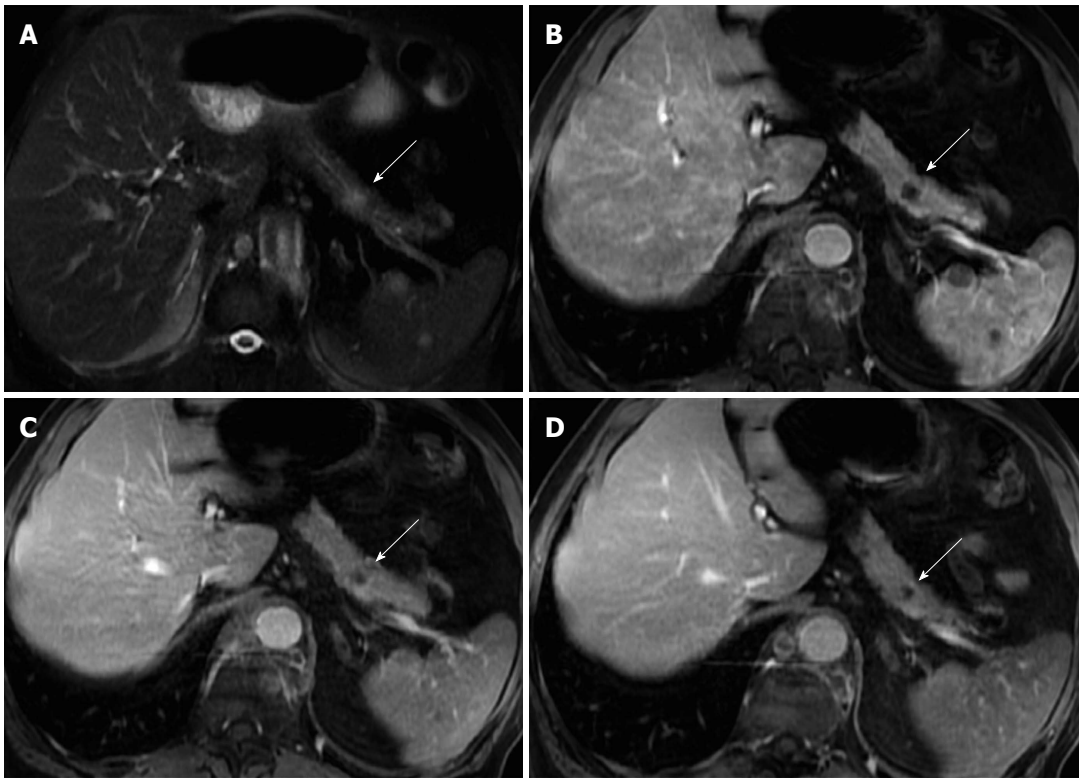


**Figure 10 Solitary pancreatic metastasis.** Axial T2-weighted SS-ETSE (A) and post-gadolinium fat-suppressed T1-weighted GRE images acquired in the arterial (B), venous (C) and interstitial (D) phases of enhancement. There is a nodular lesion in the pancreatic body showing moderate signal intensity on T2-weighted images (arrow, A) and showing hypovascular characteristics, with no pancreatic duct dilatation. These are typical features of a solitary pancreatic metastasis (arrows). Note additional splenic metastases (lung cancer). SS-ETSE: Single-shot echo train spin echo; GRE: Gradient echo.

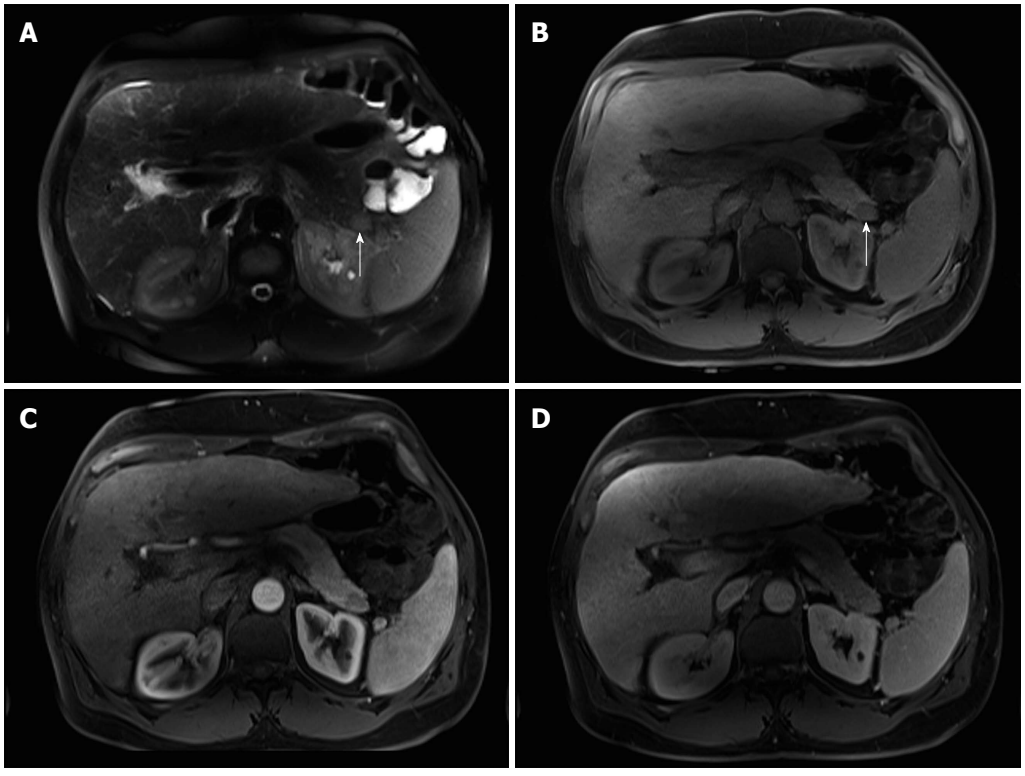


**Figure 11 Intra-pancreatic splenule.** Axial T2-weighted SS-ETSE (A), pre-contrast fat-suppressed T1-weighted (B) GRE and post-gadolinium fat-suppressed T1-weighted GRE images acquired in the arterial (C) and venous (D) phases of enhancement. There is a well-marginated and lobulated round intra-pancreatic splenule (arrows, A and B) that shows isointense signal to the pancreas on T2- and T1-weighted images (A and B). This nodule is hypointense compared to the background pancreas on the precontrast T1-weighted image (B) and demonstrates lesser enhancement relative to the pancreas on the arterial phase (C) and hepatic venous phase (D). The enhancement pattern was homogenous on the postgadolinium images and similar to that of the pancreas. SS-ETSE: Single-shot echo train spin echo; GRE: Gradient echo.

from pancreatic ductal adenocarcinoma[2,59].

## INTRAPANCREATIC SPLENULE

The presence of accessory splenules may arise within the parenchyma of solid organs, notably the pancreas. Intrapancreatic splenule is a somewhat uncommon location for splenules. These lesions typically are < 2 cm in size and are located within 3 cm of the tip of the pancreatic tail[55]. The presence of a well marginated rounded mass located in the distal tail of the pancreas with signal intensity features comparable to those of the spleen on all MR sequences suggests the diagnosis of intrapancreatic accessory spleen (Figure 11). A distinctive feature of these masses is that when greater than 2 cm they may exhibit serpiginous enhancement on arterial phase images, as typically seen in the spleen[61]. Other entities may simulate the signal intensity and post-gadolinium enhancement features of intrapancreatic splenules, and DWI and SPIO-enhanced MRI can be used to characterize the lesion and to establish the definite diagnosis[61,62].

## CONCLUSION

In addition to pancreatic ductal adenocarcinoma other solid pancreatic lesions occur. Many of the above-described tumors may be diagnosed with relatively high specificity employing MRI. The radiologist must be familiar with their MRI appearance to correctly diagnose them, or suggest them in the differential diagnosis when appropriate, since it may change substantially the approach, prognosis and patient management. We have described specific features that may aid in the discrimination from ductal adenocarcinoma and establish the correct diagnosis.

## REFERENCES


1 **Jemal A**, Siegel R, Ward E, Hao Y, Xu J, Murray T, Thun MJ. Cancer statistics, 2008. *CA Cancer J Clin* 2008; **58**: 71-96 [PMID: 18287387 DOI: 10.3322/CA.2007.0010]

2 **Altun E**, Elias Jr J, Armao D, Busakorn V, Semelka RC. Pancreas. 535-676. In: Abdominal-Pelvic MRI. 3rd edition. Semelka RC. editor. New Jersey: Wiley-Blackwell, 2010

3 **Semelka RC**, Ascher SM. MR imaging of the pancreas. *Radiology* 1993; **188**: 593-602 [PMID: 8351317 DOI: 10.1148/radiology.188.3.8351317]

4 **Zapparoli M**, Semelka RC, Altun E, Tsurusaki M, Pamuklar E, Dale BM, Gasparetto EL, Elias J. 3.0-T MRI evaluation of patients with chronic liver diseases: initial observations. *Magn Reson Imaging* 2008; **26**: 650-660 [PMID: 18440749 DOI: 10.1016/j.mri.2008.01.037]

5 **Mitchell DG**, Vinitski S, Saponaro S, Tasciyan T, Burk DL, Rifkin MD. Liver and pancreas: improved spin-echo T1 contrast by shorter echo time and fat suppression at 1.5 T. *Radiology* 1991; **178**: 67-71 [PMID: 1984328 DOI: 10.1148/radiology.178.1.1984328]

6 **Winston CB**, Mitchell DG, Outwater EK, Ehrlich SM. Pancreatic signal intensity on T1-weighted fat saturation MR images: clinical correlation. *J Magn Reson Imaging* 1995; **5**: 267-271 [PMID: 7633102 DOI: 10.1002/jmri.1880050307]

7 **Takehara Y**, Ichijo K, Tooyama N, Kodaira N, Yamamoto H, Tatami M, Saito M, Watahiki H, Takahashi M. Breath-hold MR cholangiopancreatography with a long-echo-train fast spin-echo sequence and a surface coil in chronic pancreatitis. *Radiology* 1994; **192**: 73-78 [PMID: 8208969 DOI: 10.1148/radiology.192.1.8208969]

8 **Bret PM**, Reinhold C, Taourel P, Guibaud L, Atri M, Barkun AN. Pancreas divisum: evaluation with MR cholangiopancreatography. *Radiology* 1996; **199**: 99-103 [PMID: 8633179 DOI: 10.1148/radiology.199.1.8633179]

9 **Soto JA**, Barish MA, Yucel EK, Clarke P, Siegenberg D, Chuttani R, Ferrucci JT. Pancreatic duct: MR cholangiopancreatography with a three-dimensional fast spin-echo technique. *Radiology* 1995; **196**: 459-464 [PMID: 7617861 DOI: 10.1148/radiology.196.2.7617861]

10 **Vachiranubhap B**, Kim YH, Balci NC, Semelka RC. Magnetic resonance imaging of adenocarcinoma of the pancreas. *Top Magn Reson Imaging* 2009; **20**: 3-9 [PMID: 19687720 DOI: 10.1097/RMR.0b013e3181b48392]

11 **Maccioni F**, Martinelli M, Al Ansari N, Kagarmanova A, De Marco V, Zippi M, Marini M. Magnetic resonance cholangiography: past, present and future: a review. *Eur Rev Med Pharmacol Sci* 2010; **14**: 721-725 [PMID: 20707292]

12 **Bian Y**, Wang L, Chen C, Lu JP, Fan JB, Chen SY, Zhao BH. Quantification of pancreatic exocrine function of chronic pancreatitis with secretin-enhanced MRCP. *World J Gastroenterol* 2013; **19**: 7177-7182 [PMID: 24222963 DOI: 10.3748/wjg.v19.i41.7177]

13 **Tirkes T**, Sandrasegaran K, Sanyal R, Sherman S, Schmidt CM, Cote GA, Akisik F. Secretin-enhanced MR cholangiopancreatography: spectrum of findings. *Radiographics* 2013; **33**: 1889-1906 [PMID: 24224585 DOI: 10.1148/rg.337125014]

14 **Perazella MA**. Current status of gadolinium toxicity in patients with kidney disease. *Clin J Am Soc Nephrol* 2009; **4**: 461-469 [PMID: 19201920 DOI: 10.2215/CJN.06011108]

15 **Jung JW**, Kang HR, Kim MH, Lee W, Min KU, Han MH, Cho SH. Immediate hypersensitivity reaction to gadolinium-based MR contrast media. *Radiology* 2012; **264**: 414-422 [PMID: 22550309 DOI: 10.1148/radiol.12112025]

16 **Azevedo RM**, de Campos RO, Ramalho M, Herédia V, Dale BM, Semelka RC. Free-breathing 3D T1-weighted gradient-echo sequence with radial data sampling in abdominal MRI: preliminary observations. *AJR Am J Roentgenol* 2011; **197**: 650-657 [PMID: 21862807 DOI: 10.2214/AJR.10.5881]

17 **Semelka RC**, Kroeker MA, Shoenut JP, Kroeker R, Yaffe CS, Micflikier AB. Pancreatic disease: prospective comparison of CT, ERCP, and 1.5-T MR imaging with dynamic gadolinium enhancement and fat suppression. *Radiology* 1991; **181**: 785-791 [PMID: 1947098 DOI: 10.1148/radiology.181.3.1947098]

18 **Mergo PJ**, Helmberger TK, Buetow PC, Helmberger RC, Ros PR. Pancreatic neoplasms: MR imaging and pathologic correlation. *Radiographics* 1997; **17**: 281-301 [PMID: 9084072 DOI: 10.1148/radiographics.17.2.9084072]

19 **Ros PR**, Mortelé KJ. Imaging features of pancreatic neoplasms. *JBR-BTR* 2001; **84**: 239-249 [PMID: 11817475]

20 **Low G**, Panu A, Millo N, Leen E. Multimodality imaging of neoplastic and nonneoplastic solid lesions of the pancreas. *Radiographics* 2011; **31**: 993-1015 [PMID: 21768235 DOI: 10.1148/rg.314105731]

21 **Lee ES**, Lee JM. Imaging diagnosis of pancreatic cancer: a state-of-the-art review. *World J Gastroenterol* 2014; **20**: 7864-7877 [PMID: 24976723 DOI: 10.3748/wjg.v20.i24.7864]

22 **Benassai G**, Mastrorilli M, Quarto G, Cappiello A, Giani U, Forestieri P, Mazzeo F. Factors influencing survival after resection for ductal adenocarcinoma of the head of the pancreas. *J Surg Oncol* 2000; **73**: 212-218 [PMID: 10797334 DOI: 10.1002/(SICI)1096-9098(200004)73:4<212::AID-JSO5>3.0.CO;2-D]

23 **Gabata T**, Matsui O, Kadoya M, Yoshikawa J, Miyayama S, Takashima T, Nagakawa T, Kayahara M, Nonomura A. Small pancreatic adenocarcinomas: efficacy of MR imaging with fat suppression and gadolinium enhancement. *Radiology* 1994; **193**: 683-688 [PMID: 7972808 DOI: 10.1148/radiology.193.3.7972808]

24 **Semelka RC**, Kelekis NL, Molina PL, Sharp TJ, Calvo B.

Pancreatic masses with inconclusive findings on spiral CT: is there a role for MRI? *J Magn Reson Imaging* 1996; **6**: 585-588 [PMID: 8835950 DOI: 10.1002/jmri.1880060405]
25 **Ahualli J**. The double duct sign. *Radiology* 2007; **244**: 314-315 [PMID: 17581912 DOI: 10.1148/radiol.2441041978]
26 **Clark LR**, Jaffe MH, Choyke PL, Grant EG, Zeman RK. Pancreatic imaging. *Radiol Clin North Am* 1985; **23**: 489-501 [PMID: 2997833]
27 **Morgan KA**, Adams DB. Solid tumors of the body and tail of the pancreas. *Surg Clin North Am* 2010; **90**: 287-307 [PMID: 20362787 DOI: 10.1016/j.suc.2009.12.009]
28 **Saisho H**, Yamaguchi T. Diagnostic imaging for pancreatic cancer: computed tomography, magnetic resonance imaging, and positron emission tomography. *Pancreas* 2004; **28**: 273-278 [PMID: 15084970 DOI: 10.1097/00006676-200404000-00011]
29 **Vellet AD**, Romano W, Bach DB, Passi RB, Taves DH, Munk PL. Adenocarcinoma of the pancreatic ducts: comparative evaluation with CT and MR imaging at 1.5 T. *Radiology* 1992; **183**: 87-95 [PMID: 1312736 DOI: 10.1148/radiology.183.1.1312736]
30 **Wang XY**, Yang F, Jin C, Fu DL. Utility of PET/CT in diagnosis, staging, assessment of resectability and metabolic response of pancreatic cancer. *World J Gastroenterol* 2014; **20**: 15580-15589 [PMID: 25400441 DOI: 10.3748/wjg.v20.i42.15580]
31 **Adsay NV**, Basturk O, Klimstra DS, Klöppel G. Pancreatic pseudotumors: non-neoplastic solid lesions of the pancreas that clinically mimic pancreas cancer. *Semin Diagn Pathol* 2004; **21**: 260-267 [PMID: 16273945 DOI: 10.1053/j.semdp.2005.07.003]
32 **Kim HJ**, Byun JH, Park SH, Shin YM, Kim PN, Ha HK, Lee MG. Focal fatty replacement of the pancreas: usefulness of chemical shift MRI. *AJR Am J Roentgenol* 2007; **188**: 429-432 [PMID: 17242252 DOI: 10.2214/AJR.05.1095]
33 **Isserow JA**, Siegelman ES, Mammone J. Focal fatty infiltration of the pancreas: MR characterization with chemical shift imaging. *AJR Am J Roentgenol* 1999; **173**: 1263-1265 [PMID: 10541101 DOI: 10.2214/ajr.173.5.10541101]
34 **Kawamoto S**, Siegelman SS, Bluemke DA, Hruban RH, Fishman EK. Focal fatty infiltration in the head of the pancreas: evaluation with multidetector computed tomography with multiplanar reformation imaging. *J Comput Assist Tomogr* 2009; **33**: 90-95 [PMID: 19188793 DOI: 10.1097/RCT.0b013e31815cff0d]
35 **Balthazar EJ**. CT diagnosis and staging of acute pancreatitis. *Radiol Clin North Am* 1989; **27**: 19-37 [PMID: 2642273]
36 **Ichikawa T**, Sou H, Araki T, Arbab AS, Yoshikawa T, Ishigame K, Haradome H, Hachiya J. Duct-penetrating sign at MRCP: usefulness for differentiating inflammatory pancreatic mass from pancreatic carcinomas. *Radiology* 2001; **221**: 107-116 [PMID: 11568327 DOI: 10.1148/radiol.2211001157]
37 **Kim JK**, Altun E, Elias J, Pamuklar E, Rivero H, Semelka RC. Focal pancreatic mass: distinction of pancreatic cancer from chronic pancreatitis using gadolinium-enhanced 3D-gradient-echo MRI. *J Magn Reson Imaging* 2007; **26**: 313-322 [PMID: 17610286 DOI: 10.1002/jmri.21010]
38 **Semelka RC**, Shoenut JP, Kroeker MA, Micflikier AB. Chronic pancreatitis: MR imaging features before and after administration of gadopentetate dimeglumine. *J Magn Reson Imaging* 1993; **3**: 79-82 [PMID: 8428105 DOI: 10.1002/jmri.1880030114]
39 **Siddiqi AJ**, Miller F. Chronic pancreatitis: ultrasound, computed tomography, and magnetic resonance imaging features. *Semin Ultrasound CT MR* 2007; **28**: 384-394 [PMID: 17970554 DOI: 10.1053/j.sult.2007.06.003]
40 **Wittenberg J**, Simeone JF, Ferrucci JT, Mueller PR, vanSonnenberg E, Neff CC. Non-focal enlargement in pancreatic carcinoma. *Radiology* 1982; **144**: 131-135 [PMID: 7089244 DOI: 10.1148/radiology.144.1.7089244]
41 **Chiou YY**, Chiang JH, Hwang JI, Yen CH, Tsay SH, Chang CY. Acinar cell carcinoma of the pancreas: clinical and computed tomography manifestations. *J Comput Assist Tomogr* 2004; **28**: 180-186 [PMID: 15091120 DOI: 10.1097/00004728-200403000-00005]
42 **Khalili M**, Wax BN, Reed WP, Schuss A, Drexler S, Weston SR, Katz DS. Radiology-pathology conference. Acinar cell carcinoma of the pancreas. *Clin Imaging* 2006; **30**: 343-346 [PMID: 16919557 DOI: 10.1016/j.clinimag.2006.05.027]
43 **Tatli S**, Mortele KJ, Levy AD, Glickman JN, Ros PR, Banks PA, Silverman SG. CT and MRI features of pure acinar cell carcinoma of the pancreas in adults. *AJR Am J Roentgenol* 2005; **184**: 511-519 [PMID: 15671372 DOI: 10.2214/ajr.184.2.01840511]
44 **Hsu MY**, Pan KT, Chu SY, Hung CF, Wu RC, Tseng JH. CT and MRI features of acinar cell carcinoma of the pancreas with pathological correlations. *Clin Radiol* 2010; **65**: 223-229 [PMID: 20152279 DOI: 10.1016/j.crad.2009.11.010]
45 **Hu S**, Hu S, Wang M, Wu Z, Miao F. Clinical and CT imaging features of pancreatic acinar cell carcinoma. *Radiol Med* 2013; **118**: 723-731 [PMID: 23358813 DOI: 10.1007/s11547-012-0908-5]
46 **Guerrache Y**, Soyer P, Dohan A, Faraoun SA, Laurent V, Tasu JP, Aubé C, Cazejust J, Boudiaf M, Hoeffel C. Solid-pseudopapillary tumor of the pancreas: MR imaging findings in 21 patients. *Clin Imaging* 2014; **38**: 475-482 [PMID: 24629792 DOI: 10.1016/j.clinimag.2014.01.015]
47 **Ng KH**, Tan PH, Thng CH, Ooi LL. Solid pseudopapillary tumour of the pancreas. *ANZ J Surg* 2003; **73**: 410-415 [PMID: 12801340 DOI: 10.1046/j.1445-2197.2003.t01-1-02634.x]
48 **Cooper JA**. Solid pseudopapillary tumor of the pancreas. *Radiographics* 2006; **26**: 1210 [PMID: 16848054 DOI: 10.1148/radiographics.26.4.0261210]
49 **Kalb B**, Sarmiento JM, Kooby DA, Adsay NV, Martin DR. MR imaging of cystic lesions of the pancreas. *Radiographics* 2009; **29**: 1749-1765 [PMID: 19959519 DOI: 10.1148/rg.296095506]
50 **Oberg K**, Eriksson B. Endocrine tumours of the pancreas. *Best Pract Res Clin Gastroenterol* 2005; **19**: 753-781 [PMID: 16253899 DOI: 10.1016/j.bpg.2005.06.002]
51 **Mozell E**, Stenzel P, Woltering EA, Rösch J, O'Dorisio TM. Functional endocrine tumors of the pancreas: clinical presentation, diagnosis, and treatment. *Curr Probl Surg* 1990; **27**: 301-386 [PMID: 1973365 DOI: 10.1016/0011-3840(90)90025-Z]
52 **Semelka RC**, Custodio CM, Cem Balci N, Woosley JT. Neuroendocrine tumors of the pancreas: spectrum of appearances on MRI. *J Magn Reson Imaging* 2000; **11**: 141-148 [PMID: 10713946 DOI: 10.1002/(SICI)1522-2586(200002)11:2<141::AID-JMRI10>3.0.CO;2-U]
53 **Semelka RC**, Cumming MJ, Shoenut JP, Magro CM, Yaffe CS, Kroeker MA, Greenberg HM. Islet cell tumors: comparison of dynamic contrast-enhanced CT and MR imaging with dynamic gadolinium enhancement and fat suppression. *Radiology* 1993; **186**: 799-802 [PMID: 8381551 DOI: 10.1148/radiology.186.3.8381551]
54 **Sheth S**, Hruban RK, Fishman EK. Helical CT of islet cell tumors of the pancreas: typical and atypical manifestations. *AJR Am J Roentgenol* 2002; **179**: 725-730 [PMID: 12185053 DOI: 10.2214/ajr.179.3.1790725]
55 **Ferrozzi F**, Zuccoli G, Bova D, Calculli L. Mesenchymal tumors of the pancreas: CT findings. *J Comput Assist Tomogr* 2000; **24**: 622-627 [PMID: 10966199 DOI: 10.1097/00004728-200007000-00021]
56 **Megibow AJ**, Francis IR. Unusual Pancreatic Neoplasms: Imaging. In: Imaging of the Pancreas Cystic and Rare Tumors. Carlo Procacci C, Megibow AJ, editors. Springer Berlin Heidelberg, 2003: 249-265
57 **Zeman RK**, Schiebler M, Clark LR, Jaffe MH, Paushter DM, Grant EG, Choyke PL. The clinical and imaging spectrum of pancreaticoduodenal lymph node enlargement. *AJR Am J Roentgenol* 1985; **144**: 1223-1227 [PMID: 3890486 DOI: 10.2214/ajr.144.6.1223]
58 **Zucca E**, Roggero E, Bertoni F, Cavalli F. Primary extranodal non-Hodgkin's lymphomas. Part 1: Gastrointestinal, cutaneous and genitourinary lymphomas. *Ann Oncol* 1997; **8**: 727-737 [PMID: 9332679 DOI: 10.1023/A:1008282818705]
59 **Tsitouridis I**, Diamantopoulou A, Michaelides M, Arvanity M, Papaioannou S. Pancreatic metastases: CT and MRI findings. *Diagn Interv Radiol* 2010; **16**: 45-51 [PMID: 20027546 DOI: 10.4261/1305-3825.DIR.1996-08.1]
60 **Al Ansari N**, Kim BS, Srirattanapong S, Semelka CT, Ramalho

M, Altun E, Woosley JT, Calvo B, Semelka RC. Mass-forming cholangiocarcinoma and adenocarcinoma of unknown primary: can they be distinguished on liver MRI? *Abdom Imaging* 2014; **39**: 1228-1240 [PMID: 24929668 DOI: 10.1007/s00261-014-0172-3]

61 **Herédia V**, Altun E, Bilaj F, Ramalho M, Hyslop BW, Semelka RC. Gadolinium- and superparamagnetic-iron-oxide-enhanced MR findings of intrapancreatic accessory spleen in five patients. *Magn Reson Imaging* 2008; **26**: 1273-1278 [PMID: 18440173 DOI: 10.1016/j.mri.2008.02.008]

62 **Jang KM**, Kim SH, Lee SJ, Park MJ, Lee MH, Choi D. Differentiation of an intrapancreatic accessory spleen from a small (< 3-cm) solid pancreatic tumor: value of diffusion-weighted MR imaging. *Radiology* 2013; **266**: 159-167 [PMID: 23093681 DOI: 10.1148/radiol.12112765]

**P- Reviewer**: Aktas S
**S- Editor**: Ji FF **L- Editor**: A **E- Editor**: Jiao XK

World Journal of Radiology

Submit a Manuscript: http://www.wjgnet.com/esps/
Help Desk: http://www.wjgnet.com/esps/helpdesk.aspx
DOI: 10.4329/wjr.v7.i11.375

*World J Radiol* 2015 November 28; 7(11): 375-381
ISSN 1949-8470 (online)


MINIREVIEWS

# Iliac vein compression syndrome: Clinical, imaging and pathologic findings

Katelyn N Brinegar, Rahul A Sheth, Ali Khademhosseini, Jemianne Bautista, Rahmi Oklu

Katelyn N Brinegar, Rahul A Sheth, Jemianne Bautista, Division of Interventional Radiology, Massachusetts General Hospital, Harvard Medical School, Boston, MA 02114, United States

Ali Khademhosseini, Harvard-MIT Division of Health Sciences and Technology, Cambridge, MA 02139, United States

Ali Khademhosseini, Wyss Institute for Biologically Inspired Engineering, Harvard University, Boston, MA 02115, United States

Ali Khademhosseini, Rahmi Oklu, Biomaterials Innovation Research Center, Department of Medicine, Brigham and Women's Hospital, Harvard Medical School, Boston, MA 02139, United States

Rahmi Oklu, Division of Interventional Radiology, Mayo Clinic, Scottsdale, AZ 85054, United States

Author contributions: Brinegar KN, Sheth RA, Khademhosseini A, Bautista J and Oklu R conceived the issues which formed the content of the manuscript and equally aided in its writing, editing, and revising.

Conflict-of-interest statement: The authors declared no conflicts of interest and have no financial disclosures.



Correspondence to: Rahmi Oklu, MD, PhD, Division of Interventional Radiology, Mayo Clinic, 5777 E Mayo Blvd, Scottsdale, AZ 85054, United States. oklu.rahmi@mayo.edu
Telephone: +1-480-3421650
Fax: +1-480-3421650

Received: May 6, 2015
Peer-review started: May 8, 2015
First decision: July 10, 2015
Revised: August 3, 2015
Accepted: September 10, 2015
Article in press: September 16, 2015
Published online: November 28, 2015

## Abstract

May-Thurner syndrome (MTS) is the pathologic compression of the left common iliac vein by the right common iliac artery, resulting in left lower extremity pain, swelling, and deep venous thrombosis. Though this syndrome was first described in 1851, there are currently no standardized criteria to establish the diagnosis of MTS. Since MTS is treated by a wide array of specialties, including interventional radiology, vascular surgery, cardiology, and vascular medicine, the need for an established diagnostic criterion is imperative in order to reduce misdiagnosis and inappropriate treatment. Although MTS has historically been diagnosed by the presence of pathologic features, the use of dynamic imaging techniques has led to a more radiologic based diagnosis. Thus, imaging plays an integral part in screening patients for MTS, and the utility of a wide array of imaging modalities has been evaluated. Here, we summarize the historical aspects of the clinical features of this syndrome. We then provide a comprehensive assessment of the literature on the efficacy of imaging tools available to diagnose MTS. Lastly, we provide clinical pearls and recommendations to aid physicians in diagnosing the syndrome through the use of provocative measures.

**Key words:** May-Thurner; Thrombosis; Diagnostic; Iliac compression; Vascular; Imaging



**Core tip:** There is currently no gold standard diagnostic criterion in iliac vein compression syndrome. Historically, the presence of pathologic factors has been the main component in diagnosis; however, imaging techniques

have led to a more radiologic-based diagnosis. This review details the clinical and radiologic challenges in the diagnosis of Iliac vein compression syndrome and presents clinical pearls that may help in deciding whether an endovascular intervention should be performed.

Brinegar KN, Sheth RA, Khademhosseini A, Bautista J, Oklu R. Iliac vein compression syndrome: Clinical, imaging and pathologic findings. *World J Radiol* 2015; 7(11): 375-381 Available from: URL: http://www.wjgnet.com/1949-8470/full/v7/i11/375.htm DOI: http://dx.doi.org/10.4329/wjr.v7.i11.375

## INTRODUCTION

Iliac vein compression syndrome, also know as May-Thurner syndrome (MTS), is caused by both mechanical and physiologic factors; the chronic pulsatile compression of the left common iliac vein (LCIV) by the right common iliac artery (RCIA) stimulates the formation of fibrotic adhesions that can cause partial or complete iliac vein obstruction over time[1,2]. The true incidence of MTS is not known. However, iliofemoral thrombosis is responsible for approximately 2%-3% of lower limb deep venous thrombosis (DVT) cases and approximately 50%-60% of left sided iliofemoral DVT cases exhibit iliac vein spurs resulting from extrinsic compression[3-6]. Thus, MTS is a reasonably common occurrence and a greater level of clinical suspicion is necessary.

Although MTS has historically been diagnosed by the presence of pathologic features, the use of dynamic imaging techniques has led to a more radiologic based diagnosis. However, a diagnosis of MTS relies on both clinical and imaging findings because the presence of iliac vein compression alone is insufficient for a diagnosis. There are currently no standardized clinical or radiologic diagnostic protocols in place to aid in the identification of MTS. Since MTS is treated by a wide array of specialties, including interventional radiology, vascular surgery, cardiology, and vascular medicine, the need for an established diagnostic criterion is imperative in order to reduce misdiagnosis and inappropriate treatment. MTS patients generally do not respond well to conservative treatments; thus, early diagnosis and treatment is paramount in order to avoid complications such as iliofemoral DVT or venous insufficiency[3,4]. This review will describe the clinical presentations of MTS and focus on the imaging modalities that have been used in aiding and confirming a diagnosis.

## HISTORICAL BACKGROUND

In 1851, Virchow noted the first anatomical evidence for MTS when he observed an increased frequency of DVT in the left leg due to the compression of the left iliac vein between the overlying right iliac artery and the fifth lumbar vertebrae[4]. In 1908, McMurrich examined the iliac veins of 107 cadavers and observed that 29.9% had obstructions in the left iliac vein; he deemed that these obstructions were congenital in origin and were responsible for the increased incidence of left lower extremity (LLE) DVT[7]. In 1943, Ehrich and Krumbhaar found that out of 412 cadavers, 95 (23.8%) demonstrated obstructive lesions in the LCIV; the obstructions were comprised of collagen and elastin and were demonstrated to be acquired rather than congenital, as was previously thought[8]. However, a comprehensive understanding of the anatomic variants of MTS was not established until 1957, with the work of May and Thurner.

May and Thurner, for whom the syndrome is named, found that 22% of 430 cadavers exhibited lesions in the LCIV; these lesions were described as "spurs" and were postulated to arise from the chronic compression of the LCIV by the RCIA. The spurs were categorized as central, lateral, or resulting in partial obliteration, based on location and size. Central spurs occur on the anteroposterior plane and split the lumina in two, lateral spurs occur along the sides of the LCIV, and partial obliteration results in the lumen being covered in a lattice of spurs and results in decreased venous flow[7,8]. In 1965, Cockett *et al*[9] further expounded the field by determining that patients with LCIV spurs could remain asymptomatic for a period of time due to the formation of venous collaterals. However, it was ruled that spur formation was an irreversible process, making early diagnosis integral for MTS patients.

## ROLE OF CLINICAL PRESENTATION IN DIAGNOSIS

The clinical presentation and history of the patient are critical components in formulating a diagnosis of MTS. MTS is particularly prevalent in younger and middle aged women (mean age = 42), although it also affects men[5]. Patients most commonly present with DVT, but may also present with LLE swelling, pain, venous claudication, ulcerations, nausea, and varicose veins. Rarer symptoms include phlebitis, phlegmasia alba dolens, phlegmasia cerulea dolens, and bilateral or right sided symptoms[3,5-7,10]. MTS can present either acute or chronically; acute presentation of MTS is the sudden onset of left leg edema and is usually easier to diagnose, while the chronic phase of MTS is much more difficult to identify and requires a comprehensive investigation of patient history, physical examination, and diagnostic imaging studies[7]. The clinical stages of MTS can be further delineated as being either Stage Ⅰ, asymptomatic LCIV compression; stage Ⅱ, the formation of an intraluminal spur; or Stage Ⅲ, the occurrence of left iliac vein DVT[11].

A patient history that reveals recurrent DVT, unexplained LLE edema, venous claudication, or varicosities should create suspicion for MTS as a cause. Additionally, physical examination that demonstrates LLE swelling,

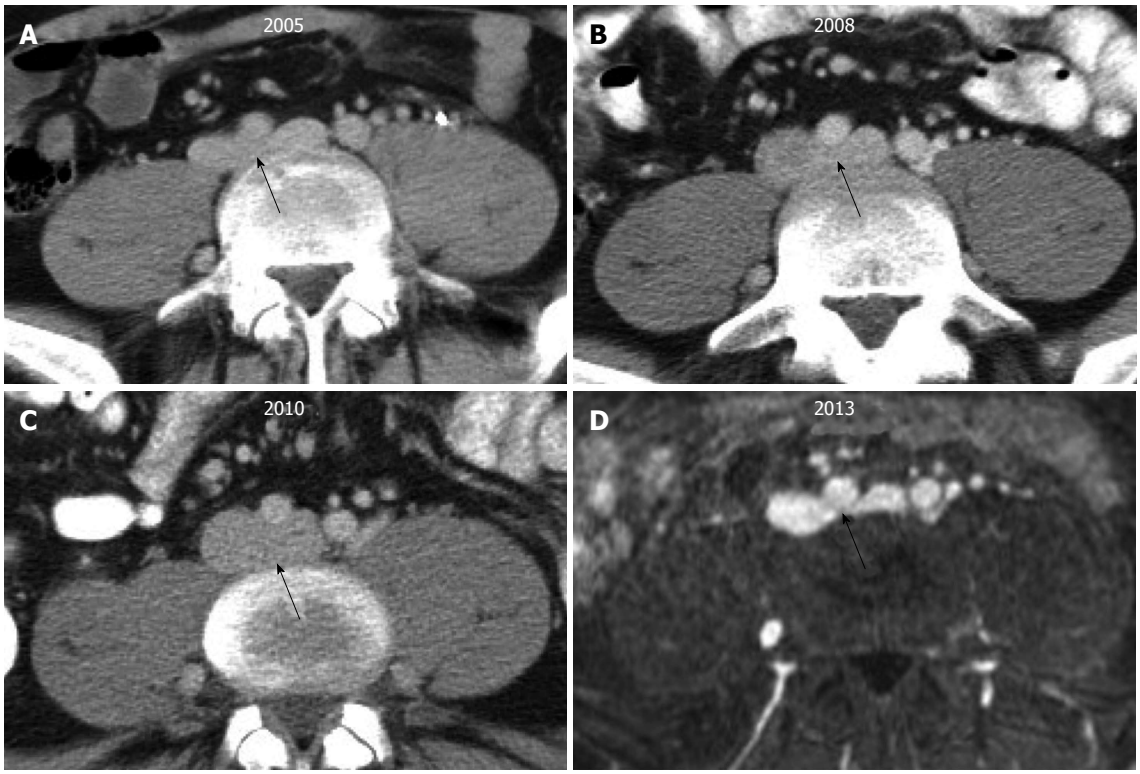


**Figure 1 Transverse computed tomography and magnetic resonance images of the proximal left common iliac vein (black arrow) in a single patient across multiple time points illustrate the challenge of diagnosing May-Thurner syndrome.** The degree of venous compression can vary substantially from one imaging study to another based upon the patient's volume status.

skin hyperpigmentation, varicose veins, telangiectasias, or evidence of ulceration in the ankle area are supportive of MTS[7,12]. Iliofemoral thrombosis can also be a result of trauma, surgery, immobilization, recent catheterization, radiation and malignancies and all these explanations must be ruled out in order to diagnose MTS[13]. Once differential diagnoses have been investigated, diagnostic imaging tests should be undertaken in order to confirm the presence of MTS anatomy and determine the best modality of treatment.

## DIAGNOSTIC IMAGING CRITERION AND TECHNIQUES

Several studies have confirmed the presence of LCIV compression in an asymptomatic patient population; these suggest that LCIV compression is a normal anatomic variant and not necessarily a pathologic condition[14-16]. Moreover, McDermott *et al*[1] found that the degree of LCIV compression in a single patient can vary over a short period of time (Figure 1); thus, the finding of May-Thurner anatomy in a single imaging study may just reflect the volume status of patient and may not be sufficient to suspect or confirm MTS[1]. Although there is no established diagnostic imaging criterion for MTS, studies recommend that the imaging standard for appropriate diagnosis of MTS should exhibit persistent narrowing of the iliac vein due to the presence of permanent iliac spurs, regardless of patient positioning during the imaging study. Thus, normal variant LCIV compression may be ruled out by placing the patient in prone position as such positioning may demonstrate a decrease in collateral flow or reveal normal iliac vein patency[1]. A visualization of greater than 50% stenosis in the luminal diameter of the vein is considered an adequate indicator of LCIV compression related to MTS[17]. An additional secondary indicator of MTS is the presence of venous collaterals, presence of intraluminal spurs, and changes in hemodynamic flow greater than 2 mmHg across the stenotic region with the patient in supine positioning[1,4,17]. The MTS diagnostic imaging modalities include ultrasonography, pleythysmography, computed tomography (CT), magnetic resonance venography (MRV), ascending contrast venography, hemodynamic studies, and intravascular ultrasound (IVUS) (Figure 2). The advantages and disadvantages of each imaging technique in the diagnosis of MTS are discussed below.

### *Ultrasonography*

Color Doppler ultrasonography (CDUS) is often the initial diagnostic modality in determining venous insufficiencies and DVT because it is noninvasive, bares no risk to the patient, is easy to perform, and is accurate in determining the location, severity, and cause of venous insufficiencies[18]. Ultrasound can usually identify acute iliofemoral DVT, a common result of MTS[7]. However, ultrasound has significant limitations in visualizing

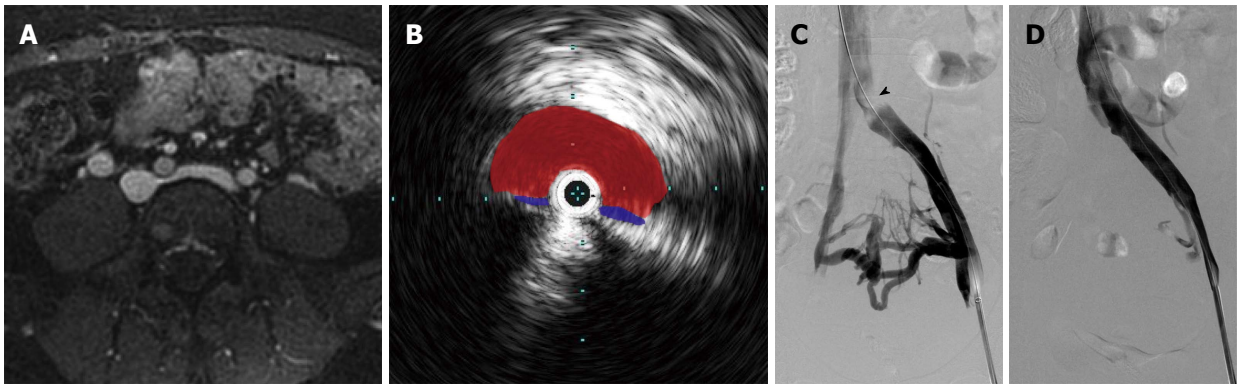


**Figure 2 The appearance of May-Thurner syndrome on multiple imaging modalities from a single patient.** A: Axial T1 fat-saturated magnetic resonance image following the administration of an intravascular contrast agent demonstrates > 50% narrowing of the left common iliac vein by the overlying right common iliac artery; B: Intravascular ultrasound with the transducer within the left common iliac vein (blue) demonstrates near complete obliteration of the vessel's lumen due to compression by the right common iliac artery (red); C: Digital subtraction angiography with contrast injection from a vascular sheath in the left external iliac vein demonstrates an obliquely oriented silhouette of the right common iliac artery compressing the left common iliac vein (arrowhead); multiple left-to-right pelvic collaterals are also present, signifying that the compression is hemodynamically significant; D: Following the placement of an uncovered stent, the compression is resolved, and there is no longer filling of the cross-pelvic collaterals.

abnormalities of the iliac veins because of the deep location of the veins in the pelvis; skilled sonographers are unable to visualize the iliac veins in approximately 20% of cases. Moreover, ultrasound does not reveal the specific anatomic characteristics of MTS such as iliac vein compression or intraluminal spurs[4,18]. However, in a case report by Oğuzkurt *et al*[3], a diagnosis of MTS was initially reached by transabdominal ultrasonography alone and later confirmed by CT, venography, and pressure measurements. Although transvaginal ultrasound can be used to determine the pathological reflux in the internal iliac veins in women, it does not allow for good imaging of the common iliac veins and is therefore not a very useful tool in the diagnosis of MTS[19]. Overall, ultrasound is a useful mechanism for determining venous patency, but a negative study result does not rule out the possibility of MTS and therefore more imaging tests are needed in order to establish a diagnosis.

### *Pleythysmography*

Air pleythysmography (APG) is a noninvasive test that can determine the degree of venous reflux and evaluate any proximal obstructions[7]. Hurst *et al*[5] utilized APG to determine the degree of iliac vein obstruction in 9 patients in order to confirm a suspected diagnosis of MTS. In all 9 cases, APG was unable to detect any iliac vein obstructions despite the presence of occlusions or stenosis in all patients. Hurst *et al*[5] thus concluded that APG has a low sensitivity in confirming a diagnosis of MTS. Although APG can be useful in evaluating the severity of venous symptoms, it can be nondiagnostic due to the presence of collateral pathways and a lack of sufficient narrowing to impact the flow dynamics[4,5]. Therefore, APG is not considered a routine diagnostic tool for MTS and more invasive tests are required in order to confirm a diagnosis of MTS.

### *CT*

CT with intravenous contrast in a transverse plane has proven to be a useful modality in confirming the diagnosis of MTS[14,18,20]. A CT examination of the abdomen or pelvis can rule out extrinsic reasons of compression as well as identify acute DVT and collateral pathways; however, a normal CT with 10-mm cuts cannot always establish a diagnosis of MTS because small iliac spurs are often too difficult to visualize and fibrosis can conceal the underlying vasculature[7,8,21]. However, a CT analysis utilizing narrower cuts 3 to 5-mm can be sufficient enough to visualize the structural details that may be previously missed. Chung *et al*[21] utilized spiral CT venography to evaluate iliac vein compression due to MTS in 27 out of 44 patients presenting with lower extremity DVT; Oguzkurt *et al*[22] found that CT images in a transverse plane showed the compression of the LCIV by the LCIA in all 10 patients tested. Additionally, in a study conducted by Liu *et al*[17], CT venography was found to have a high sensitivity and specificity in confirming MTS over other imaging modalities and that it can also distinguish between non-thrombotic and thrombotic MTS. The advantages of CT venography over CDUS or traditional venography include lack of operator dependence, clearer imaging of the pelvic veins, and a shorter exam time; however, the radiation dose is contraindicated in instances of pregnancy and large amount of contrast medium required for CT venography are contraindicated in patients with renal impairment[22]. Overall, CT venography is a useful diagnostic tool in demonstrating iliac vein compression, although more studies are required in order to fully evaluate the sensitivity and specificity of CT images in diagnosing MTS.

### *MRV*

Several studies have advocated that MRV is a suitable

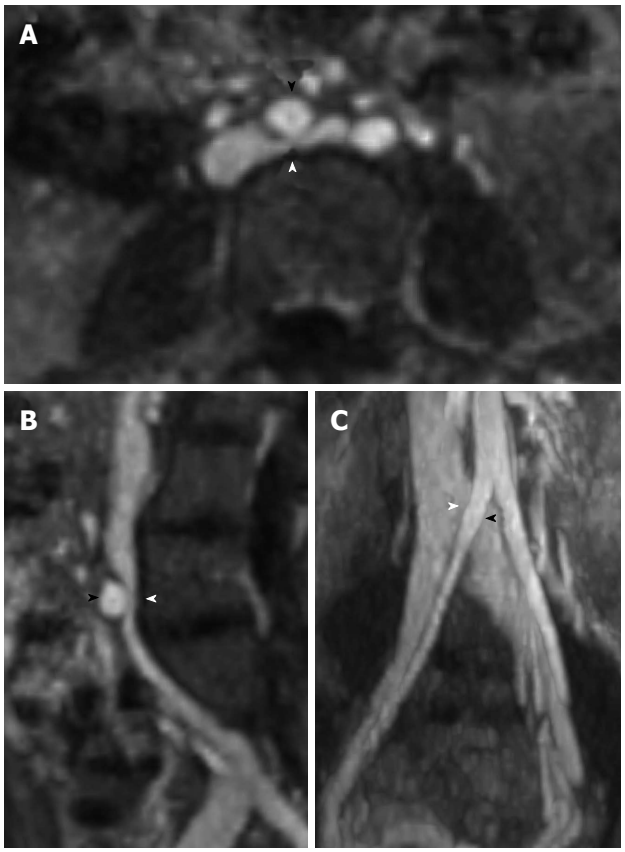


**Figure 3 Magnetic resonance venography with axial (A), sagittal (B), and coronal (C) reformatted images demonstrating May-Thurner syndrome anatomy with compression of the left common iliac vein (white arrowhead) by the right common iliac artery (black arrowhead).**

imaging modality in diagnosing MTS (Figure 3)[4-7,13]. In a case study by Wolpert *et al*[13], MRV was able to confirm a diagnosis of MTS in all 9 patients that presented with the condition; moreover, MRV was able to reveal the anatomic abnormalities of MTS as well as rule out the presence of DVT or pelvic masses. Additionally, Shebel *et al*[7] found that MRV was able to confirm the presence of nonocclusive iliac spurs (thus confirming a diagnosis of MTS) in 5 patients that had normal DUS results. The primary advantages of MRV in the diagnosis of MTS include its noninvasiveness, ability to analyze all pelvic structures, and lack of operator dependence[13]. Additionally, MRV can estimate the degree of venous collateral flow, which greatly assists in the diagnosis of MTS[23]. Lastly, MRV can be performed without contrast, which is beneficial to patients with contraindications such as contrast allergies or renal impairment[8]. Conversely, the primary disadvantage of MRV in the diagnosis of MTS is that the vasculature above bifurcations has nonlaminar flow, which sometimes presents a confusing image[13]. Additionally, MRV studies are expensive, take significant time to perform, and are hard to perform on severely ill patients[18].

Although MRV is a beneficial diagnostic option, a single MRV study may not be sufficient enough to diagnose MTS; McDermott *et al*[1] found that the degree of left iliac vein compression significantly differs in the same patient when undergoing repeated MRV imaging within a short period of time due to factors such as volume status or patient positioning[1,8]. Because MTS is a chronic condition with the development of permanent adhesions and intraluminal spurs, the degree of left iliac vein compression should not change significantly over time or depend on patient positioning. Thus, the sole finding of MTS anatomy on one MRV study may not be sufficient enough to confirm a diagnosis of MTS and more imaging studies may be necessary in order to reach a definitive diagnosis.

### *Contrast venography/hemodynamic studies*

Contrast venography has widely been considered the gold standard diagnostic modality for MTS and has been utilized to confirm a diagnosis of MTS in several studies[5,6,12,24]. The procedure demonstrates the degree of iliac vein stenosis and can visualize any pelvic venous collaterals. Contrast dye must be injected in either the popliteal or femoral veins, as the standard method of dye injected into the dorsum of the foot is not adequate to fully visualize the iliac venous system[7,8]. Venography also allows for hemodynamic evaluation of MTS through pressure gradient measurements; iliofemoral stenosis is considered significant with a measurement of greater than 2 mmHg at rest and greater than 3 mmHg during periods of exercise. However, a nondiagnostic result does not rule out MTS because the patient is tested while at rest; exercise is usually required to increase blood flow to demonstrate a significant pressure gradient[4,7]. Although ascending venography almost always provides the evidence needed for a confirmed diagnosis of MTS, it is time consuming, invasive, cannot be performed in patients with widespread iliofemoral DVT and can result in post-procedural complications such as phlebitis[18].

### *IVUS*

IVUS, using either a 12.5-MHz or 20-MHz ultrasound transducer, can accurately determine LCIV vessel size and morphology, and can verify the presence of MTS anatomy[10,25,26]. Knipp *et al*[6] utilized IVUS to confirm a diagnosis of MTS in 36 out of 58 patients; (62.1%) and defined the IVUS criteria for an MTS diagnosis as the lack of an evident venous lumen proximate to the IVUS catheter. In a small scale study conducted by Forauer *et al*[10], IVUS was not only used to confirm a diagnosis of MTS in all patients ($n$ = 16), but information provided by the study was also found to influence the endovascular management of approximately 50% of the cases while also assisting with stent placement choice and accuracy. Moreover, in some studies, IVUS was found to have a higher success than venography in identifying obstructions[27-29]. Overall, IVUS is a useful modality in the diagnosis of MTS, although more studies are needed to truly evaluate its advantages over other diagnostic techniques.

## CLINICAL PEARLS TO IMPROVE MTS DIAGNOSIS

There are several clinical pearls that can be considered in the diagnosis of MTS. For instance, if ultrasound is possible and allows for visualization of the iliac veins, provocative maneuvers (*i.e.*, placing the patient in supine *vs* lateral positions or imaging during valsalva) may be performed to help demonstrate permanent vascular changes. These provocative maneuvers may also be used at the time of venography. Supine and prone CT or magnetic resonance imaging and cone beam CT at the time of venography may reveal the true state of common iliac vein. Additionally, due to the nil per os status for the procedure, the patient may be hypovolemic causing the IVC and iliac veins to easily flatten; in these cases, an IV bolus of 500-1000 cc of normal saline may be provided to the patient.

## TREATMENT OPTIONS

Due to the mechanical nature of the obstruction, MTS patients generally do not respond well to conservative treatments[4]. In the past, surgical management of MTS has resulted in variable outcomes, as it is correlated with a high morbidity rate and has varied success in reestablishing venous patency[4,5]. Currently, the use of endovascular techniques in the treatment of MTS patients is considerably successful and carries less risk than invasive surgical treatments[8]. Common endovascular treatment options include catheter-directed thrombolysis, angioplasty, and ultimately stent placement[3,5,6,10,24]. Angioplasty has been found to be associated with low long-term patency rates, which indicates that the iliac vein compression may not be alleviated with solely the use of balloon angioplasty[30]. Additionally, stent placement is often necessary; however, stents are also associated with poor long-term patency rates, thus making diagnostic accuracy even more critical in the treatment of MTS patients as the choice to stent should be not be chosen lightly[8]. Overall, more studies are needed in order to fully evaluate the endovascular treatment that can provide the best outcome[8].

## CONCLUSION

Prompt diagnosis is critical in MTS patients in order to avoid potential complications and the permanent consequences of intraluminal spur development. Currently, there is no diagnostic criteria in place to confirm a diagnosis of MTS. Imaging techniques such as CT, IVUS, MRV, and ascending venography have been useful in verifying a diagnosis; conversely, ultrasonography and pleythysmography, while useful in evaluating DVT and venous obstructions, cannot effectively be used to diagnose MTS and are best used in conjunction with other imaging techniques. Overall, the identification of MTS relies on both clinical and image findings, and more studies are needed in order to develop a comprehensive protocol for both.

## REFERENCES


1 **McDermott S**, Oliveira G, Ergül E, Brazeau N, Wicky S, Oklu R. May-Thurner syndrome: can it be diagnosed by a single MR venography study? *Diagn Interv Radiol* 2013; **19**: 44-48 [PMID: 22801870 DOI: 10.4261/1305-3825.DIR.5939-12.1]

2 **Heijmen RH**, Bollen TL, Duyndam DA, Overtoom TT, Van Den Berg JC, Moll FL. Endovascular venous stenting in May-Thurner syndrome. *J Cardiovasc Surg* (Torino) 2001; **42**: 83-87 [PMID: 11292912]

3 **Oğuzkurt L**, Ozkan U, Tercan F, Koç Z. Ultrasonographic diagnosis of iliac vein compression (May-Thurner) syndrome. *Diagn Interv Radiol* 2007; **13**: 152-155 [PMID: 17846991]

4 **O'Sullivan GJ**, Semba CP, Bittner CA, Kee ST, Razavi MK, Sze DY, Dake MD. Endovascular management of iliac vein compression (May-Thurner) syndrome. *J Vasc Interv Radiol* 2000; **11**: 823-836 [PMID: 10928517 DOI: 10.1016/S1051-0443(07)61796-5]

5 **Hurst DR**, Forauer AR, Bloom JR, Greenfield LJ, Wakefield TW, Williams DM. Diagnosis and endovascular treatment of iliocaval compression syndrome. *J Vasc Surg* 2001; **34**: 106-113 [PMID: 11436082 DOI: 10.1067/mva.2001.114213]

6 **Knipp BS**, Ferguson E, Williams DM, Dasika NJ, Cwikiel W, Henke PK, Wakefield TW. Factors associated with outcome after interventional treatment of symptomatic iliac vein compression syndrome. *J Vasc Surg* 2007; **46**: 743-749 [PMID: 17903652 DOI: 10.1016/j.jvs.2007.05.048]

7 **Shebel ND**, Whalen CC. Diagnosis and management of iliac vein compression syndrome. *J Vasc Nurs* 2005; **23**: 10-17; quiz 18-19 [PMID: 15741959 DOI: 10.1016/j.jvn.2004.12.001]

8 **Brazeau NF**, Harvey HB, Pinto EG, Deipolyi A, Hesketh RL, Oklu R. May-Thurner syndrome: diagnosis and management. *Vasa* 2013; **42**: 96-105 [PMID: 23485836 DOI: 10.1024/0301-1526/a000252]

9 **Cockett FB**, Thomas ML, Negus D. Iliac vein compression.--Its relation to iliofemoral thrombosis and the post-thrombotic syndrome. *Br Med J* 1967; **2**: 14-19 [PMID: 6020994 DOI: 10.1136/bmj.2.5543.14]

10 **Forauer AR**, Gemmete JJ, Dasika NL, Cho KJ, Williams DM. Intravascular ultrasound in the diagnosis and treatment of iliac vein compression (May-Thurner) syndrome. *J Vasc Interv Radiol* 2002; **13**: 523-527 [PMID: 11997362 DOI: 10.1016/S1051-0443(07)61535-8]

11 **Ibrahim W**, Al Safran Z, Hasan H, Zeid WA. Endovascular management of may-thurner syndrome. *Ann Vasc Dis* 2012; **5**: 217-221 [PMID: 23555515 DOI: 10.3400/avd.cr.12.00007]

12 **Patel NH**, Stookey KR, Ketcham DB, Cragg AH. Endovascular management of acute extensive iliofemoral deep venous thrombosis caused by May-Thurner syndrome. *J Vasc Interv Radiol* 2000; **11**: 1297-1302 [PMID: 11099239 DOI: 10.1016/S1051-0443(07)61304-9]

13 **Wolpert LM**, Rahmani O, Stein B, Gallagher JJ, Drezner AD. Magnetic resonance venography in the diagnosis and management of May-Thurner syndrome. *Vasc Endovascular Surg* 2002; **36**: 51-57 [PMID: 12704525 DOI: 10.1177/153857440203600109]

14 **Kibbe MR**, Ujiki M, Goodwin AL, Eskandari M, Yao J, Matsumura J. Iliac vein compression in an asymptomatic patient population. *J Vasc Surg* 2004; **39**: 937-943 [PMID: 15111841 DOI: 10.1016/j.jvs.2003.12.032]

15 **Moreland NC**, Ujiki M, Matsumura JS, Morasch MD, Eskandari MK, Pearce WH, Kibbe MR. Decreased incidence of left common iliac vein compression in patients with abdominal aortic aneurysms. *J Vasc Surg* 2006; **44**: 595-600 [PMID: 16950440 DOI: 10.1016/j.jvs.2006.05.046]

16 **Oguzkurt L**, Ozkan U, Ulusan S, Koc Z, Tercan F. Compression of the left common iliac vein in asymptomatic subjects and patients with left iliofemoral deep vein thrombosis. *J Vasc Interv Radiol* 2008; **19**: 366-370; quiz 371 [PMID: 18295695 DOI: 10.1016/j.jvir.2007.09.007]

17 **Liu Z**, Gao N, Shen L, Yang J, Zhu Y, Li Z, Si Y. Endovascular treatment for symptomatic iliac vein compression syndrome: a prospective consecutive series of 48 patients. *Ann Vasc Surg* 2014; **28**: 695-704 [PMID: 24559785 DOI: 10.1016/j.avsg.2013.05.019]

18 **Lamba R**, Tanner DT, Sekhon S, McGahan JP, Corwin MT, Lall CG. Multidetector CT of vascular compression syndromes in the abdomen and pelvis. *Radiographics* 2014; **34**: 93-115 [PMID: 24428284 DOI: 10.1148/rg.341125010]

19 **Whiteley M**, Dos Santos S, Harrison C, Holdstock J, Lopez A. Transvaginal duplex ultrasonography appears to be the gold standard investigation for the haemodynamic evaluation of pelvic venous reflux in the ovarian and internal iliac veins in women. *Phlebology* 2014; Epub ahead of print [PMID: 25324278 DOI: 10.1177/0268355514554638]

20 **Zhu QH**, Zhou CY, Chen Y, Wang J, Mo HY, Luo MH, Huang W, Yu XF. Percutaneous manual aspiration thrombectomy followed by stenting for iliac vein compression syndrome with secondary acute isolated iliofemoral deep vein thrombosis: a prospective study of single-session endovascular protocol. *Eur J Vasc Endovasc Surg* 2014; **47**: 68-74 [PMID: 24183245 DOI: 10.1016/j.ejvs.2013.09.030]

21 **Chung JW**, Yoon CJ, Jung SI, Kim HC, Lee W, Kim YI, Jae HJ, Park JH. Acute iliofemoral deep vein thrombosis: evaluation of underlying anatomic abnormalities by spiral CT venography. *J Vasc Interv Radiol* 2004; **15**: 249-256 [PMID: 15028809 DOI: 10.1097/01.RVI.0000109402.52762.8D]

22 **Oguzkurt L**, Tercan F, Pourbagher MA, Kizilkilic O, Turkoz R, Boyvat F. Computed tomography findings in 10 cases of iliac vein compression (May-Thurner) syndrome. *Eur J Radiol* 2005; **55**: 421-425 [PMID: 16129251 DOI: 10.1016/j.ejrad.2004.11.002]

23 **Gurel K**, Gurel S, Karavas E, Buharalıoglu Y, Daglar B. Direct contrast-enhanced MR venography in the diagnosis of May-Thurner syndrome. *Eur J Radiol* 2011; **80**: 533-536 [PMID: 20570076 DOI: 10.1016/j.ejrad.2010.04.033]

24 **Binkert CA**, Schoch E, Stuckmann G, Largiader J, Wigger P, Schoepke W, Zollikofer CL. Treatment of pelvic venous spur (May-Thurner syndrome) with self-expanding metallic endoprostheses. *Cardiovasc Intervent Radiol* 1998; **21**: 22-26 [PMID: 9473541 DOI: 10.1007/s002709900205]

25 **Ahmed HK**, Hagspiel KD. Intravascular ultrasonographic findings in May-Thurner syndrome (iliac vein compression syndrome). *J Ultrasound Med* 2001; **20**: 251-256 [PMID: 11270529]

26 **Canales JF**, Krajcer Z. Intravascular ultrasound guidance in treating May-Thurner syndrome. *Tex Heart Inst J* 2010; **37**: 496-497 [PMID: 20844634]

27 **McLafferty RB**. The role of intravascular ultrasound in venous thromboembolism. *Semin Intervent Radiol* 2012; **29**: 10-15 [PMID: 23450229 DOI: 10.1055/s-0032-1302446]

28 **Raju S**, Neglen P. High prevalence of nonthrombotic iliac vein lesions in chronic venous disease: a permissive role in pathogenicity. *J Vasc Surg* 2006; **44**: 136-143; discussion 144 [PMID: 16828437 DOI: 10.1016/j.jvs.2006.02.065]

29 **Neglén P**, Raju S. Intravascular ultrasound scan evaluation of the obstructed vein. *J Vasc Surg* 2002; **35**: 694-700 [PMID: 11932665 DOI: 10.1067/mva.2002.121127]

30 **Kim JY**, Choi D, Guk Ko Y, Park S, Jang Y, Lee do Y. Percutaneous treatment of deep vein thrombosis in May-Thurner syndrome. *Cardiovasc Intervent Radiol* 2006; **29**: 571-575 [PMID: 16502185 DOI: 10.1007/s00270-004-0165-7]


**P- Reviewer**: Chan WP, Chen F
**S- Editor**: Ji FF **L- Editor**: A **E- Editor**: Jiao XK

World Journal of Radiology

Submit a Manuscript: http://www.wjgnet.com/esps/
Help Desk: http://www.wjgnet.com/esps/helpdesk.aspx
DOI: 10.4329/wjr.v7.i11.382

*World J Radiol* 2015 November 28; 7(11): 382-393
ISSN 1949-8470 (online)


MINIREVIEWS

# Application of positron emission tomography/computed tomography in radiation treatment planning for head and neck cancers

Musaddiq J Awan, Farzan Siddiqui, David Schwartz, Jiankui Yuan, Mitchell Machtay, Min Yao

Musaddiq J Awan, Jiankui Yuan, Mitchell Machtay, Min Yao, Department of Radiation Oncology, Case Comprehensive Cancer Center, University Hospitals and Case Western Reserve University School of Medicine, Cleveland, OH 44106, United States

Farzan Siddiqui, Department of Radiation Oncology, Henry Ford Health System, Detroit, MI 48202, United States

David Schwartz, Department of Radiation Oncology, University of Texas Southwestern Medical Center, Dallas, TX 75390, United States

Author contributions: Awan MJ, Siddiqui F and Yao M contributed equally to this work; Siddiqui F, Schwartz D and Yao M contributed to case examples; Yuan J contributed to the data collection and image process; Awan MJ, Siddiqui F, Schwartz D, Yuan J, Machtay M, and Yao M all contributed to writing and editing the paper.

Conflict-of-interest statement: The authors have no conflicts of interest to disclose related to the publication of this work.



Correspondence to: Min Yao, MD, PhD, Professor, Department of Radiation Oncology, Case Comprehensive Cancer Center, University Hospitals and Case Western Reserve University School of Medicine, 11100 Euclid Avenue, Cleveland, OH 44106, United States. min.yao@uhhospitals.org
Telephone: +1-216-8443103
Fax: +1-216-8442005

Received: May 29, 2015
Peer-review started: June 1, 2015
First decision: June 18, 2015
Revised: July 8, 2015
Accepted: September 16, 2015
Article in press: September 18, 2015
Published online: November 28, 2015

## Abstract

18-fluorodeoxygluocose positron emission tomography/computed tomography ($^{18}$FDG-PET/CT) provides significant information in multiple settings in the management of head and neck cancers (HNC). This article seeks to define the additional benefit of PET/CT as related to radiation treatment planning for squamous cell carcinomas (SCCs) of the head and neck through a review of relevant literature. By helping further define both primary and nodal volumes, radiation treatment planning can be improved using PET/CT. Special attention is paid to the independent benefit of PET/CT in targeting mucosal primaries as well as in detecting nodal metastases. The utility of PET/CT is also explored for treatment planning in the setting of SCC of unknown primary as PET/CT may help define a mucosal target volume by guiding biopsies for examination under anesthesia thus changing the treatment paradigm and limiting the extent of therapy. Implications of the use of PET/CT for proper target delineation in patients with artifact from dental procedures are discussed and the impact of dental artifact on CT-based PET attenuation correction is assessed. Finally, comment is made upon the role of PET/CT in the high-risk post-operative setting, particularly in the context of radiation dose escalation. Real case examples are used in these settings to elucidate the practical benefits of PET/CT as related to radiation treatment planning in HNCs.

**Key words:** Head and neck cancer; Radiation treatment planning; Computed tomography; Fluorodeoxygluocose positron emission tomography; Imaging

**Core tip:** The 18-fluorodeoxygluocose positron emission tomography ($^{18}$FDG-PET) scan has increasing clinical importance in the management of head and neck cancers. It has also proven useful in treatment planning for radiation therapy. PET scans have utility in tumor volume delineation, the identification of metastatic lymph nodes, the management of carcinoma of unknown primary, dental artifact reduction and high-risk postoperative radiation therapy. Many of these applications of $^{18}$FDG-PET scans are still in the preliminary stages of development and active investigations are ongoing to standardize these processes.

Awan MJ, Siddiqui F, Schwartz D, Yuan J, Machtay M, Yao M. Application of positron emission tomography/computed tomography in radiation treatment planning for head and neck cancers. *World J Radiol* 2015; 7(11): 382-393 Available from: URL: http://www.wjgnet.com/1949-8470/full/v7/i11/382.htm DOI: http://dx.doi.org/10.4329/wjr.v7.i11.382

## INTRODUCTION

Head and neck cancer (HNC) is a significant cause of cancer morbidity and mortality worldwide. Approximately 650000 new HNC are diagnosed annually worldwide with approximately half of this number resulting in deaths[1]. The majority of HNCs worldwide are squamous cell carcinomas (SCCs) related to tobacco abuse, however the incidence of head and neck SCCs resulting from infection with the human papilloma virus (HPV) is rising. The prognosis for HPV-negative (tobacco-related) cancers is inferior to that of HPV-positive cancers. Undoubtedly, radiation therapy plays a central role in the management of the majority of HNC patients and meticulous radiation treatment planning is required to ensure high rates of cure as well as in limiting toxicity. This is particularly important for HPV-positive oropharyngeal cancer patients as these patients are generally younger and with few co-morbidities and thus are expected to live longer with long-term radiation complications. Most HNCs present in a locally advanced stage and primary management takes one of the two courses: surgical resection with or without adjuvant radiation based upon pathologic features or definitive radiation therapy with or without concurrent chemotherapy saving surgery as a salvage option.

Modern radiation therapy is delivered using highly conformal technologies including three-dimensional conformal radiotherapy, intensity modulated radiation therapy (IMRT) and most recently IMRT with image guidance. Target delineation on treatment planning computed tomography (CT) scans is a central part of the treatment process in both cure and limiting toxicity. This is particularly important in the era of IMRT, in which steep radiation dose falloff is achievable within millimeters.

A risk-stratified approach is taken in radiation treatment planning in HNCs. Areas of high-risk of disease spread and gross disease receive a high dose of radiation (usually 66-70 Gy). Other areas, including those of intermediate-risk of disease spread and grossly uninvolved nodal regions in which tumor recurrence may occur, receive lower doses of radiation (56-60 Gy and 50-56 Gy, respectively). Clinical data from physical examinations and diagnostic laryngoscopies, as well as pathologic data and multimodality imaging using CT, magnetic resonance imaging (MRI), ultrasound and positron emission tomography (PET) all contribute to the target delineation and treatment planning process. This article seeks to define the additional benefit of the utility of 18-fluorodeoxyglucose ($^{18}$FDG) PET/CT scans in radiation treatment planning particularly as related to five areas: (1) Primary gross tumor and nodal volume (GTV) delineation; (2) Identification of involved metastatic lymph nodes; (3) Management of SCCs of unknown primary in the head and neck; (4) Utility in accounting for dental artifact; and (5) High-risk post-operative radiation (PORT).

## DELINEATION OF THE PRIMARY AND NODAL GTV

$^{18}$FDG-PET can help clarify the extent of primary tumor and eliminate unnecessary treatment volumes that may appear as abnormal on CT or MRI imaging. Significant variations have been noted in both primary tumor and lymph nodal volumes based on the diagnostic imaging modality(ies) used to define these. Iodinated-contrast-enhanced CT scans remain the imaging modality of choice due to their widespread availability in radiation oncology departments worldwide. Additionally, CT scans have a short image acquisition time and thus do not suffer from the image quality degradation that may result from longer acquisition times and normal breathing or swallowing motion. They provide sufficient anatomical details of the gross tumor and involved lymph nodes, provide electron density information for attenuation correction for treatment planning purposes, and require less end-user training for image interpretation relative to other modalities. Many reports have investigated the impact of additional PET imaging on primary and lymph nodal volume definition for radiation treatment planning purposes. Most of these reports have found major discrepancies between CT-based and PET-based volumes resulting in clinically significant implications for radiation therapy.

### *Studies assessing the addition of PET to CT-based planning*

A number of studies have assessed the impact of the addition of PET in the manual segmentation of HNC GTVs. In an analysis of 12 HNC patients comparing CT

based GTV (GTV-CT) and PET based GTV (GTV-PET), the GTV increased or decreased by 25% or more because of PET in 17% and 33% of cases, respectively[2]. In this report, the primary and nodal volumes were not assessed separately.

In another study, Heron *et al*[3] did analyze the changes in primary and nodal volumes separately and noted a change in GTV delineation in 80% of cases with the use of PET scans. For the primary site, the GTV was larger in 14% and smaller in 66% of cases based on PET scans. Interestingly, for the abnormal lymph nodes, the volume was larger in 33% of cases and smaller in 14% of cases. The average ratio of GTVs for the CT-defined and PET-defined volumes was 3.1 (range, 0.3-23.6), whereas for abnormal nodes was 0.7 (range, 0-4). Hence, tumor volumes for the primaries were significantly larger as delineated on CT than on PET but not for nodal regions suggesting a larger benefit in delineating the primary tumor with the addition of PET.

A similar discrepancy between CT-GTV and PET-GTV was noted by Guido *et al*[4]. Thirty-eight consecutive HNC patients underwent treatment planning CTs with intravenous contrast enhancement. A radiation oncologist defined all GTVs using both the PET/CT and CT scans. The CT-GTV was larger than PET-GTV in 92% cases. Unlike the previous study, no statistically significant difference was seen between these volumes for primary and nodal sites.

Variations in target delineation with the addition of PET/CT may also affect treatment planning. In a study of a group of 40 patients, Paulino *et al*[5] noted changes in the PET-GTV in 37 cases (30 smaller, 7 larger). IMRT plans were generated based on the CT-based volumes and dosimetric analysis was performed to examine the adequacy of coverage for the PET-based volume in these IMRT plans. The volume of PET-GTV receiving at least 95% of the prescribed dose was 100% and 95%-99% in 20 and 10 cases, respectively. Thus, inadequate coverage (< 95% of the PET-GTV receiving the prescribed dose) was seen in 25% of cases.

A major reason for these variations in study results is the subjectivity associated with $^{18}$FDG-PET image interpretation and consequent user dependence on how the GTV is defined using PET images. The potential impact of interobserver and intraobserver variation was studied by Breen *et al*[6] Eight experienced observers (6 head and neck oncologists and 2 neuroradiologists) outlined the primary GTV for 10 patients. There was a very high agreement between and within observers on GTVs derived from contrast-enhanced CT scans. However, there was less reliability noted when PET/CT scans were used for outlining the GTV. In another similar analysis[7], 4 physicians (2 neuroradiologists and 2 radiation oncologists) contoured GTVs in 16 patients on the basis of the CT alone, and then on PET/CT fusion. A high degree of variation was noted across physicians for the CT volumes ($P$ = 0.09) and significant variation was seen for the PET/CT volumes ($P$ = 0.0002). Observer variation in lymph nodal volume outlining was not assessed in either of these studies.

### *Automated techniques of PET-GTV delineation*

Due to limitations in how different experienced physicians define the GTVs for various cases it is very difficult to perform interinstitutional comparative studies and arrive at any meaningful conclusions on the utility of PET scans for head and neck treatment planning. To overcome these interobserver and intraobserver variations, many attempts have been made to automate the process of volume definition using PET scans. Various groups have attempted to describe "thresholding" or "segmentation" techniques to make the process more objective and eliminate or reduce the subjectivity associated with the use of PET imaging data.

Schinagl *et al*[8] evaluated PET based GTVs derived using 5 different segmentation techniques: visual interpretation, applying an isocontour of a standardized uptake value (SUV) of 2.5, using a fixed threshold of 40% and 50% of the maximum signal intensity, and applying an adaptive threshold based on the signal-to-background ratio. Seventy-eight patients with Stages Ⅱ-Ⅳ SCC of the head and neck were studied. The primary tumor was delineated on CT. The GTV method of applying an isocontour of a SUV of 2.5 failed to provide successful delineation in 45% of cases. However, the other segmentation methods resulted in PET-GTVs that were smaller than that seen on the CT scan. Additionally, the PET scans frequently showed tumor extension outside that seen on the CT scans. The authors concluded that none of the segmentation methods provided a satisfactory result.

In a subsequent publication, the authors used the same data set of 78 patients to assess whether PET scans could be used for target volume definition for metastatic lymph nodes in the head and neck region[9]. On the CT scans, lymph nodes measuring 7-10 mm were labeled as "marginally enlarged" and those > 10 mm were "enlarged". Eight different PET segmentation methods were used to identify these nodes: visual interpretation, applying fixed thresholds at SUV of 2.5 and at 40% and 50% of the maximum signal intensity of the primary tumor and applying a variable threshold based on the signal-to-background ratio. Additionally, these same thresholds were acquired using the signal of the lymph node as the threshold reference. Based on the CT scan imaging, 208 lymph nodes were > 7 mm while 108 were >10 mm. A large percentage of these lymph nodes were not identified by the segmentation methods when normalized to the primary tumor PET-SUV. The results were better when the thresholds were set based on the lymph node SUV values. Due to these limitations, the authors concluded that until proper validation of $^{18}$FDG-PET based segmentation tools is done it should not be recommended for target volume definition of metastatic lymph nodes in routine clinical practice.

Another recent prospective study in 19 patients with 39 lesions used the signal-to-background ratio

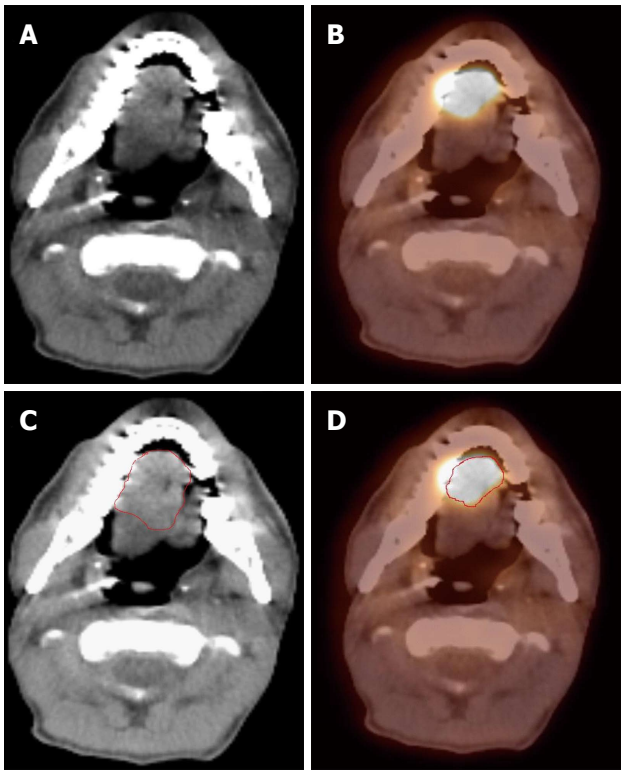


**Figure 1 Positron emission tomography/computed tomography improves gross tumor and nodal volume delineation in a patient with oral tongue cancer.** A: In the CT image, the tumor is difficult to separate from the soft tissues of the tongue; B: In the PET image, there is sharp demarcation of the primary tumor; C: The GTV is outlined in red based on CT scan; D: The GTV outlined in red based on $^{18}$FDG PET/CT is much smaller. $^{18}$FDG-PET/CT: 18-fluorodeoxygluocose positron emission tomography/computed tomography; GTV: Gross tumor and nodal volume.

thresholding method to define tumor volumes. It concluded that methods that rely mainly on $SUV_{max}$ for thresholding are very sensitive to partial volume effects and may provide unreliable results when applied on small lesions[10]. Thus, automated thresholding and segmentation methods have not yet yielded promising results in PET-GTV delineation.

### *Pathologic correlation of PET-GTV volumes*

Investigators have also evaluated the pathologic correlates to PET imaging findings in HNC patients. Daisne *et al*[11] compared delineation of tumor volumes on MRI, CT and PET in multiple patients with HNCs. Average PET-GTVs (20.3 cc) were smaller than those derived from MR (27.9 cc) or CT (32 cc). Additionally, PET-GTVs contained additional volume not delineated on either primary MR or CT images. For 9 patients with laryngeal cancer who underwent total laryngectomy after multimodality imaging in this cohort, pathologic tumor volumes were significantly smaller than the estimated image volumes on all modalities studied. The average surgical specimen tumor volume measured 12.6 cc while tumor volume was measured as 16.3 cc, 20.8 cc and 23.8 cc on PET, CT and MRI images, respectively.

In a similar radio-pathologic correlative study, Schinagl *et al*[12] identified 28 lymph nodes in 12 HNC patients and looked at the ability of various PET segmentation methods to predict pathologic size after lymph node dissection. Nodal volumes on CT scans and visual interpretation of PET scans showed good correlations with the pathological volume. The authors noted that $^{18}$FDG-PET scans are valuable for detection of lymph nodes for staging purposes but provide no additional information over CT scans for outlining radiotherapy target volumes.

### *Guidelines for the utility of PET/CT for GTV delineation*

There is currently no consensus on the methods of auto-segmentation, volume definition and the overall utility of $^{18}$FDG-PET scans in RT of HNCs. This remains an active area of research and development. Currently, we use $^{18}$FDG-PET co-registered with the simulation CT images to identify the tumor, contour the GTV and subsequently modify the GTV volume with the CT images, especially with contrast-enhancing CT images. $^{18}$FDG-PET is especially helpful when it is difficult to separate the tumor from surrounding soft tissue and muscle in CT imaging, such as tumor in the oral tongue or oropharynx. Figure 1 shows a patient with oral tongue cancer, comparing CT *vs* PET. The GTV based on CT (Figure 1C) is much larger than that based on $^{18}$FDG-PET (Figure 1D).

$^{18}$FDG-PET is also very helpful in identifying tumor extent that is not detectable on either CT or MR images. In particular, HNC patients often have synchronous second primaries. $^{18}$FDG-PET can help detect additional primary disease to be included in the high dose radiation field. Figure 2 shows a patient who presented with a right lateral oral tongue cancer. PET/CT revealed additional primary cancers in the soft palate and in the cervical esophagus (Figure 2A). Thus, the IMRT plan delivered 70 Gy to all of these primary tumors (Figure 2B-D).

## IDENTIFICATION OF INVOLVED LYMPH NODES THAT ARE MISSED ON CT/MR

In addition to helping better delineate primary tumors, $^{18}$FDG-PET can clarify the involvement of metastatic lymph nodes in HNC patients. Standard CT and MR criteria for malignant cervical lymph nodes include size, shape, margins, and internal architecture, with size as the main criteria[13]. These criteria for CT and MR may under- or over-diagnose lymph node involvement and nodal stage in patients, resulting in 20%-30% false positive and false negative results[13]. The consequence of such errors may have a significant impact on treatment planning in HNC; in particular, small malignant lymph nodes may be under-dosed using CT or MRI criteria alone.

PET sensitivity and specificity for predicting involved nodes has been estimated at over 90%[14]. Heron *et*

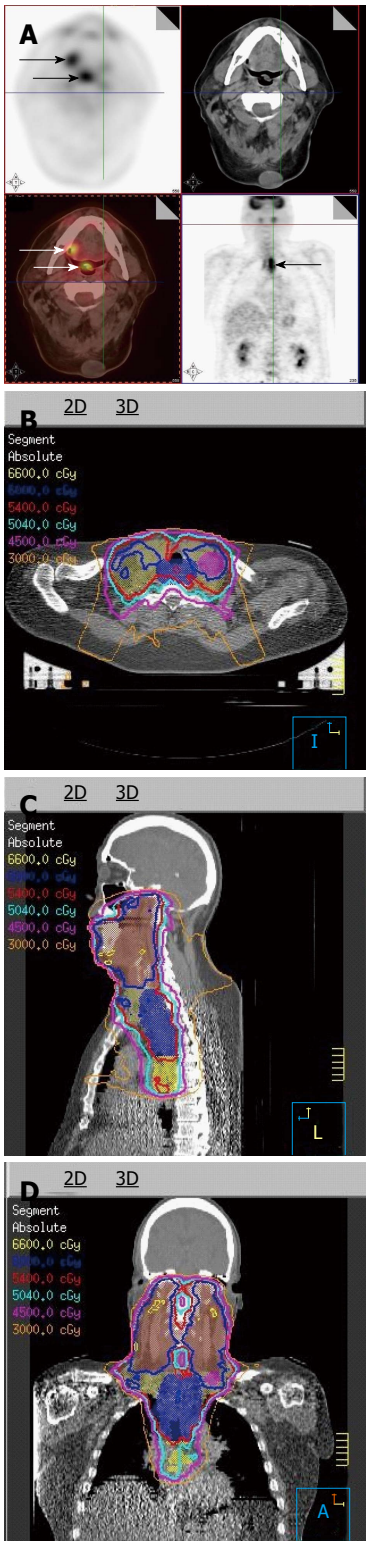


**Figure 2 Positron emission tomography/computed tomography discovers multiple primaries in a patient with a right lateral tongue cancer.** A: PET/CT images revealed that in addition to an oral tongue tumor, this patient had a primary tumor of the soft palate (inferior white arrow) as well as the cervical esophagus (black arrow); B-D: The IMRT plan for this patient demonstrates all three tumors covered in the high dose CTV. PET/CT: Positron emission tomography/computed tomography; IMRT: Intensity modulated radiation therapy.

*al*[3] reported that the addition of $^{18}$FDG-PET to CT-based treatment planning increased the number of abnormal nodes contoured in 5 of 21 (24%) patients in a small institutional study. In another study, Koshy *et al*[15] reported significant changes in TNM staging affecting tumor volume delineation with the addition of $^{18}$FDG-PET to CT alone. Amongst a group of 36 patients in this study, 6 patients had a change in N-stage with the use of PET/CT relative to CT alone: 3 patients were upstaged including one to bilateral disease, while 3 other patients were downstaged to N0 disease. These changes in nodal staging are not trivial, as grossly involved nodal disease will receive radiation doses of up to 70 Gy, while node-negative disease may receive an elective radiation dose of 50-56 Gy or no radiation therapy at all.

In a prospective study by Schwartz *et al*[16] evaluating the feasibility of PET/CT based treatment planning, 63 patients underwent PET/CT simulation and 20 patients underwent neck dissection after a PET/CT simulation. $^{18}$FDG-PET correctly identified all 17 diseased heminecks and 9 negative heminecks. Additionally, 26/27 pathologically involved nodal levels were identified with positive predictive value (PPV) and negative predictive values (NPV) for nodal staging at 98.5% and 96% respectively. This affirms the high level of accuracy by which $^{18}$FDG-PET can be used to assess nodal disease. Further, in comparing CT-based and PET/CT-based treatment planning, PET/CT-based planning directly improved parotid and laryngeal doses, thus theoretically sparing patients from long-term toxicities of xerostomia and dysphagia.

Figure 3 illustrates a patient with nasopharyngeal cancer. Initial staging by CT and MRI was T1N0, but an $^{18}$FDG-PET scan revealed a hypermetabolic level Ⅱ lymph node which did not meet size criteria for malignancy by CT/MRI (Figure 3A-D). Fine needle aspiration (FNA) of this node confirmed metastatic disease. Thus, this lymph node was treated to a high dose of radiation (Figure 3E-H) and concurrent chemotherapy was indicated.

PET/CT has especially been helpful in detecting lymph nodes at a far distance from the primary tumor or in the contralateral neck, specifically when the lymph node has not reached size criteria by CT/MRI (Figure 4). $^{18}$FDG-PET is also very helpful in detecting involved lymph nodes in the lower neck in which CT visualization is hindered by complex muscular and vascular structures (Figure 5). Thus, additional highly suspicious nodes could be included in the high-dose dose field with the addition of $^{18}$FDG-PET.

Finally, well-lateralized tonsil cancer is often treated to the ipsilateral side to reduce toxicities. However, before subjecting the patient to ipsilateral radiation, it is prudent to rule out any contralateral suspicious nodes. Because of the highly sensitivity of $^{18}$FDG-PET to detect metastatic lymph nodes, it should be the best modality in selecting patients for this treatment (Figure 6).

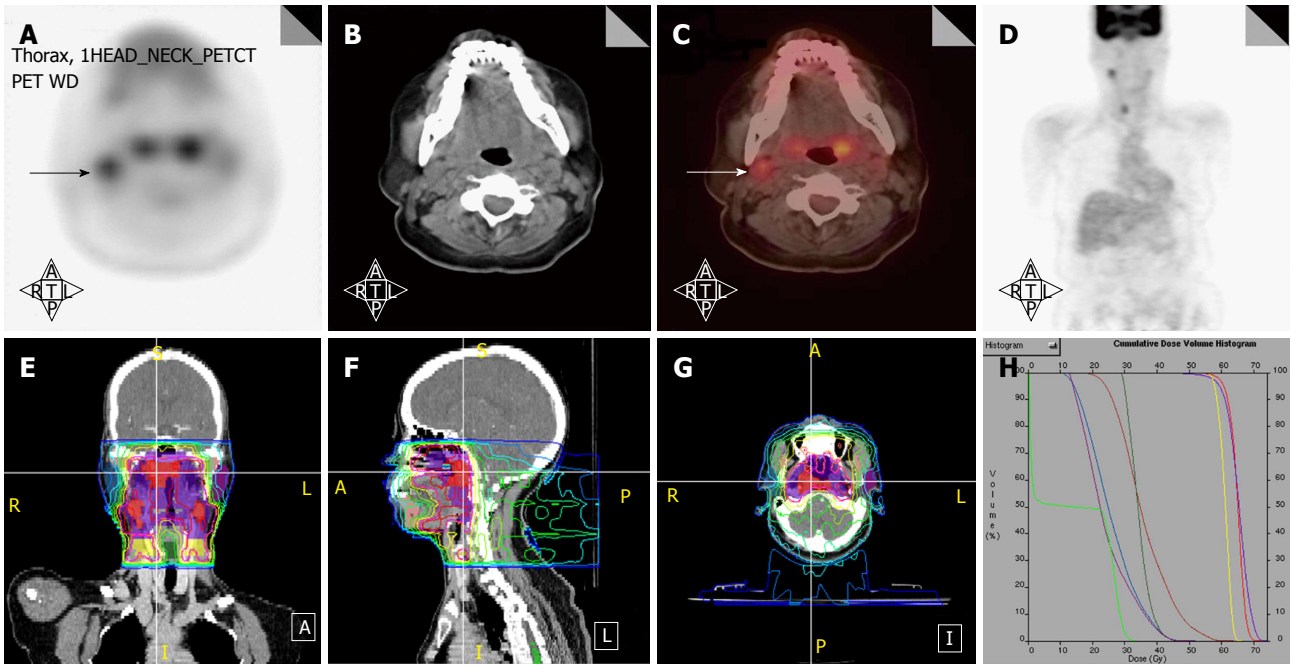


**Figure 3 Positron emission tomography/computed tomography upstages a T1 nasopharyngeal cancer patient from N0 to N1.** A-D: PET/CT images reveal that in addition to the T1 nasopharyngeal primary, there is increased FDG uptake in a level II node which was 1.0 cm in size (arrows). FNA of this node confirmed metastatic carcinoma. Thus, the patient was upstaged as T1N1 and treated with concurrent chemotherapy with IMRT; E-H: The IMRT plan for this patient treated the right level II node to a dose of 70 Gy. IMRT: Intensity modulated radiation therapy; PET/CT: Positron emission tomography/computed tomography; FDG: Fluorodeoxygluocose.

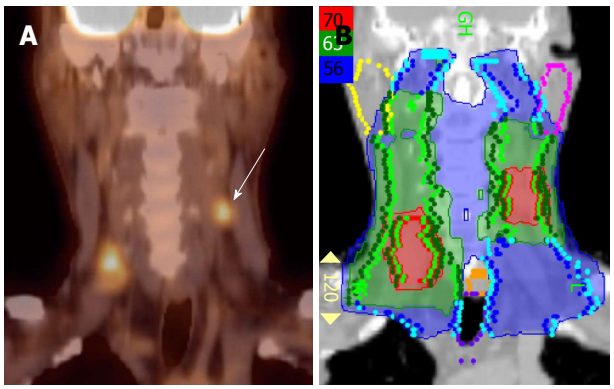


**Figure 4 Positron emission tomography/computed tomography extends the high dose CTV contralaterally in a patient with a T2N2B base of tongue cancer.** A: PET/CT reveals a contralateral level III node (white arrow), and thus, the patient was upstaged as T2N2C; B: An IMRT plan of this patient showing that this node was treated to 70 Gy and contralateral levels II and III were treated to 63 Gy. IMRT: Intensity modulated radiation therapy; PET/CT: Positron emission tomography/computed tomography.

## UNKNOWN PRIMARY OF THE HEAD AND NECK

Between 2% and 9% of patients with HNC present with an enlarged cervical node without a definitive site of origin of the primary tumor by clinical examination and routine imaging studies[17]. This entity is called HNC of unknown primary (HNCUP). As most HNCUPs are SCCs[18], patients presenting with this entity undergo an examination under anesthesia (EUA) of the mucosal surface of the upper aerodigestive tract as well as directed biopsies of the nasopharynx and oropharynx if no suspicious lesion is noted during EUA. Additionally, ipsilateral or bilateral tonsillectomies may be performed for diagnostic purposes. Approximately 50% of primaries are detected in this manner[19].

PET/CT has been shown to be valuable in the work up and in identifying the primary tumor in patients with unknown primary. A systematic review of 16 studies of 302 patients by Rusthoven *et al*[20] validated the benefit of $^{18}$FDG-PET in HNCUP. The sensitivity, specificity and accuracy of $^{18}$FDG-PET in detecting unknown primary tumors were 88.3%, 74.9% and 78.8%. Additionally, $^{18}$FDG-PET detected 24.5% of primary tumors not apparent after traditional workup. The authors also noted that $^{18}$FDG-PET has a similar benefit in detecting additional occult nodal disease and metastases in the HNCUP population with a 15.9% and 11.2% detection rate, respectively.

In a prospective study, 20 patients with HNCUP underwent conventional workup prior to EUA[21]. PET/CT was performed, and the surgeons performing EUA were blinded to the PET results. EUAs and traditional random biopsies were performed prior to the surgeon viewing the PET/CT. After EUA and biopsies, the surgeon was shown the PET/CT intraoperatively and further biopsies were obtained according to the $^{18}$FDG-PET results. PET/CT increased the detection of the primary site from 25% to 55%. This suggests that PET/CT directed biopsy is superior to traditional random biopsy in detecting a primary tumor.

Radiation treatment is the main treatment modality in HNCUP, but radiation volumes vary drastically

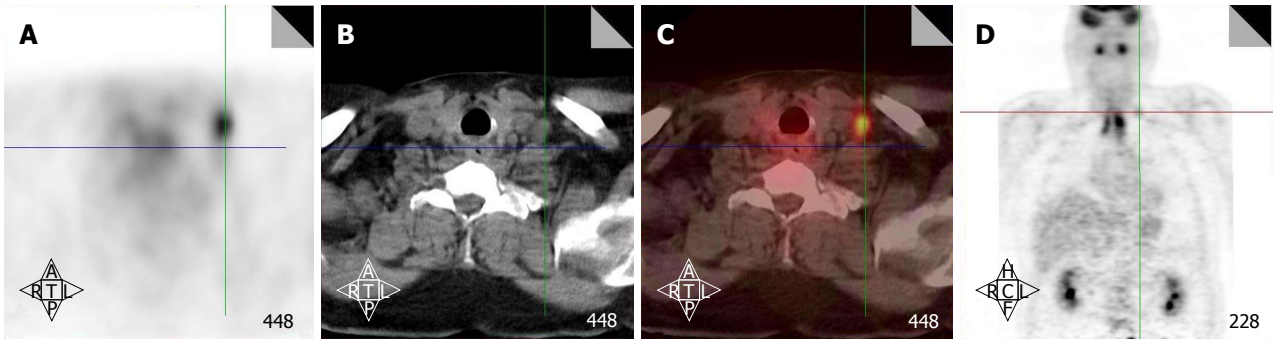


**Figure 5 Positron emission tomography/computed tomography detects a low neck lymph node involved by metastasis.** Increased FDG uptake in the low neck reveals a metastatic lymph node which would otherwise be difficult to detect because of the presence of muscular and vascular structures in this region of the neck (A-D). FDG: Fluorodeoxygluocose.

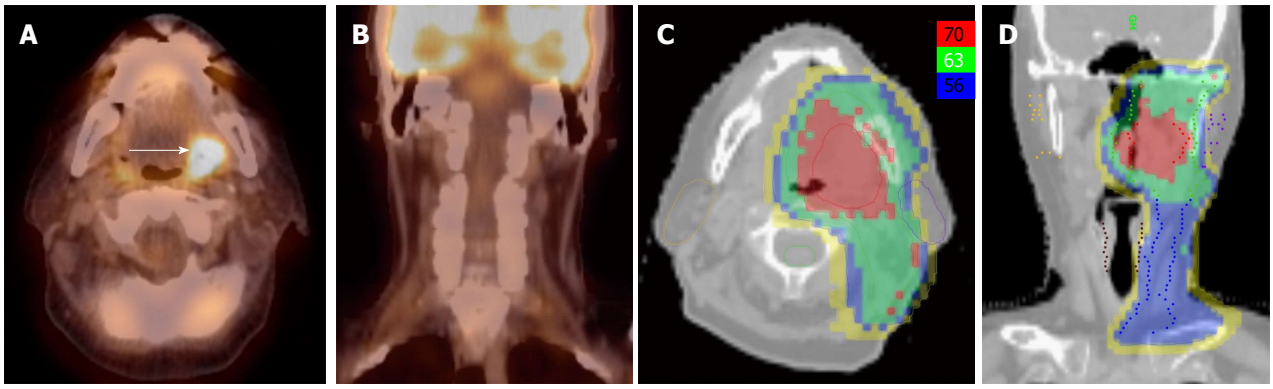


**Figure 6 Positron emission tomography/computed tomography allows for unilateral tonsil cancer treatment in a patient with a T2N0 left tonsil cancer.** A, B: PET/CT shows no evidence of lymph node metastasis in the contralateral (right) neck; C, D: An IMRT plan of the radiation treatment plan showing effective contralateral sparing. IMRT: Intensity modulated radiation therapy; PET/CT: Positron emission tomography/computed tomography.

between institutions and no standard has been defined. Radiation treatment may be directed to either the ipsilateral involved neck or to the bilateral neck, and may include pan-mucosal irradiation to areas that may harbor a microscopic primary tumor including the nasopharynx, oropharynx, larynx, and hypopharynx. Identifying the primary tumor is therefore critical and may allow tailoring the radiation volume according to the primary disease, thus avoiding high dose radiation to unnecessary areas and reducing toxicities of the treatment.

Figure 7 illustrates a patient who presented with multiple left neck nodes with FNA confirming SCC. Conventional workup including EUA and traditional biopsies failed to identify the primary tumor. PET/CT showed a hypermetabolic focus in the left base of tongue corresponding to the primary tumor. This patient was treated as a base of tongue cancer and thus other mucosal areas including the larynx and hypopharynx were spared from high dose radiation.

## ACCOUNTING FOR DENTAL ARTIFACTS

Artifact from amalgam-based fillings and other dental procedures may significantly distort and hinder CT-based target delineation for primary tumors in HNCs. Though artifact reduction techniques exist and have been used to improve the quality of CT-based target delineation and radiation treatment planning, many facilities may not have access to software to reduce dental artifacts on head and neck treatment planning CTs[22].

CT-based attenuation correction is used to improve spatial resolution from PET imaging. Gamma rays produced after positron emission are affected by tissue heterogeneity, and utilizing CT data in addition to raw PET data improves spatial and quantitative accuracy of PET imaging[23]. Multiple authors have addressed the issue of attenuation correction in the context of metallic dental artifact. A study by Kamel *et al*[24] compared CT-based attenuation correction with Ge-68 PET-based attenuation correction in patients with metallic artifact and demonstrated quantitative value differences in regions of dental artifact raising the question of the impact of dental artifact on CT-based attenuation correction. Goerres *et al*[25] confirmed that $^{18}$FDG-PET artifacts are indeed generated adjacent to dental artifact using CT-based correction using a similar methodology of Ge-68 PET-based attenuation correction. However, they also found that these artifacts demonstrated significantly lower $^{18}$FDG-uptake when compared to primary tumor, mitigating the clinical significance of these artifacts in

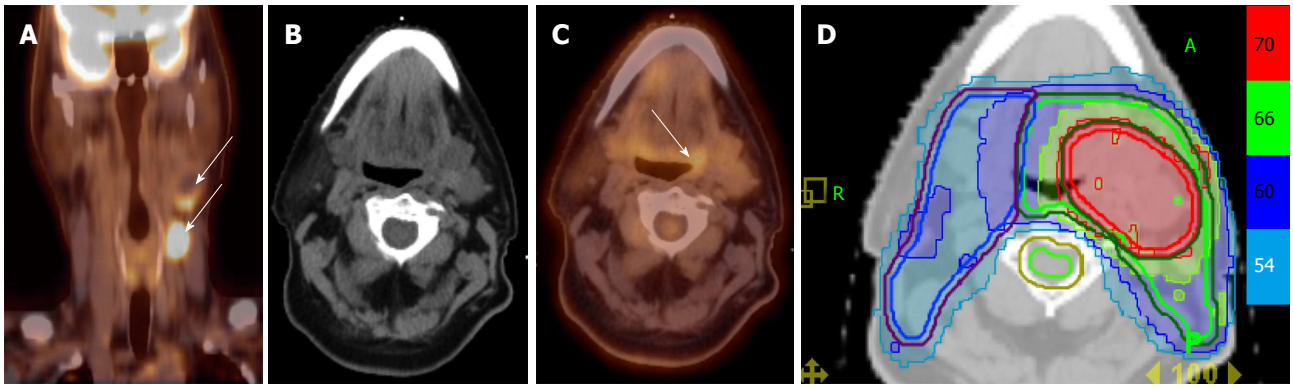


**Figure 7 Positron emission tomography/computed tomography allows for detection for occult primary in a patient with multiple involved left neck nodes.** A: PET/CT showing the initial presentation with multiple enlarged left neck nodes (white arrows); B: A conventional CT scan does not reveal a source of primary cancer; C: PET/CT demonstrated increased FDG uptake in the left base of tongue (white arrow) and a directed biopsy of this area revealed this as the primary site; D: IMRT treatment plan for this patient showing that the left base of tongue was included in the high-dose (70 Gy) volume while sparing uninvolved mucosal areas. IMRT: Intensity modulated radiation therapy; PET/CT: Positron emission tomography/computed tomography.

target delineation. Others have also demonstrated that irrespective of artifact reduction techniques, CT-based PET attenuation correction is robust as metallic artifacts do not propagate into the attenuation correction using CT imaging in HNC patients[26].

As $^{18}$FDG-PET resolution is not significantly modified by dental artifact, it is practical to use $^{18}$FDG-PET to improve target delineation in this context. A study out of Korea compared tumor staging between CT alone, MRI alone, and PET/CT in 37 patients with dental artifact on CT and MRI[27]. PET/CT had improved staging regardless of the presence of dental artifact, and had better specificity in ruling out involvement of the sublingual gland and floor of mouth. Comparing MRI-delineated primary tumor volume and PET-delineated primary tumor volume using an SUV cutoff of 2.5 with post-operative pathologic samples, demonstrated that MRI inferiorly predicted pathologic tumor size relative to PET/CT with an SUV cutoff of 2.5. Thus, PET/CT improved target definition in patients with dental artifact. A previous study also investigated the utility of PET/CT scans in oral cavity cancers comparing 69 patients with dental artifacts and 40 patients without such artifacts[28]. The PET/CT scans detected more tumors as compared to CT scans (95% *vs* 75%). A regression equation was developed equating the pathologic volume of the tumors with the PET volume as defined by a SUV = 3.5.

Recently more algorithms have been developed to use PET/CT imaging in combination with MRI images to reduce the impact of the dental artifacts[29-31].

## UTILITY IN HIGH-RISK PORT

PORT for HNC can improve locoregional control and overall survival in patients with adverse pathologic features, including positive or close margins, extracapsular extension, perineural invasion, lymphovascular invasion, advanced tumor stage (T4), and advanced nodal stage (N2B or higher). Indications for PORT were validated in work by Peters *et al*[32] and further stratified by Ang *et al*[33] at the MD Anderson Cancer Center. Randomized clinical trials from the Radiation Therapy Oncology Group and the European Organization for Research and Treatment of Cancer have shown that concurrent chemotherapy and radiation is significantly better than radiation alone in patients with high risk pathologic features; particularly those with extracapsular nodal extension or positive surgical margins. This was further validated by a pooled analysis of individual patient data from both trials[34-36]. PORT should include the entire postoperative area to a dose between 57.6 and 60 Gy in 30 to 33 fractions. High-risk areas including areas of close or positive post-operative margins or extracapsular nodal extension may also benefit from radiation dose escalation in addition to the radio-sensitizing effect of concurrent chemotherapy[37]. Radiation treatment to these high-risk areas is often escalated to 66 Gy.

Defining the radiation treatment targets is very challenging in the post-operative setting due to the anatomical changes after surgical resection and reconstruction especially in patients who have free flap reconstruction. Information including pre-operative imaging, pre-operative physical examination or endoscopy, surgical and pathologic findings, and post-operative imaging should be incorporated in target delineation in PORT and often requires a multidisciplinary approach with coordination between radiation oncologists, surgeons, radiologists, and pathologists. For patients who have pre-operative $^{18}$FDG-PET scans, registration of these PET images to postoperative simulation CT images can help to define the tumor beds which are often the high risk areas. Pre-operative PET/CT may be registered to the simulation CT using either rigid or deformable algorithms to provide guidance in assessing areas of high risk of recurrence[38]. Through image registration, the radiation oncologist is able to directly correlate the pre-treatment disease volumes to the post-operative CT imaging, and delineate high-risk areas to be included in the high radiation dose field.

PORT is often delivered 4 to 6 wk after surgery when

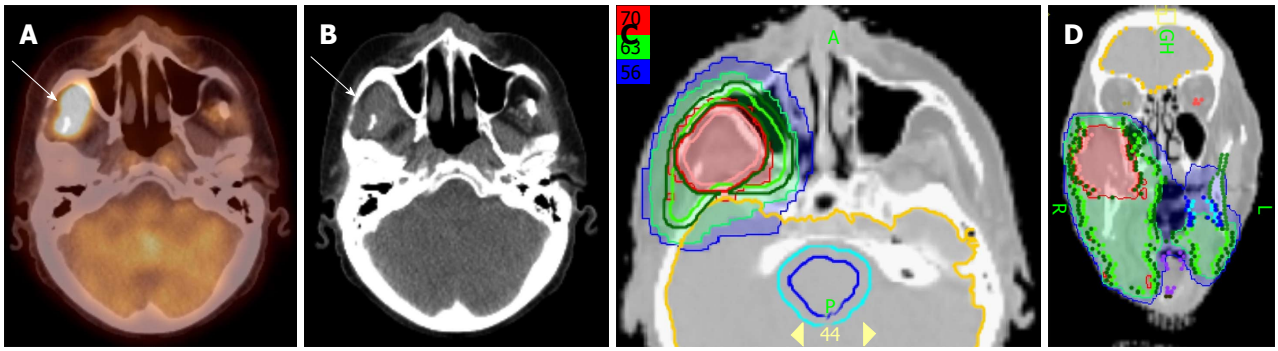


**Figure 8 Positron emission tomography/computed tomography demonstrates tumor recurrence in a patient with a resected T4aN2b right buccal mucosa cancer prior to postoperative radiation.** A-B: PET-CT obtained 50 d after surgery before postoperative radiation shows recurrent tumor (white arrow) in the infratemporal fossa; C-D: An IMRT treatment plan for this patient showing the recurrent tumor treated to a definitive radiation dose of 70 Gy rather a typical postoperative radiation dose of 60 Gy. IMRT: Intensity modulated radiation therapy; PET/CT: Positron emission tomography/computed tomography.

the surgical wound is fully healed. Unfortunately, some patients with high-risk features may have recurrences even before starting PORT. Because of the anatomical distortion and fibrotic changes after surgery, and flap reconstruction, these recurrences are difficult to detect by physical examination and CT imaging. $^{18}$FDG-PET is an ideal imaging modality in this setting. Shintani *et al*[39] examined the utility of early post-operative pre-radiation PET/CT in HNCs. Among a cohort of 91 HNC patients, post-operative pre-radiation PET/CT performed at a median time of 28 d after surgery led to the discovery of 27 patients with suspicious findings on PET/CT. Of these, 24 patients (29% of the total cohort) underwent biopsy of these sites, with 11 biopsies positive for cancer. Treatment was changed in 14 patients (15.4%) with the addition of post-operative PET/CT: 4 underwent palliative care only, 6 had treatment to an extended volume, 1 received treatment to a higher dose, 2 underwent additional surgery and 2 received concurrent chemotherapy. Liao *et al*[40] also reported 29 patients who had a $^{18}$FDG-PET scan obtained before PORT. They found 7 patients with positive PET studies, 3 with distant metastases and 4 with local regional recurrences. For those who had locoregional disease detected by $^{18}$FDG-PET, the radiation volumes and radiation dose have to be changed, with higher doses delivered to the recurrent tumor. Thus, for patients with high-risk features or for those who have a prolonged interval from surgery to radiation, a post-surgery and pre-radiation $^{18}$FDG-PET will be valuable in treatment decision and radiation treatment planning.

Figure 8 illustrates a patient with initial stage T4AN2B right buccal mucosal cancer. He had surgery and radial forearm flap reconstruction. Due to the patient's non-compliance, he did not have radiation treatment planning until 50 d after surgery. A PET/CT was obtained at simulation that revealed tumor recurrence in the right masticator space and right infratemporal fossa region (Figure 8A and B). The recurrent tumor was not resectable and thus this was treated to 70 Gy rather than a traditional post-operative dose of 60 Gy. Figure 8C and D represents the IMRT plan for this patient.

Both pre-operative and post-radiation PET/CT may also assist in predicting the likelihood of disease-free survival and locoregional recurrence after PORT. Kim *et al*[41] correlated multiple PET/CT derived imaging factors with areas of high likelihood of recurrence. Examining 100 patients with both pre-operative and post-operative post-radiation PET/CT, the authors found that a metabolic tumor volume defined as a pre-operative autosegmentation of SUV > 2.5 of more than 41 cc predicted for poorer disease-free survival. Additionally, post-radiation treatment $SUV_{max}$ predicted for areas of locoregional recurrence. The authors suggested a post-treatment cutoff SUV value of 5.38 yielding a 93.7% NPV and a 66.7% positive predictive value. This may be used to select patients after postoperative radiation for further treatment interventions.

## FUTURE DIRECTIONS

In addition to the routinely clinically available $^{18}$FDG substrate, many newer radioisotopes and radiotracers are being developed to image further functional characteristics of tumors including hypoxia, tumor proliferation, amino acid metabolism and presence of EGFR on tumor cells[42]. Hypoxia is commonly noted in head and neck tumors including in the primary site and metastatic lymph nodes. This is commonly seen in HPV-positive cancers; tumors which often present with small primaries and large necrotic and hypoxic neck nodes. Identification of these hypoxic areas may allow for radiation dose escalation to hypoxic sub-regions of tumors. Hypoxia poses a major radiobiologic disadvantage and confers radioresistance to the tumor. Hypoxic cells are not killed in response to radiation therapy and may be responsible for treatment failure, either locally or as distant metastasis. A commonly used dose-prescription and dose-delivery technique is the "simultaneous integrated boost" method in which doses of 70 Gy are delivered to areas of gross disease while areas of intermediate-risk and low-risk of involvement by disease simultaneously receive 59.4 Gy to 63 Gy

and 56 Gy, respectively. Using the same technique it may be possible to further escalate the dose to the radio-resistant hypoxic regions in the same number of fractions while still meeting the dose constraints for surrounding normal tissue. Examples of radiopharmaceuticals being used to image the hypoxic portion of the tumor include $^{18}$F-fluoromisonidazole, copper-diacetyl-bis (N4-methylthiosamicarbazone) (Cu-ATSM) and $^{18}$F-fluoroazomycin arabinoside. The use of these agents has been described in literature[43,44]. Another interesting possibility is the use of 3'-deoxy-3'-[$^{18}$F]-fluorothymidine, a PET tracer to noninvasively image tumor cell proliferation, and deliver higher doses to areas of the tumor showing higher degree of tumor growth[45,46].

In addition to these newer substrates, there has also been an evolution in the imaging modalities with the development of simultaneous PET/MR imagers. These offer the advantages of high-quality soft tissue imaging from MR with whole-body and functional imaging from the PET component[47-49]. The use of PET/MR in HNC patients has been recently described[50,51].

Finally, improved acquisition technologies including time-of-flight PET (TOF-PET) and four-dimensional PET (4D-PET) are emerging. TOF-PET improves the signal-to-noise ratio in acquisition as well as reduces scanning time leading to improved image resolution[52]. This may further improve the benefit of PET in target delineation of HNCs by reducing PET-GTVs. 4D-PET has primarily found clinical utility in lung cancers[53], an entity in which tumor motion is more prominent than in HNCs. Though small relative to lung motion, organ motion does exist in the head and neck and an improvement in resolution and target delineation in HNCs by reducing artifacts may be expected with 4D-PET.

## CONCLUSION

The widespread availability of PET imagers and clinical experience has increased considerably in the recent years. Although methodologies of how to use PET information with either $^{18}$FDG or new substrates in radiation therapy planning for HNCs are still under development, PET scans have changed our daily practice in management of these patients. Integrating tumor biology obtained from these images with advanced delivery techniques using IMRT and image-guided radiation therapy has the potential to significantly impact outcomes in HNCs.

## REFERENCES


1 **Parkin DM**, Bray F, Ferlay J, Pisani P. Global cancer statistics, 2002. *CA Cancer J Clin* 2002; **55**: 74-108 [PMID: 15761078 DOI: 10.3322/canjclin.55.2.74]

2 **Ciernik IF**, Dizendorf E, Baumert BG, Reiner B, Burger C, Davis JB, Lütolf UM, Steinert HC, Von Schulthess GK. Radiation treatment planning with an integrated positron emission and computer tomography (PET/CT): a feasibility study. *Int J Radiat Oncol Biol Phys* 2003; **57**: 853-863 [PMID: 14529793 DOI: 10.1016/S0360-3016(03)00346-8]

3 **Heron DE**, Andrade RS, Flickinger J, Johnson J, Agarwala SS, Wu A, Kalnicki S, Avril N. Hybrid PET-CT simulation for radiation treatment planning in head-and-neck cancers: a brief technical report. *Int J Radiat Oncol Biol Phys* 2004; **60**: 1419-1424 [PMID: 15590173 DOI: 10.1016/j.ijrobp.2004.05.037]

4 **Guido A**, Fuccio L, Rombi B, Castellucci P, Cecconi A, Bunkheila F, Fuccio C, Spezi E, Angelini AL, Barbieri E. Combined 18F-FDG-PET/CT imaging in radiotherapy target delineation for head-and-neck cancer. *Int J Radiat Oncol Biol Phys* 2009; **73**: 759-763 [PMID: 18834671 DOI: 10.1016/j.ijrobp.2008.04.059]

5 **Paulino AC**, Koshy M, Howell R, Schuster D, Davis LW. Comparison of CT- and FDG-PET-defined gross tumor volume in intensity-modulated radiotherapy for head-and-neck cancer. *Int J Radiat Oncol Biol Phys* 2005; **61**: 1385-1392 [PMID: 15817341 DOI: 10.1016/j.ijrobp.2004.08.037]

6 **Breen SL**, Publicover J, De Silva S, Pond G, Brock K, O'Sullivan B, Cummings B, Dawson L, Keller A, Kim J, Ringash J, Yu E, Hendler A, Waldron J. Intraobserver and interobserver variability in GTV delineation on FDG-PET-CT images of head and neck cancers. *Int J Radiat Oncol Biol Phys* 2007; **68**: 763-770 [PMID: 17379435 DOI: 10.1016/j.ijrobp.2006.12.039]

7 **Anderson CM**, Sun W, Buatti JM, Maley JE, Policeni B, Mott SL, Bayouth JE. Interobserver and intermodality variability in GTV delineation on simulation CT, FDG-PET, and MR Images of Head and Neck Cancer. *Jacobs J Radiat Oncol* 2014; **1**: 006 [PMID: 25568889]

8 **Schinagl DA**, Vogel WV, Hoffmann AL, van Dalen JA, Oyen WJ, Kaanders JH. Comparison of five segmentation tools for 18F-fluoro-deoxy-glucose-positron emission tomography-based target volume definition in head and neck cancer. *Int J Radiat Oncol Biol Phys* 2007; **69**: 1282-1289 [PMID: 17967318 DOI: 10.1016/j.ijrobp.2007.07.2333]

9 **Schinagl DA**, Hoffmann AL, Vogel WV, van Dalen JA, Verstappen SM, Oyen WJ, Kaanders JH. Can FDG-PET assist in radiotherapy target volume definition of metastatic lymph nodes in head-and-neck cancer? *Radiother Oncol* 2009; **91**: 95-100 [PMID: 19285354 DOI: 10.1016/j.radonc.2009.02.007]

10 **Perez-Romasanta LA**, Bellon-Guardia M, Torres-Donaire J, Lozano-Martin E, Sanz-Martin M, Velasco-Jimenez J. Tumor volume delineation in head and neck cancer with 18-fluor-fluoro-deoxiglucose positron emission tomography: adaptive thresholding method applied to primary tumors and metastatic lymph nodes. *Clin Transl Oncol* 2013; **15**: 283-293 [PMID: 22865325 DOI: 10.1007/s12094-012-0914-z]

11 **Daisne JF**, Sibomana M, Bol A, Cosnard G, Lonneux M, Grégoire V. Evaluation of a multimodality image (CT, MRI and PET) coregistration procedure on phantom and head and neck cancer patients: accuracy, reproducibility and consistency. *Radiother Oncol* 2003; **69**: 237-245 [PMID: 14644482 DOI: 10.1016/j.radonc.2003.10.009]

12 **Schinagl DA**, Span PN, van den Hoogen FJ, Merkx MA, Slootweg PJ, Oyen WJ, Kaanders JH. Pathology-based validation of FDG PET segmentation tools for volume assessment of lymph node metastases from head and neck cancer. *Eur J Nucl Med Mol Imaging* 2013; **40**: 1828-1835 [PMID: 23942906 DOI: 10.1007/s00259-013-2513-9]

13 **Som PM**. Detection of metastasis in cervical lymph nodes: CT and MR criteria and differential diagnosis. *AJR Am J Roentgenol* 1992; **158**: 961-969 [PMID: 1566697 DOI: 10.2214/ajr.158.5.1566697]

14 **Adams S**, Baum RP, Stuckensen T, Bitter K, Hör G. Prospective comparison of 18F-FDG PET with conventional imaging modalities (CT, MRI, US) in lymph node staging of head and neck cancer. *Eur J Nucl Med* 1998; **25**: 1255-1260 [PMID: 9724374 DOI: 10.1007/s002590050293]

15 **Koshy M**, Paulino AC, Howell R, Schuster D, Halkar R, Davis LW. F-18 FDG PET-CT fusion in radiotherapy treatment planning for head and neck cancer. *Head Neck* 2005; **27**: 494-502 [PMID: 15772951 DOI: 10.1002/hed.20179]

16 **Schwartz DL**, Ford EC, Rajendran J, Yueh B, Coltrera MD, Virgin J, Anzai Y, Haynor D, Lewellen B, Mattes D, Kinahan P, Meyer J,

Phillips M, Leblanc M, Krohn K, Eary J, Laramore GE. FDG-PET/CT-guided intensity modulated head and neck radiotherapy: a pilot investigation. *Head Neck* 2005; **27**: 478-487 [PMID: 15772953 DOI: 10.1002/hed.20177]

17 **Jereczek-Fossa BA**, Jassem J, Orecchia R. Cervical lymph node metastases of squamous cell carcinoma from an unknown primary. *Cancer Treat Rev* 2004; **30**: 153-164 [PMID: 15023433 DOI: 10.1016/j.ctrv.2003.10.001]

18 **Grau C**, Johansen LV, Jakobsen J, Geertsen P, Andersen E, Jensen BB. Cervical lymph node metastases from unknown primary tumours. Results from a national survey by the Danish Society for Head and Neck Oncology. *Radiother Oncol* 2000; **55**: 121-129 [PMID: 10799723 DOI: 10.1016/S0167-8140(00)00172-9]

19 **Lee DJ**, Rostock RA, Harris A, Kashima H, Johns M. Clinical evaluation of patients with metastatic squamous carcinoma of the neck with occult primary tumor. *South Med J* 1986; **79**: 979-983 [PMID: 3738594]

20 **Rusthoven KE**, Koshy M, Paulino AC. The role of fluorodeoxyglucose positron emission tomography in cervical lymph node metastases from an unknown primary tumor. *Cancer* 2004; **101**: 2641-2649 [PMID: 15517576 DOI: 10.1002/cncr.20687]

21 **Rudmik L**, Lau HY, Matthews TW, Bosch JD, Kloiber R, Molnar CP, Dort JC. Clinical utility of PET/CT in the evaluation of head and neck squamous cell carcinoma with an unknown primary: a prospective clinical trial. *Head Neck* 2011; **33**: 935-940 [PMID: 21674668 DOI: 10.1002/hed.21566]

22 **Li H**, Noel C, Chen H, Harold Li H, Low D, Moore K, Klahr P, Michalski J, Gay HA, Thorstad W, Mutic S. Clinical evaluation of a commercial orthopedic metal artifact reduction tool for CT simulations in radiation therapy. *Med Phys* 2012; **39**: 7507-7517 [PMID: 23231300 DOI: 10.1118/1.4762814]

23 **Kinahan PE**, Townsend DW, Beyer T, Sashin D. Attenuation correction for a combined 3D PET/CT scanner. *Med Phys* 1998; **25**: 2046-2053 [PMID: 9800714 DOI: 10.1118/1.598392]

24 **Kamel EM**, Burger C, Buck A, von Schulthess GK, Goerres GW. Impact of metallic dental implants on CT-based attenuation correction in a combined PET/CT scanner. *Eur Radiol* 2003; **13**: 724-728 [PMID: 12664109 DOI: 10.1007/s00330-002-1564-2]

25 **Goerres GW**, Schmid DT, Eyrich GK. Do hardware artefacts influence the performance of head and neck PET scans in patients with oral cavity squamous cell cancer? *Dentomaxillofac Radiol* 2003; **32**: 365-371 [PMID: 15070838 DOI: 10.1259/dmfr/77741718]

26 **Nahmias C**, Lemmens C, Faul D, Carlson E, Long M, Blodgett T, Nuyts J, Townsend D. Does reducing CT artifacts from dental implants influence the PET interpretation in PET/CT studies of oral cancer and head and neck cancer? *J Nucl Med* 2008; **49**: 1047-1052 [PMID: 18552154 DOI: 10.2967/jnumed.107.049858]

27 **Hong HR**, Jin S, Koo HJ, Roh JL, Kim JS, Cho KJ, Choi SH, Nam SY, Kim SY. Clinical values of (18) F-FDG PET/CT in oral cavity cancer with dental artifacts on CT or MRI. *J Surg Oncol* 2014; **110**: 696-701 [PMID: 24995957 DOI: 10.1002/jso.23691]

28 **Baek CH**, Chung MK, Son YI, Choi JY, Kim HJ, Yim YJ, Ko YH, Choi J, Cho JK, Jeong HS. Tumor volume assessment by 18F-FDG PET/CT in patients with oral cavity cancer with dental artifacts on CT or MR images. *J Nucl Med* 2008; **49**: 1422-1428 [PMID: 18703597 DOI: 10.2967/jnumed.108.051649]

29 **Buchbender C**, Hartung-Knemeyer V, Forsting M, Antoch G, Heusner TA. Positron emission tomography (PET) attenuation correction artefacts in PET/CT and PET/MRI. *Br J Radiol* 2013; **86**: 20120570 [PMID: 23580397 DOI: 10.1259/bjr.20120570]

30 **Delso G**, Wollenweber S, Lonn A, Wiesinger F, Veit-Haibach P. MR-driven metal artifact reduction in PET/CT. *Phys Med Biol* 2013; **58**: 2267-2280 [PMID: 23478566 DOI: 10.1088/0031-9155/58/7/2267]

31 **Burger IA**, Wurnig MC, Becker AS, Kenkel D, Delso G, Veit-Haibach P, Boss A. Hybrid PET/MR imaging: an algorithm to reduce metal artifacts from dental implants in Dixon-based attenuation map generation using a multiacquisition variable-resonance image combination sequence. *J Nucl Med* 2015; **56**: 93-97 [PMID: 25500830 DOI: 10.2967/jnumed.114.145862]

32 **Peters LJ**, Goepfert H, Ang KK, Byers RM, Maor MH, Guillamondegui O, Morrison WH, Weber RS, Garden AS, Frankenthaler RA. Evaluation of the dose for postoperative radiation therapy of head and neck cancer: first report of a prospective randomized trial. *Int J Radiat Oncol Biol Phys* 1993; **26**: 3-11 [PMID: 8482629 DOI: 10.1016/0360-3016(93)90167-T]

33 **Ang KK**, Trotti A, Brown BW, Garden AS, Foote RL, Morrison WH, Geara FB, Klotch DW, Goepfert H, Peters LJ. Randomized trial addressing risk features and time factors of surgery plus radiotherapy in advanced head-and-neck cancer. *Int J Radiat Oncol Biol Phys* 2001; **51**: 571-578 [PMID: 11597795 DOI: 10.1016/S0360-3016(01)01690-X]

34 **Bernier J**, Domenge C, Ozsahin M, Matuszewska K, Lefèbvre JL, Greiner RH, Giralt J, Maingon P, Rolland F, Bolla M, Cognetti F, Bourhis J, Kirkpatrick A, van Glabbeke M. Postoperative irradiation with or without concomitant chemotherapy for locally advanced head and neck cancer. *N Engl J Med* 2004; **350**: 1945-1952 [PMID: 15128894 DOI: 10.1056/NEJMoa032641]

35 **Cooper JS**, Pajak TF, Forastiere AA, Jacobs J, Campbell BH, Saxman SB, Kish JA, Kim HE, Cmelak AJ, Rotman M, Machtay M, Ensley JF, Chao KS, Schultz CJ, Lee N, Fu KK. Postoperative concurrent radiotherapy and chemotherapy for high-risk squamous-cell carcinoma of the head and neck. *N Engl J Med* 2004; **350**: 1937-1944 [PMID: 15128893 DOI: 10.1056/NEJMoa032646]

36 **Bernier J**, Cooper JS, Pajak TF, van Glabbeke M, Bourhis J, Forastiere A, Ozsahin EM, Jacobs JR, Jassem J, Ang KK, Lefèbvre JL. Defining risk levels in locally advanced head and neck cancers: a comparative analysis of concurrent postoperative radiation plus chemotherapy trials of the EORTC (#22931) and RTOG (# 9501). *Head Neck* 2005; **27**: 843-850 [PMID: 16161069 DOI: 10.1002/hed.20279]

37 **Grégoire V**, Eisbruch A, Hamoir M, Levendag P. Proposal for the delineation of the nodal CTV in the node-positive and the post-operative neck. *Radiother Oncol* 2006; **79**: 15-20 [PMID: 16616387 DOI: 10.1016/j.radonc.2006.03.009]

38 **Kovalchuk N**, Jalisi S, Subramaniam RM, Truong MT. Deformable registration of preoperative PET/CT with postoperative radiation therapy planning CT in head and neck cancer. *Radiographics* 2012; **32**: 1329-1341 [PMID: 22977021 DOI: 10.1148/rg.325125008]

39 **Shintani SA**, Foote RL, Lowe VJ, Brown PD, Garces YI, Kasperbauer JL. Utility of PET/CT imaging performed early after surgical resection in the adjuvant treatment planning for head and neck cancer. *Int J Radiat Oncol Biol Phys* 2008; **70**: 322-329 [PMID: 17889447 DOI: 10.1016/j.ijrobp.2007.06.038]

40 **Liao CT**, Fan KH, Lin CY, Wang HM, Huang SF, Chen IH, Kang CJ, Ng SH, Hsueh C, Lee LY, Lin CH, Yen TC. Impact of a second FDG PET scan before adjuvant therapy for the early detection of residual/relapsing tumours in high-risk patients with oral cavity cancer and pathological extracapsular spread. *Eur J Nucl Med Mol Imaging* 2012; **39**: 944-955 [PMID: 22434050 DOI: 10.1007/s00259-012-2103-2]

41 **Kim G**, Kim YS, Han EJ, Yoo IeR, Song JH, Lee SN, Lee JH, Choi BO, Jang HS, Yoon SC. FDG-PET/CT as prognostic factor and surveillance tool for postoperative radiation recurrence in locally advanced head and neck cancer. *Radiat Oncol J* 2011; **29**: 243-251 [PMID: 22984677 DOI: 10.3857/roj.2011.29.4.243]

42 **Wang TJC**, Menda Y, Cheng SK, Wu CC, Lee NY. New Tracers PET in head and neck squamous cell carcinoma. *PET Clin* 2012; **7**: 431-441 [DOI: 10.1016/j.cpet.2012.06.009]

43 **Chao KS**, Bosch WR, Mutic S, Lewis JS, Dehdashti F, Mintun MA, Dempsey JF, Perez CA, Purdy JA, Welch MJ. A novel approach to overcome hypoxic tumor resistance: Cu-ATSM-guided intensity-modulated radiation therapy. *Int J Radiat Oncol Biol Phys* 2001; **49**: 1171-1182 [PMID: 11240261 DOI: 10.1016/S0360-3016(00)01433-4]

44 **Servagi-Vernat S**, Differding S, Hanin FX, Labar D, Bol A, Lee JA, Grégoire V. A prospective clinical study of $^{18}$F-FAZA PET-CT hypoxia imaging in head and neck squamous cell carcinoma before and during radiation therapy. *Eur J Nucl Med Mol Imaging* 2014; **41**: 1544-1552 [PMID: 24570097 DOI: 10.1007/s00259-014-

2730-x]
45 **Arens AI**, Troost EG, Hoeben BA, Grootjans W, Lee JA, Grégoire V, Hatt M, Visvikis D, Bussink J, Oyen WJ, Kaanders JH, Visser EP. Semiautomatic methods for segmentation of the proliferative tumour volume on sequential FLT PET/CT images in head and neck carcinomas and their relation to clinical outcome. *Eur J Nucl Med Mol Imaging* 2014; **41**: 915-924 [PMID: 24346414 DOI: 10.1007/s00259-013-2651-0]
46 **Troost EG**, Bussink J, Hoffmann AL, Boerman OC, Oyen WJ, Kaanders JH. 18F-FLT PET/CT for early response monitoring and dose escalation in oropharyngeal tumors. *J Nucl Med* 2010; **51**: 866-874 [PMID: 20484426 DOI: 10.2967/jnumed.109.069310]
47 **Berker Y**, Franke J, Salomon A, Palmowski M, Donker HC, Temur Y, Mottaghy FM, Kuhl C, Izquierdo-Garcia D, Fayad ZA, Kiessling F, Schulz V. MRI-based attenuation correction for hybrid PET/MRI systems: a 4-class tissue segmentation technique using a combined ultrashort-echo-time/Dixon MRI sequence. *J Nucl Med* 2012; **53**: 796-804 [PMID: 22505568 DOI: 10.2967/jnumed.111.092577]
48 **Drzezga A**, Souvatzoglou M, Eiber M, Beer AJ, Fürst S, Martinez-Möller A, Nekolla SG, Ziegler S, Ganter C, Rummeny EJ, Schwaiger M. First clinical experience with integrated whole-body PET/MR: comparison to PET/CT in patients with oncologic diagnoses. *J Nucl Med* 2012; **53**: 845-855 [PMID: 22534830 DOI: 10.2967/jnumed.111.098608]
49 **Keereman V**, Fierens Y, Broux T, De Deene Y, Lonneux M, Vandenberghe S. MRI-based attenuation correction for PET/MRI using ultrashort echo time sequences. *J Nucl Med* 2010; **51**: 812-818 [PMID: 20439508 DOI: 10.2967/jnumed.109.065425]
50 **Covello M**, Cavaliere C, Aiello M, Cianelli MS, Mesolella M, Iorio B, Rossi A, Nicolai E. Simultaneous PET/MR head-neck cancer imaging: Preliminary clinical experience and multiparametric evaluation. *Eur J Radiol* 2015; **84**: 1269-1276 [PMID: 25958189 DOI: 10.1016/j.ejrad.2015.04.010]
51 **Queiroz MA**, Huellner MW. PET/MR in cancers of the head and neck. *Semin Nucl Med* 2015; **45**: 248-265 [PMID: 25841279 DOI: 10.1053/j.semnuclmed.2014.12.005]
52 **Surti S**. Update on time-of-flight PET imaging. *J Nucl Med* 2015; **56**: 98-105 [PMID: 25525181 DOI: 10.2967/jnumed.114.145029]
53 **Chirindel A**, Adebahr S, Schuster D, Schimek-Jasch T, Schanne DH, Nemer U, Mix M, Meyer P, Grosu AL, Brunner T, Nestle U. Impact of 4D-(18)FDG-PET/CT imaging on target volume delineation in SBRT patients with central versus peripheral lung tumors. Multi-reader comparative study. *Radiother Oncol* 2015; **115**: 335-341 [PMID: 26116339 DOI: 10.1016/j.radonc.2015.05.019]

**P- Reviewer**: Chang Z, Gao BL
**S- Editor**: Tian YL **L- Editor**: A **E- Editor**: Jiao XK

World Journal of Radiology

Submit a Manuscript: http://www.wjgnet.com/esps/
Help Desk: http://www.wjgnet.com/esps/helpdesk.aspx
DOI: 10.4329/wjr.v7.i11.394

*World J Radiol* 2015 November 28; 7(11): 394-404
ISSN 1949-8470 (online)


ORIGINAL ARTICLE

Case Control Study

# Magnetic resonance imaging in assessment of stress urinary incontinence in women: Parameters differentiating urethral hypermobility and intrinsic sphincter deficiency

Katarzyna Jadwiga Macura, Richard Eugene Thompson, David Alan Bluemke, Rene Genadry

Katarzyna Jadwiga Macura, The Russell H. Morgan Department of Radiology and Radiological Science, Johns Hopkins University, Baltimore, MD 21287, United States

Richard Eugene Thompson, Johns Hopkins Biostatistics Center, Baltimore, MD 21205, United States

David Alan Bluemke, National Institutes of Health Clinical Center, Bethesda, MD 20892, United States

Rene Genadry, University of Iowa Hospitals and Clinics, Iowa City, IA 52242, United States

Author contributions: Macura KJ, Bluemke DA and Genadry R contributed to the design of the study, acquisition of data, and interpretation of data; Thompson RE performed statistical analysis of data; Macura KJ and Genadry R drafted the article; Macura KJ, Thompson RE, Bluemke DA and Genadry R made critical review of the content of the manuscript and approved the final version of the article.

Supported by The Radiological Society of North America and the Society of Computed Body Tomography and Magnetic Resonance.

Institutional review board statement: The study was approved by the Johns Hopkins University Institutional Review Board.

Informed consent statement: The study was compliant with the Health Insurance Portability and Accountability Act. Study-specific written consent was obtained from all subjects.

Conflict-of-interest statement: The authors declare no conflicts of interest regarding this manuscript.

Data sharing statement: Participants did not give informed consent for data sharing and no additional data are available.



Correspondence to: Katarzyna Jadwiga Macura, MD, PhD, Professor of Radiology, The Russell H. Morgan Department of Radiology and Radiological Science, Johns Hopkins University, 601 N. Caroline Street, JHOC 3140C, Baltimore, MD 21287, United States. kmacura@jhmi.edu
Telephone: +1-410-9555391
Fax: +1-410-9557699

Received: June 30, 2015
Peer-review started: July 5, 2015
First decision: July 31, 2015
Revised: August 22, 2015
Accepted: September 29, 2015
Article in press: September 30, 2015
Published online: November 28, 2015

## Abstract

**AIM:** To define the magnetic resonance imaging (MRI) parameters differentiating urethral hypermobility (UH) and intrinsic sphincter deficiency (ISD) in women with stress urinary incontinence (SUI).

**METHODS:** The static and dynamic MR images of 21 patients with SUI were correlated to urodynamic (UD) findings and compared to those of 10 continent controls. For the assessment of the urethra and integrity of the urethral support structures, we applied the high-resolution endocavitary MRI, such as intraurethral MRI, endovaginal or endorectal MRI. For the functional imaging of the urethral support, we performed dynamic MRI with the pelvic phased array coil. We assessed the following MRI parameters in both the patient and the

volunteer groups: (1) urethral angle; (2) bladder neck descent; (3) status of the periurethral ligaments, (4) vaginal shape; (5) urethral sphincter integrity, length and muscle thickness at mid urethra; (6) bladder neck funneling; (7) status of the puborectalis muscle; (8) pubo-vaginal distance. UDs parameters were assessed in the patient study group as follows: (1) urethral mobility angle on Q-tip test; (2) Valsalva leak point pressure (VLPP) measured at 250 cc bladder volume; and (3) maximum urethral closure pressure (MUCP). The UH type of SUI was defined with the Q-tip test angle over 30 degrees, and VLPP pressure over 60 cm $H_2O$. The ISD incontinence was defined with MUCP pressure below 20 cm $H_2O$, and VLPP pressure less or equal to 60 cm $H_2O$. We considered the associations between the MRI and clinical data and UDs using a variety of statistical tools to include linear regression, multivariate logistic regression and receiver operating characteristic (ROC) analysis. All statistical analyses were performed using STATA version 9.0 (StataCorp LP, College Station, TX).

**RESULTS:** In the incontinent group, 52% have history of vaginal delivery trauma as compared to none in control group ($P < 0.001$). There was no difference between the continent volunteers and incontinent patients in body habitus as assessed by the body mass index. Pubovaginal distance and periurethral ligament disruption are significantly associated with incontinence; periurethral ligament symmetricity reduces the odds of incontinence by 87%. Bladder neck funneling and length of the suprapubic urethral sphincter are significantly associated with the type of incontinence on UDs; funneling reduced the odds of pure UH by almost 95%; increasing suprapubic urethral sphincter length at rest is highly associated with UH. Both MRI variables result in a predictive model for UDs diagnosis (area under the ROC = 0.944).

**CONCLUSION:** MRI may play an important role in assessing the contribution of hypermobility and sphincteric dysfunction to the SUI in women when considering treatment options.

**Key words:** Magnetic resonance imaging; Stress urinary incontinence; Women; Urethra hypermobility; Intrincic sphincter deficiency; Urodynamics; Dynamic magnetic resonance imaging



**Core tip:** Magnetic resonance imaging (MRI) allows visualization of the female urethra and periurethral tissues relevant to stress urinary incontinence (SUI). The role of MRI in the specific diagnosis of SUI caused by urethral hypermobility (UH) and/or intrinsic sphincter deficiency (ISD) has not been documented. The purpose of this pilot study was to define the MRI parameters differentiating UH and ISD types of incontinence, and assess their ability to predict the type of SUI when urodynamic (UD) results are used as a reference standard. Bladder neck funneling and length of the suprapubic urethral sphincter on MRI were significantly associated with the type of incontinence on UDs.

Macura KJ, Thompson RE, Bluemke DA, Genadry R. Magnetic resonance imaging in assessment of stress urinary incontinence in women: Parameters differentiating urethral hypermobility and intrinsic sphincter deficiency. *World J Radiol* 2015; 7(11): 394-404 Available from: URL: http://www.wjgnet.com/1949-8470/full/v7/i11/394.htm DOI: http://dx.doi.org/10.4329/wjr.v7.i11.394

## INTRODUCTION

Stress urinary incontinence (SUI) is the observation of involuntary urinary loss from the urethra synchronous with exertion, sneezing, or coughing. Urodynamic stress incontinence is noted during urodynamic testing and is defined as the involuntary leakage of urine during increases in abdominal pressure in the absence of a detrusor contraction. SUI is one of the most common conditions among women with a significant impact on the quality of life due to psychosocial and hygienic problems[1]. Two main etiologic factors have been implicated in the urethral dysfunction leading to SUI, urethral hypermobility (UH) and intrinsic sphincter deficiency (ISD)[2]. In UH, it is the weakness of pelvic floor support that results in a rotational descent of the vesical neck and urethra during increases in abdominal pressure with subsequent leakage. In ISD, there is malfunction of the urethral sphincter which leads to low urethral closure pressures[3].

The type of urinary incontinence determines choice of surgical treatment, to prevent UH by repositioning the urethra into the pelvis to equalize pressure transmission between the bladder and urethra, and for women with low urethral resistance in ISD to increase the urethral closure pressures. Studies investigating the effects of UH and ISD on the outcome of the commonly performed procedures, such as transobturator tape (TOT) used to treat UH reported that the lack of UH as a contributing factor to SUI may be a risk factor for TOT failure[4]. Also, Sand *et al*[5] studied women who failed retropubic suspension and found a higher failure rate in those with ISD. It has been shown that SUI caused by ISD is the most challenging to treat; with failure rates as high as 54%[6]. These failures were attributed to the correction of UH without concomitant increase of urethral closure pressures.

Traditionally, the diagnosis of SUI is made based on history, clinical exam and urodynamics (UDs) or videourodynamics. Urethral pressure profilometry [which allows to measure maximum urethral closure pressure (MUCP)] may be combined with videourodynamics. This indirect method has limitations, as only the physiologic effect of sphincteric dysfunction can be assessed,

without the evaluation of any morphological defects leading to SUI.

With its excellent soft tissue contrast and multiplanar acquisition, magnetic resonance imaging (MRI) allows visualization of the female urethra and periurethral tissues relevant to SUI[7,8]. MRI findings related to SUI caused by UH and ISD in women have been described[9]. Previous studies of MRI in female patients with SUI were focused on the assessment of lesions of the urethral support mechanism[10], defects of the levator ani muscle[11,12], and paravaginal fascia[13], as well as on the kinematics of pelvic floor muscles function[14].

To date, however, the role of MRI in the specific diagnosis of SUI caused by UH and/or ISD has not been documented. Therefore, the purpose of this pilot study was to define the MRI parameters differentiating UH and ISD types of incontinence, and assess their ability to predict the type of SUI with UDs as a reference standard.

## MATERIALS AND METHODS

### *Patient accrual and informed consent*

The study was approved by the Institutional Review Board. The study was compliant with the Health Insurance Portability and Accountability Act. Study-specific written consent was obtained from all subjects. Patients were recruited from the Urogynecology clinic for this single-institution study, in which prospectively collected data from consecutive women who met the enrollment criteria and participated in the study were analyzed in a retrospective fashion. A target accrual of 20 patients with SUI and 10 volunteers was established for this pilot study. A total of 31 women were recruited. The inclusion criteria were as follows: (1) SUI documented on UDs (for patients with SUI) or no clinical symptoms of SUI (for volunteers); (2) study-specific informed consent signed prior to study entry; (3) no contraindications to MRI. Subject exclusion criteria were as follows: (1) unable to give valid informed consent; (2) unable to undergo MR, *e.g.*, patients with contra-indications to MR imaging; (3) latex allergy; (4) extraurethral incontinence and bladder abnormalities causing incontinence; (5) greater than grade Ⅱ prolapse on clinical exam; (6) pregnancy and (7) metallic implant(s) that might compromise quality of MRI.

### *MR imaging technique*

MRI was performed on 1.5 T magnet (Signa Excite, GE Medical Systems, Waukesha, WI). For the assessment of the urethra and integrity of the urethral support structures, we applied the high-resolution endocavitary MRI, such as intraurethral MRI, endovaginal or endorectal MRI. For the functional imaging of the urethral support, we performed dynamic MRI with the pelvic phased array coil.

**Intraurethral MRI:** The 14F endourethral coil (SurgiVision, Inc., Gaithersburg, MD) was inserted under sterile conditions into the urethra. Both patient and volunteer groups underwent intraurethral MRI. All patients tolerated the procedure well and there were no complications from the coil placement. Patients were not pre-medicated with antibiotics. The imaging protocol included ultra-high resolution T2-weighted sequences in the axial and coronal planes (TR/TE 4000-6000 ms/90-120 ms, slice/spacing 2.5-3 mm/0-1 mm, FOV 6-10 cm centered on the urethra, matrix 256 × 256 ZIP interpolated to 512, NEX 6-8).

**Endovaginal or endorectal MRI:** The MRInnervu coil (Medrad, Indianola, PA) was placed in the vagina or rectum, depending on the patient's or volunteer's preference. The imaging protocol included T2-weighted fast spin echo (FSE) acquisition in three-plane with the field of view 10-14 cm and anatomical coverage between the symphysis pubis and coccyx. Imaging parameters were as follows: TR/TE 4000-6000 ms/90-120 ms, slice/space 3 mm/0-1 mm, matrix 256 × 192, NEX 3-4. The axial images were acquired in the oblique plane, perpendicular to the urethral axis. The frequency direction was AP to avoid endorectal/vaginal coil motion artifact over the urethra.

**Pelvic MRI:** Larger field of view imaging (20-30 cm) with the pelvic phased array coil was performed with the following parameters for the T2-weighted FSE images in axial and sagittal planes: TR/TE 4000-6000 ms/90-120 ms, slice/space 4-6 mm/0-1 mm, matrix 512 × 512, NEX 1-2. The dynamic pelvic floor imaging was performed in sagittal plane during rest and maximal strain with single shot fast spin echo (SSFSE) sequence TR/TE 15000/70 ms, slice/space 6 mm/2 mm, matrix 512 × 256, NEX 0.5; each image was acquired in 2 s, 10 images per sequence. At least two dynamic sequences were performed at maximal strain. Patients were asked to empty their bladder prior to the MRI, at the time of the dynamic evaluation they had their bladder at least half-full.

### *MRI interpretation*

We assessed the following parameters in both the patient and the volunteer groups: (1) urethral angle; (2) bladder neck descent; (3) status of the periurethral ligaments; (4) vaginal shape; (5) urethral sphincter integrity, length and muscle thickness at mid urethra; (6) bladder neck funneling; (7) status of the puborectalis muscle (PRM); and (8) pubo-vaginal distance (PVD).

The urethral angle was defined as an angle between the patient body axis and the axis of the urethra, assessed at rest and during maximal strain. UH was diagnosed if the angle changed over 30 degrees between the rest and strain (as per definition of hypermobility)[11]. The bladder neck descent was measured as a distance (cm) between its position at rest and strain in reference to the pubococcygeal line (PCL, a line drawn from the inferior margin of the pubic bone to the last coccygeal joint).

We assessed the integrity of the periurethral ligament that was seen in all patients. The periurethral ligament is the hypointense linear structure extending from PRM attachment on both sides of the pelvis and running in front of the urethra. The ligament status (intact/symmetric *vs* disrupted), as well as the site of disruption was evaluated. The ligament was judged as intact when the attachments were maintained and the ligament had a taut appearance and normal course. The ligament was deemed disrupted when there was a wavy/laxed appearance to the ligament, discontinuity of the ligament was present, or the attachment at PRM was lost.

The normal vaginal shape, assessed as an H-shaped contour on axial images, was deemed as a sign of the normal vaginolevator attachments. The loss of the H-shape vaginal morphology on axial images was interpreted as the presence of abnormal vaginolevator attachments (paravaginal defect) reflecting the loss of vaginal support. Laterality of the paravaginal defect was assessed. The PVD was measured as a distance between the posterior margin of the pubis and the anterior margin of the vagina at the mid urethra level (mid urethra defined at 50% of the sphincter length from the internal meatus).

The urethral sphincter length was measured at rest on the coronal and sagittal views, and a mean from both measurements was obtained as the total sphincter length. In addition to the total sphincter length, we assessed the functional length of the sphincter above the pelvic floor level (above the inferior pubic margin) and expressed it as a percentage of the total sphincter length. We evaluated the urethral sphincter muscle status for focal defects or signal changes within the sphincter. We measured the sphincter muscle thickness at the mid urethra level, for the anterior, lateral, and posterior urethral walls, separately for the striated and smooth muscle layers and for the total wall thickness.

We assessed the presence or absence of the bladder neck funneling, defined as an opening of the internal meatus of the urethral sphincter at rest or during strain.

The status of the PRM was evaluated at the mid urethra level. The muscle thickness (measured at mid length of the muscle), its length, and an angle between the PRM and an obturator internus muscle were assessed.

The anonymized MRI scans were reviewed on a PACS workstation (eFilm Workstation, Merge Healthcare, Milwaukee, WI) by two investigators (KJM with 10 years of experience in GU MRI and RG with 20 years of experience in urogynecology) blinded to the subject's status as a patient with SUI *vs* continent volunteer. The MRI parameters, as above, were assessed by consensus as to the presence of the finding, symmetricity and/or severity. The review was performed at least 1 year post-imaging date, to avoid a memory bias as to the pelvic anatomy of the subjects. Data were entered into the Excel (Microsoft, Bellevue, WA) spreadsheet for subsequent transfer to the STATA 9.0 (StataCorp LP, College Station, TX).

### *Urodynamics exam*

The urodynamics exam was performed on a UD-2000 MMS (Medical Measurement System) using Millar Micro-tip 8F catheter transducers following a standard protocol: The patient empties her bladder and a post-void residual is measured. With the patient in the sitting position at 45°, and after the sensors have been zeroed to atmospheric pressure before insertion, a dual sensor catheter is inserted in the urethra with the proximal sensor in the bladder and the distal sensor positioned at the area of maximal urethral closure pressure (MUCP). A single sensor catheter is also inserted intravaginally to indirectly record intra-abdominal pressure. The detrusor pressure is monitored continually as an automatically subtracted pressure. An infusion of sterile water is instilled at a rate of 60 mL/mn. Volume at first desire, strong desire and urge to urinate are recorded in standard fashion. After 250 mL have been instilled in the bladder a Valsalva leak point pressure (VLPP) is obtained. It is defined as the pressure increase leading to leakage in the absence of detrusor contraction. The subtracted nature of the pressure eliminates the effect of different pressures obtained with different types of catheters. Usually, the patient is asked to bear down maximally to determine the presence of incontinence and then incrementally to determine the lowest pressure leading to incontinence. In the absence of leakage with maximal Valsalva generated pressure, the patient was asked to cough maximally and incrementally for the same purpose. For this study group, a VLPP was obtained. The Q-tip test is obtained in the following manner. With the patient lying on the chair leveled with the horizontal, a sterile cotton-tipped swab is lubricated and placed in the urethra to the level of the urethrovesical junction. With the patient at rest, the angle of the distal end of the swab is measured relative to the horizontal and recorded. The patient then is instructed to bear down to maximal Valsalva effort and the angle is measured again. The difference in the two angles is recorded as the Q-tip test angle.

Urodynamics parameters were assessed in the patient study group as follows: (1) urethral mobility angle on Q-tip test; (2) VLPP measured at 250 cc bladder volume; and (3) MUCP. The UH type of SUI was defined with the Q-tip test angle over 30 degrees, and VLPP pressure over 60 cm $H_2O$. The ISD incontinence was defined with MUCP pressure below 20 cm $H_2O$, and VLPP pressure less or equal to 60 cm $H_2O$. Out of 21 incontinent patients, 18 had a complete UDs exam, 3 had incomplete exam that did not include the MUCP measurement. The volunteer group did not undergo the UDs exam as volunteer women had no clinical symptoms of urinary incontinence and therefore were not subjected to the invasive UDs workup.

### *Statistical analysis*

As a primary analysis, we considered the statistical

associations between the MRI and clinical data with the binary outcome of incontinence (present/absent). Continuous variables were assessed using the two sample *t*-test with a two-sided alpha of 0.05. We used the $\chi^2$ test and, when appropriate, the Fisher's exact test, for categorical and dichotomous data. As a secondary analysis, we looked at only the subset of women with the diagnosis of SUI. These analyses included an assessment of the correlation between the UDs variables of MUCP and VLPP with the MRI data, as well as an investigation of the MRI variables that discriminated between women with a UDs diagnosis of SUI due to pure UH *vs* a diagnosis of SUI with an ISD component (pure ISD or mixed UH/ISD). In the former analyses, we used the Pearson's correlation coefficient along with scatter plots and linear regression analyses. In the latter case, multivariate logistic regression models were created on the binary outcome of SUI with pure UH *vs* SUI with an ISD component using MRI and other clinical variables that at least trended toward statistical significance (*e.g.*, *P* value < 0.1) in the univariate analyses. ROC analysis was then performed in order to assess the discriminative power of the MRI variables in the logistic regression models, and to obtain estimates of sensitivities, specificities, positive predictive values, and negative predictive values using the UDs diagnosis as the reference standard. All statistical analyses were performed using STATA version 9.0 (StataCorp LP, College Station, TX) by a biomedical statistician.

## RESULTS

Thirty one women recruited for this study were considered in the analysis, 21 with SUI and 10 volunteer controls. The characteristics of participants according to continent *vs* incontinent status are listed in Table 1.

When differences in clinical variables by incontinent status were considered, a history of obstetrical (OB) trauma was the only variable found to be statistically significant. Eleven of the 21 women with incontinence (52%) had a history of trauma during child birth (episiotomy, forceps delivery, perineal laceration) as compared to none of the control volunteer women (*P* < 0.001, Fisher's exact test). Incontinent women tended to be older with a mean (SD) age of 54.4 (11.8) years *vs* 45.1 (13.6) years for controls (*P* = 0.0610, *t*-test). There was no difference between the continent volunteers and incontinent patients in body habitus as assessed by the body mass index (BMI). Among the MRI variables, PVD and periurethral ligament disruption were found to be significantly associated with incontinence status (Table 1). Seven of the 10 control patients (70%) had intact, symmetric periurethral ligament, as opposed to only 4 of the 20 incontinent (20%) women (*P* = 0.015, Fisher's exact test) (Figures 1 and 2). When these variables were considered in a multivariable logistic regression model, we found that only periurethral ligament status was statistically associated with incontinence. Having intact periurethral ligament reduced the odds of incontinence by 87% as compared to those who had periurethral disruption [Adjusted odds ratio 95%CI: 0.13 (0.018, 0.961), *P* = 0.046].

Among the subset of incontinent patients, we found an inverse correlation between bladder neck descent and MUCP that trended towards statistical significance (Pearson's correlation = -0.537, *P* = 0.089). When we looked at VLPP, only total urethral sphincter length trended to significance, giving a Pearson's correlation coefficient of 0.478 (*P* = 0.072) (Figures 3 and 4).

When we looked at the relationship of UDs diagnosis in patients who had complete UDs (SUI due to pure UH in 9 patients *vs* SUI with ISD component in 9 patients) and the MRI data, both bladder neck funneling (absent *vs* present) (Figure 5) and the functional suprapubic urethra sphincter length were found to be significantly associated with UDs diagnosis. In the univariate logistic model, being positive for funneling reduced the odds of pure UH diagnosis by almost 95% as compared to no funneling [OR (95%CI) = 0.036 (0.003, 0.484), *P* = 0.012]. In contrast, increasing the suprapubic urethral sphincter length was highly associated with an UDs diagnosis of UH [OR (95%CI) = 12.95 (1.17, 143.18), *P* = 0.037]. Both MRI variables considered in the multivariable logistic regression resulted in a highly predictive model for UDs diagnosis (area under the ROC = 0.944); Figure 6 shows the ROC curve for this model, and Table 2 gives the corresponding predictive statistics and 95%CIs. The prediction statistics for this model were quite good, giving a 100% sensitivity and 88.9% specificity (Figure 7). Probability of UH diagnosis, alternative propensity scores, and covariate and outcome values are listed in Table 3. The predicted probability of UH at 0.529 cutoff was associated with suprapubic urethral sphincter length above 3.0 cm.

## DISCUSSION

MRI allows the visualization of the urethra and its supporting structures with great detail, especially with a multicoil MRI technique[15,16], and also permits the evaluation of urethral mobility and bladder neck competence during strain and Valsalva. The importance of the integrity of the urethral attachments to the maintenance of continence is supported by our findings that the visualization of the periurethral ligament and assessment of its status leads to the prediction of incontinence. The majority of continent control patients (70%) in our study had intact, symmetric periurethral ligament, as opposed to only 20% of incontinent women. Having intact, symmetric periurethral ligament reduced the odds of incontinence by 87% as compared to those who had periurethral disruption. Similar results of distorted periurethral ligaments were found in 56% of the patients with SUI *vs* 13% of the women who were continent in the study by Kim *et al*[12], and also in a recent study by Tasali *et al*[10] where there was a significantly higher pubourethral

**Table 1 Characteristics of participants according to continent *vs* incontinent status**

| Characteristics | Continent volunteers *n* = 10 | Incontinent patients *n* = 21 | *P* value |
|---|---|---|---|
| [1]Age (yr) | 45.1 (13.6) | 54.4 (11.8) | 0.0610 |
| [2]Race | | | |
| White | 5 (50) | 14 (67) | |
| Black | 5 (50) | 6 (29) | |
| Other | - | 1 (4) | |
| [1]BMI index | 29.98 (7.0) | 29.95 (6.6) | 0.9915 |
| [1]Parity, *n* births | 1.5 (1.2) | 1.9 (1.2) | 0.3329 |
| [2]Vaginal, *n* | 11 (65) | 39 (90) | |
| [2]C-section, *n* | 4 (24) | 2 (5) | |
| [2]Nullipara, *n* | 2 (12) | 2 (5) | |
| [2]OB Trauma, *n* | 0 (0) | 11 (52) | < 0.001[4] |
| [2]Hormones, *n* | 0 (0) | 5 (24) | |
| [2]Hysterectomy, *n* | 2 (2) | 8 (38) | |
| [3]Urethra wall thickness | | | |
| Ant total, mm | 0.47 (0.43-0.50) | 0.59 (0.33-0.84) | 0.5161 |
| Ant striated muscle, mm | 0.17 (0.13-0.2) | 0.21 (0.12-0.29) | 0.5467 |
| Ant smooth muscle, mm | 0.30 (0.3-0.3) | 0.38 (0.20-0.55) | 0.5055 |
| Post total, mm | 0.40 (0.36-0.43) | 0.39 (0.36-0.42) | 0.7713 |
| Post striated muscle, mm | 0.11 (0.08-0.13) | 0.09 (0.08-0.11) | 0.3180 |
| Post smooth muscle, mm | 0.29 (0.26-0.31) | 0.29 (0.27-0.32) | 0.7952 |
| [3]Urethral sphincter length | | | |
| Total, cm | 3.67 (3.45-3.88) | 3.77 (3.47-4.06) | 0.6432 |
| Length, suprapubic, cm | 3.03 (2.59-3.46) | 2.95 (2.65-3.24) | 0.7361 |
| [3]Urethra mobility angle | 53 (19.6-86.6) | 65 (50.1-80.2) | 0.4116 |
| [3]Bladder neck descent | | | |
| Total, cm | 1.98 (0.73-3.23) | 2.56 (1.96-3.15) | 0.3158 |
| Rest, above PCL, cm | 1.42 (0.43-2.41) | 1.51 (1.16-1.85) | 0.8195 |
| Strain, below PCL, cm | 0.56 (0.99-2.12) | 1.05 (0.46-1.63) | 0.4272 |
| [2]Funneling, *n* | 1 (10) | 11 (52) | 0.184 |
| [3]Retropubic distance to urethra, mm | 5.2 (4.19-6.20) | 5.0 (4.16-5.92) | 0.8259 |
| [3]Pubo-vaginal distance | | | |
| Right, cm | 1.81 (1.59-2.02) | 1.59 (1.47-1.70) | 0.0372 |
| Left, cm | 1.87 (1.72-2.01) | 1.67 (1.53-1.79) | 0.0475 |
| [2]Normal vaginal shape, *n* | 7 (70) | 8 (40) | 0.128 |
| [3]Puborectalis muscle thickness | | | |
| Right, mm | 3.4 (2.6-4.1) | 3.8 (1.8-3.0) | 0.4903 |
| Left, mm | 3.9 (2.9-4.9) | 4.7 (3.7-5.5) | 0.2748 |
| [1]Puborectalis muscle length | | | |
| Right, cm | 1.81 (0.30) | 1.59 (0.24) | 0.037 |
| Left, cm | 1.87 (0.21) | 1.67 (0.28) | 0.048 |
| [3]Puborectalis angle | | | |
| Right, ° | 21 (17-24) | 25 (21-28) | 0.0781 |
| Left, ° | 23 (19-27) | 24 (19-28) | 0.7323 |
| [2]Periurethral ligament status | | | |
| Intact/symmetric, *n* | 7 (70) | 4 (20) | 0.015[4] |
| Disrupted, *n* | 3 (30) | 16 (80) | |

[1]Data are presented as mean (standard deviation); [2]Data are presented as number of cases (%); [3]Data are presented as mean (95%CI); *P* value of *t*-test; [4]Fisher's exact test. BMI: Body mass index; PCL: Pubococcygeal line; OB: Obstetric trauma to include episiotomy; Ant: Anterior; Post: Posterior.

ligament distortion and larger vesicourethral angle in women with SUI. In our study the PVD was also found to be significantly associated with incontinence status. Incontinent women had a shorter PVD than the control volunteers. Previous studies demonstrated that the volume of paravaginal fascia (connective tissue that contained venous plexus anterior to vagina) was reduced in patients with stress incontinence compared to reference continent subjects[13], therefore our finding of shortening of the distance between the anterior vaginal wall and pubic wall in incontinent women may indirectly relate to diminishing volume of paravaginal tissue noted by deSouza *et al*[13]. However, in the study by Tasali *et al*[10], authors documented lack of association between the dimension of the retropubic space and the SUI. Notably, in our study there was no difference in BMI between the incontinent patients and continent volunteers, therefore our results should not be influenced by the contribution of retropubic fat pad to the PVD in our study sample.

Contrary to findings by Kim *et al*[12], Tasali *et al*[10], and Morgan *et al*[17], but in agreement with results from the study by Pontbriand-Drolet *et al*[18], we did not find a statistically significant difference between the urethral sphincter striated muscle thickness in women with SUI *vs* that in the continent group. In our

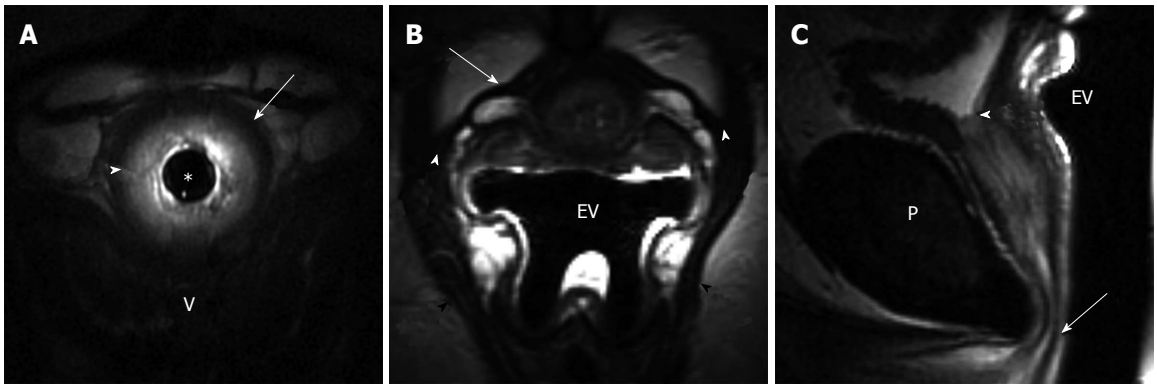


**Figure 1 41-year-old woman post one vaginal delivery with episiotomy, body mass index: 46.7, with occasional stress urinary incontinence.** A: Axial T2-weighted image of the mid urethra obtained with 14F endourethral MR coil (TR/TE 4816/68 ms) shows detailed depiction of the urethral sphincter with a hypointense outer layer of striated muscle (arrow) and inner hyperintense smooth muscle layer (arrowhead); B: Axial T2-weighted image at the mid urethra level obtained with endovaginal placement of MRInnervu coil (EV) (TR/TE 3000/92 ms) shows well-defined intact periurethral ligament (arrow) extending between the right and left puborectalis muscle (black arrowheads). Note symmetric, intact ligament attachment (white arrowheads); C: Sagittal T2-weighted image obtained with endovaginal placement of MRInnervu coil (EV) (TR/TE 4000/92 ms) shows normal resting position of the urethra, with distal end of urethral sphincter (arrow) at inferior pubis level (P). Note excellent coaptation of the mucosa at internal meatus/bladder neck level (arrowhead). V: Vagina.

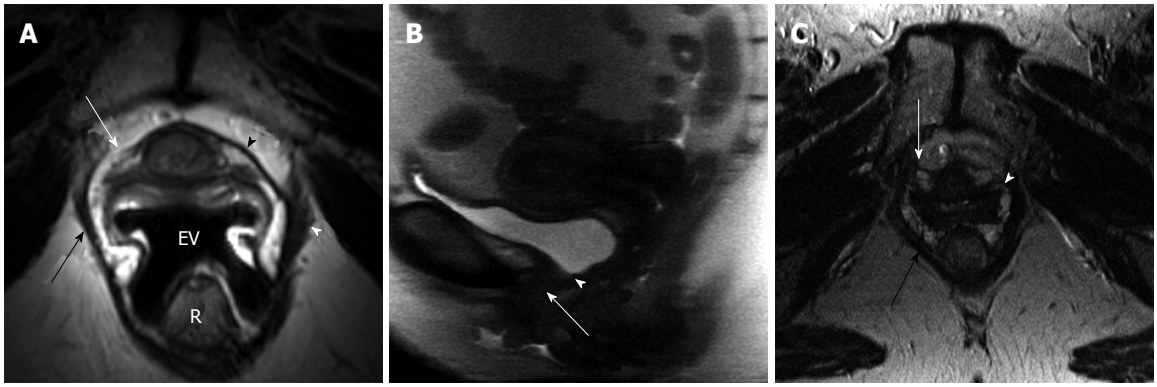


**Figure 2 51-year-old woman post two uneventful vaginal deliveries, body mass index: 24.3.** A: Axial oblique T2-weighted image at the mid urethra level (at 50% length from the internal meatus, about 1.2 cm), perpendicular to the axis of urethra, obtained with endovaginal placement of MRInnervu coil (EV) (TR/TE 3200/93 ms) shows disrupted attenuated right periurethral ligament (white arrow). Note intact left side of the periurethral ligament (black arrowhead) and its attachment to the puborectalis muscle (white arrowhead). Minimal asymmetric thinning of the right puborectalis muscle (black arrow); B: Sagittal SSFSE image (TR/TE 15000/78 ms) during strain shows hypermobility of the urethra (arrow). Note closure of bladder neck (arrowhead) during the urethral descent; C: Axial T2-weighted image of the pelvis at the level of mid urethra (at 50% from the internal meatus) obtained with pelvic coil (TR/TE 4666/85 ms) shows much less detail of the periurethral ligament compared to endovaginal MRI in A. It is difficult to appreciate the status of the ligament itself (white arrow) or its attachment (white arrowhead). Puborectalis muscle (black arrow) is well visualized. R: Rectum.

study, we performed precise measurements of the sphincter on images acquired with endourethral coil, both groups were comparable in body habitus and the mean age difference for incontinent patients and continent volunteers was less than a decade. It has been demonstrated that with aging, there is a decrease in the relative volume of urethral striated muscle and blood vessels[19].

Urethral mobility is tested clinically with the *Q* test[16]. Clinical *Q* test without visualization of urethral attachment defects may not be a reliable test, as continent women may also demonstrate hypermobility of the urethra. In our study groups there was an overlap between urethral mobility angles for continent women (mean 53 degrees) and incontinent women (mean 65 degrees) when assessed based on MRI. MRI is able to demonstrate not only the presence of hypermobility, but also other associated findings. UH is often accompanied by moderate to severe bladder descent with anterior bulging of the vagina. Bladder neck descent can be quantified and its competence/coaptation can be assessed on MRI along with hypermobility. We found an inverse correlation between bladder neck strain and MUCP that supports the hypothesis that, with increased inferior translation of the bladder neck due to loosening of the bladder neck attachment, there is decreasing urethral closure pressure caused by loss of coaptation of the sphincter as it descends. We also noted a correlation approaching significance between the increasing total urethral sphincter length and increasing VLPP; the longer the sphincter, the higher the leak point pressure.

On MRI, urethral and bladder descent are assessed in reference to the level of the pelvic floor which can be defined by the PCL[20-23]. Yang *et al*[21] demonstrated that

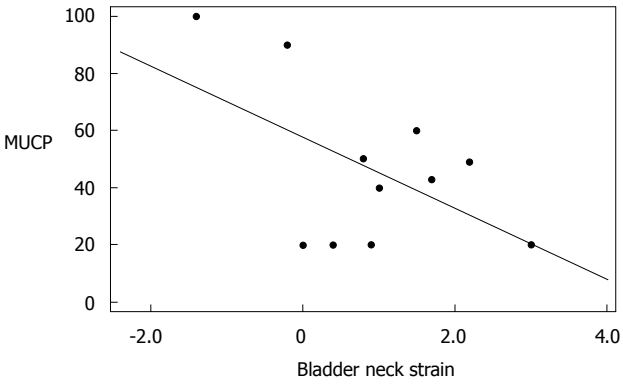


**Figure 3 Scatter plot of maximum urethral closure pressure (cm $H_20$) and bladder neck strain (distance in cm, traveled between position at rest and maximal strain) with fitted regression line (Pearson's correlation coefficient -0.537, *P* = 0.089).** MUCP: Maximum urethral closure pressure.

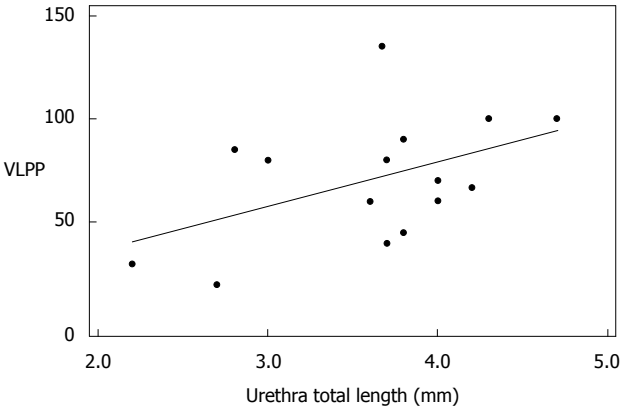


**Figure 4 Scatter plot of valsalva leak point pressure (cm $H_2O$) and total urethra sphincter length (mm) with fitted regression line (Person's correlation coefficient 0.478, *P* = 0.072).**

the normal vertical distance from PCL to the bladder base at strain should be no more than 1 cm below the line. In our study group, bladder neck descended to mean distance 0.56 cm below PCL in continent women during strain and 1.1 cm below PCL for incontinent women (*P* = 0.43).

Other findings associated with UH that can be detected on MRI are distortion of urethral support ligaments, either partial or complete. Partial defects include laxity, fluttering or focal attenuation of ligaments. Complete disruption shows a discontinuity of ligamentous fibers[6,12]; mostly affected and reproducibly visualized on imaging is PEL and pubourethral ligaments[10]. Findings are frequently accompanied by the abnormal vaginal configuration (loss of normal H-shape vaginal contour, or dropping vaginal fornix), best seen on axial images, and widening of the para-vaginal attachments. In our study group, normal vaginal shape was maintained in 70% of continent volunteers and 40% of incontinent women.

The levator ani muscle signal and integrity can be well evaluated on MR images, on axial and coronal T2-weighted images. Levator ani should be symmetric without defects or fraying. Abnormal signal in the levator

**Table 2 Predictive value statistics and corresponding 95%CI for urethral hypermobility diagnosis for both suprapubic urethra sphincter length and bladder neck funneling (present/absent)**

| Urethral hypermobility diagnosis - suprapubic urethra sphincter length and bladder neck funneling[1] | Estimate 95%CI |
|---|---|
| Sensitivity | 100.0% (66.4%, 100%)[2] |
| Specificity | 88.9% (51.8%, 99.7%) |
| Positive predictive value | 90.0% (55.5%, 99.7%) |
| Negative predictive value | 100.0% (63.1%, 100.0%)[2] |

A total of 18 incontinent women were included in the analysis. [1]ROC = 0.944; [2]One-sided 97.5% CI.

**Table 3 Probability of urethral hypermobility diagnosis, alternative propensity scores, and covariate and outcome values**

| Predicted probability of urethral hypermobility | Score | Funneling Y = 1, *n* = 0 | Suprapubic urethral sphincter length (cm) | UH = 1 ISD/mixed = 0 |
|---|---|---|---|---|
| 0.008 | -4.77 | 1 | 1.8 | 0 |
| 0.020 | -3.84 | 1 | 2.1 | 0 |
| 0.027 | -3.53 | 1 | 2.2 | 0 |
| 0.027 | -3.53 | 1 | 2.2 | 0 |
| 0.065 | -2.6 | 1 | 2.5 | 0 |
| 0.149 | -1.67 | 1 | 2.8 | 0 |
| 0.193 | -1.36 | 1 | 2.9 | 0 |
| 0.377 | -0.43 | 1 | 3.2 | 0 |
| 0.529 | 0.19 | 1 | 3.4 | 1 |
| 0.587 | 0.38 | 0 | 2.3 | 1 |
| 0.605 | 0.5 | 1 | 3.5 | 1 |
| 0.659 | 0.69 | 0 | 2.4 | 1 |
| 0.925 | 2.55 | 0 | 3.0 | 1 |
| 0.925 | 2.55 | 0 | 3.0 | 0 |
| 0.969 | 3.48 | 0 | 3.3 | 1 |
| 0.969 | 3.48 | 0 | 3.3 | 1 |
| 0.969 | 3.48 | 0 | 3.3 | 1 |
| 0.996 | 5.65 | 0 | 4.0 | 1 |

UH: Urethral hypermobility; ISD: Intrinsic sphincter defects.

muscle, when compared to the obturator internus, and thinning can be observed in patients with stress incontinence and can be a result of fatty infiltration and atrophy as well as direct muscle injury[24]. The normal thickness of the PRM is 5-6 mm[25]. Interruption of the muscle fibers, lateral deviation of the muscle that is frequently associated with vaginal shape distortion on the affected side, can be observed. In our study group however, there was no difference between the thickness of PRM or the puborectalis angle between incontinent and continent women.

In patients with SUI, there are some imaging findings that are more likely to be associated with ISD, such as a short urethra, urethral muscle thinning, or bladder neck weakness demonstrated by funneling. Our results in incontinent women demonstrate that when the total urethral sphincter is shorter than 3.0 cm, or when the segment of urethral sphincter above

**Figure 5 48-year-old woman post four vaginal deliveries, body mass index: 24.4.** Sagittal SSFSE image (TR/TE 15000/78 ms) during strain shows funneling at the bladder neck level (arrow).

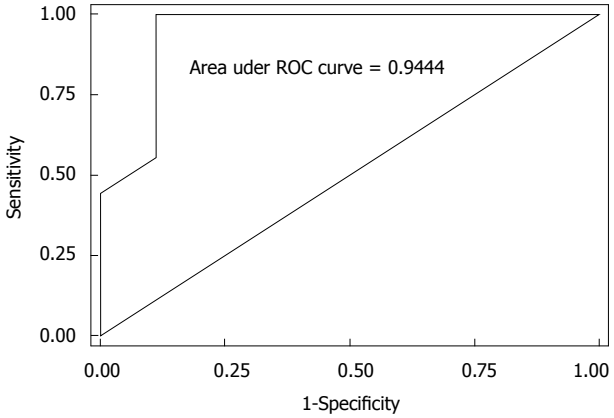


**Figure 6 Receiver operating characteristic curve for the logistic model of urodynamics diagnosis regressed on bladder neck funneling and suprapubic urethral sphincter length.**

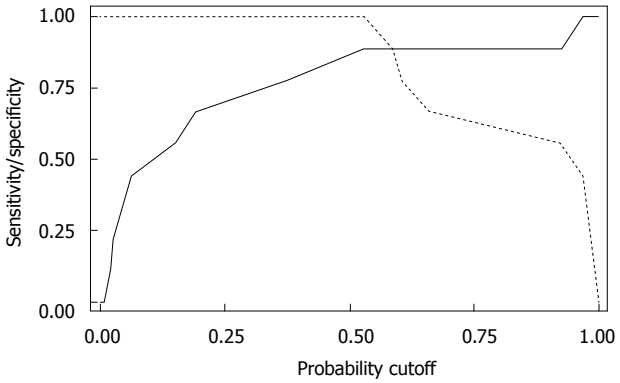


**Figure 7 Plot of sensitivity (solid line) and specificity (dashed line) as a function of the probability cut points obtained from the logistic model of urodynamics diagnosis regressed on bladder neck funneling and suprapubic urethral sphincter length.** The optimal probability cutoff point was determined to be 0.52.

the pelvic floor level is less than 3.0 cm, this decreased functional length of the urethra can lead to incontinence with urethral sphincter weakening associated with ISD on UDs. Also, funneling at the bladder neck, which is the opening of the urethrovesical junction at rest or during strain, can be seen on MRI in patients with SUI. An open bladder neck and proximal urethra was shown to indicate an ISD[26], however funneling can be also found in some postmenopausal continent women. In our study, funneling was seen in 52% of incontinent women and only in 1 (10%) continent volunteer. In a recent study by Pontbriand-Drolet *et al*[18] women with SUI symptoms were more likely to exhibit bladder neck funneling and a larger posterior urethrovesical angle at rest than both continent and mixed urinary incontinence women.

When we looked at the relationship of UDs diagnosis (SUI with pure UH *vs* SUI with ISD component) and the MRI data, both bladder neck funneling and the suprapubic urethral sphincter length were found to be predictive of UDs diagnosis; being positive for funneling on MRI reduced the odds of pure UH diagnosis on UDs by almost 95% as compared to no funneling. Our results are consistent with previous reports showing that funneling predicts ISD, as it results from the weakness of the proximal sphincter[26]. In contrast, increasing suprapubic urethral sphincter length was highly associated with a UDs diagnosis of pure UH, as the dysfunction of the sphincter results from the inferior translation of the urethra that is poorly supported rather than from shortening or intrinsic weakness of the sphincter itself. Both variables considered in the multivariable logistic regression analyses resulted in a highly predictive model for UDs diagnosis (area under the ROC = 0.944). The prediction statistics for this model was good, giving a 100% sensitivity and 88.9% specificity. However, due to a small size of the sample, the confidence intervals are large. A larger cohort study is needed to address these findings. Some patients may demonstrate imaging findings of both UH and ISD, as the ISD with bladder neck funneling may represent a secondary deficiency related to abnormal proximal urethral wall traction and shearing that can over time overcome the urethral coaptation such as in chronic hypermobility[27,28].

A limitation of our study is a relatively small sample size for incontinent group as only 18 incontinent women had a complete UDs exam to be included in the logistic regression model. Our study group patients were nearly-matched by age to within a decade. They were matched by BMI. However, there was a significant difference in the incidence of OB trauma, with 90% of incontinent patients reporting vaginal deliveries and 52% at least one incident of episiotomy, perineal laceration, or forceps delivery. No history of OB trauma was reported in the control group. This finding indirectly may relate to a known risk of pelvic floor injury during vaginal delivery as a cause of SUI. However, since the study sample was small, we were unable to control for individual types of injury to directly correlate the MRI findings with the severity of pelvic floor trauma. Another potential limitation of our study is imaging in the supine position, which is not a physiological position when patients

experience SUI. However, we performed dynamic pelvic floor strain imaging to allow assessment of the changes in the urethra that take place during increases of intra-abdominal pressures. Our study group was imaged with pelvic MRI that included three different imaging components, with intraurethral imaging and dynamic pelvic floor imaging performed in all patients, and endovaginal or endorectal imaging being performed based on patients' preference. This could have resulted in some measurements inconsistencies where endovaginal coil placement may have caused vaginal shape distortion.

In conclusion, our study demonstrated that there are specific morphological defects in women with SUI detectable on MRI that can be evaluated to differentiate incontinence related to the pure UH *vs* incontinence that has a component of ISD. Currently, MRI is usually considered in the diagnostic work-up of women who failed prior surgeries for incontinence or who have severe and complex pelvic organ prolapse. Further studies are needed to address the effects of aging, parity, pelvic floor injury, and hormonal status on SUI, in the context of specific anatomical defects related to SUI that can be observed and quantified on MR images, in order to evaluate the role of MRI in the assessment and treatment planning of women with SUI.

## COMMENTS

### Background

Anatomical defects related to stress urinary incontinence (SUI) can be observed and quantified with magnetic resonance imaging (MRI) and may contribute to diagnostic work-up and treatment planning of women with SUI.

### Research frontiers

To date the role of MRI in the specific diagnosis of SUI caused by urethral hypermobility (UH) and/or intrinsic sphincter deficiency (ISD) has not been documented.

### Innovations and breakthroughs

The results from this pilot study suggest that two MRI parameters, the bladder neck funneling and length of the suprapubic urethral sphincter on MRI can predict the UH and ISD types of incontinence when urodynamics results are used as a reference standard.

### Applications

MRI may play a critical role in assessing the contribution of hypermobility and sphincteric dysfunction to the stress urinary incontinence in women when considering treatment options. Further studies are warranted to assess the potential added value of MRI to management strategy selection.

### Peer-review

The authors performed an interesting pilot study aimed at the identification of MRI parameters differentiating UH and intrinsic sphincteric deficiency in women with SUI.

## REFERENCES


1 **Abrams P**, Blaivas JG, Stanton SL, Andersen JT. The standardisation of terminology of lower urinary tract function. The International Continence Society Committee on Standardisation of Terminology. *Scand J Urol Nephrol Suppl* 1988; **114**: 5-19 [PMID: 3201169]

2 **Blaivas JG**, Romanzi LJ, Heritz DM. Urinary incontinence: pathophysiology, evaluation, treatment overview, and nonsurgical management. In: Walsh P, Retik A, Vaughan E, Wein A, editors. Campbell's Urology. Philadelphia: WB Saunders Co., 1997: 1007-1043

3 **McGuire EJ**, Fitzpatrick CC, Wan J, Bloom D, Sanvordenker J, Ritchey M, Gormley EA. Clinical assessment of urethral sphincter function. *J Urol* 1993; **150**: 1452-1454 [PMID: 8411422]

4 **Haliloglu B**, Karateke A, Coksuer H, Peker H, Cam C. The role of urethral hypermobility and intrinsic sphincteric deficiency on the outcome of transobturator tape procedure: a prospective study with 2-year follow-up. *Int Urogynecol J* 2010; **21**: 173-178 [PMID: 19802505 DOI: 10.1007/s00192-009-1010-y]

5 **Sand PK**, Bowen LW, Panganiban R, Ostergard DR. The low pressure urethra as a factor in failed retropubic urethropexy. *Obstet Gynecol* 1987; **69**: 399-402 [PMID: 3822288]

6 **Shah SM**, Gaunay GS. Treatment options for intrinsic sphincter deficiency. *Nat Rev Urol* 2012; **9**: 638-651 [PMID: 23027065 DOI: 10.1038/nrurol.2012.177]

7 **Macura KJ**, Genadry RR. Female urinary incontinence: pathophysiology, methods of evaluation and role of MR imaging. *Abdom Imaging* 2008; **33**: 371-380 [PMID: 17610006 DOI: 10.1007/s00261-007-9257-6]

8 **el-Sayed RF**, Morsy MM, el-Mashed SM, Abdel-Azim MS. Anatomy of the urethral supporting ligaments defined by dissection, histology, and MRI of female cadavers and MRI of healthy nulliparous women. *AJR Am J Roentgenol* 2007; **189**: 1145-1157 [PMID: 17954653 DOI: 10.2214/AJR.07.2215]

9 **Macura KJ**, Genadry RR, Bluemke DA. MR imaging of the female urethra and supporting ligaments in assessment of urinary incontinence: spectrum of abnormalities. *Radiographics* 2006; **26**: 1135-1149 [PMID: 16844938 DOI: 10.1148/rg.264055133]

10 **Tasali N**, Cubuk R, Sinanoğlu O, Sahin K, Saydam B. MRI in stress urinary incontinence: endovaginal MRI with an intracavitary coil and dynamic pelvic MRI. *Urol J* 2012; **9**: 397-404 [PMID: 22395838]

11 **Stoker J**, Rociu E, Bosch JL, Messelink EJ, van der Hulst VP, Groenendijk AG, Eijkemans MJ, Laméris JS. High-resolution endovaginal MR imaging in stress urinary incontinence. *Eur Radiol* 2003; **13**: 2031-2037 [PMID: 12692675 DOI: 10.1007/s00330-003-1855-2]

12 **Kim JK**, Kim YJ, Choo MS, Cho KS. The urethra and its supporting structures in women with stress urinary incontinence: MR imaging using an endovaginal coil. *AJR Am J Roentgenol* 2003; **180**: 1037-1044 [PMID: 12646452 DOI: 10.2214/ajr.180.4.1801037]

13 **deSouza NM**, Daniels OJ, Williams AD, Gilderdale DJ, Abel PD. Female urinary genuine stress incontinence: anatomic considerations at MR imaging of the paravaginal fascia and urethra initial observations. *Radiology* 2002; **225**: 433-439 [PMID: 12409577 DOI: 10.1148/radiol.2252011347]

14 **Constantinou CE**. Dynamics of female pelvic floor function using urodynamics, ultrasound and Magnetic Resonance Imaging (MRI). *Eur J Obstet Gynecol Reprod Biol* 2009; **144** Suppl 1: S159-S165 [PMID: 19303690 DOI: 10.1016/j.ejogrb.2009.02.021]

15 **Bergman A**, McCarthy TA, Ballard CA, Yanai J. Role of the Q-tip test in evaluating stress urinary incontinence. *J Reprod Med* 1987; **32**: 273-275 [PMID: 3585870]

16 **Macura KJ**, Genadry R, Borman TL, Mostwin JL, Lardo AC, Bluemke DA. Evaluation of the female urethra with intraurethral magnetic resonance imaging. *J Magn Reson Imaging* 2004; **20**: 153-159 [PMID: 15221821 DOI: 10.1002/jmri.20058]

17 **Morgan DM**, Umek W, Guire K, Morgan HK, Garabrant A, DeLancey JO. Urethral sphincter morphology and function with and without stress incontinence. *J Urol* 2009; **182**: 203-209 [PMID: 19450822 DOI: 10.1016/j.juro.2009.02.129]

18 **Pontbriand-Drolet S**, Tang A, Madill SJ, Tannenbaum C, Lemieux MC, Corcos J, Dumoulin C. Differences in pelvic floor morphology between continent, stress urinary incontinent, and mixed urinary incontinent elderly women: An MRI study. *Neurourol Urodyn* 2015; Epub ahead of print [PMID: 25727524 DOI: 10.1002/nau.22743]

19 **Carlile A**, Davies I, Rigby A, Brocklehurst JC. Age changes in the human female urethra: a morphometric study. *J Urol* 1988; **139**:

532-535 [PMID: 3343739]
20 **Borghesi G**, Simonetti R, Goldman SM, Szejnfeld J, Srougi M, Ortiz V, Bruschini H. Magnetic resonance imaging urodynamics. Technique development and preliminary results. *Int Braz J Urol* 2006; **32**: 336-341; discussion 341 [PMID: 16813681 DOI: 10.1590/S1677-55382006000300015]
21 **Yang A**, Mostwin JL, Rosenshein NB, Zerhouni EA. Pelvic floor descent in women: dynamic evaluation with fast MR imaging and cinematic display. *Radiology* 1991; **179**: 25-33 [PMID: 2006286 DOI: 10.1148/radiology.179.1.2006286]
22 **Gufler H**, DeGregorio G, Allmann KH, Kundt G, Dohnicht S. Comparison of cystourethrography and dynamic MRI in bladder neck descent. *J Comput Assist Tomogr* 2000; **24**: 382-388 [PMID: 10864072 DOI: 10.1097/00004728-200005000-00005]
23 **Goh V**, Halligan S, Kaplan G, Healy JC, Bartram CI. Dynamic MR imaging of the pelvic floor in asymptomatic subjects. *AJR Am J Roentgenol* 2000; **174**: 661-666 [PMID: 10701605 DOI: 10.2214/ajr.174.3.1740661]
24 **Tunn R**, Paris S, Fischer W, Hamm B, Kuchinke J. Static magnetic resonance imaging of the pelvic floor muscle morphology in women with stress urinary incontinence and pelvic prolapse. *Neurourol Urodyn* 1998; **17**: 579-589 [PMID: 9829422 DOI: 10.1002/(SICI)1520-6777(1998)17:6<579::AID-NAU2>3.0.CO;2-R]
25 **Singh K**, Reid WM, Berger LA. Magnetic resonance imaging of normal levator ani anatomy and function. *Obstet Gynecol* 2002; **99**: 433-438 [PMID: 11864670 DOI: 10.1016/S0029-7844(01)01743-4]
26 **Mostwin JL**. Urinary incontinence. *J Urol* 1995; **153**: 352-353 [PMID: 7815581 DOI: 10.1097/00005392-199502000-00016]
27 **Mostwin JL**, Genadry R, Saunders R, Yang A. Stress incontinence observed with real time sonography and dynamic fastscan magnetic resonance imaging--insights into pathophysiology. *Scand J Urol Nephrol Suppl* 2001; **(207)**: 94-99; discussion 106-125 [PMID: 11409622 DOI: 10.1080/003655901750175033]
28 **Huang WC**, Yang JM. Bladder neck funneling on ultrasound cystourethrography in primary stress urinary incontinence: a sign associated with urethral hypermobility and intrinsic sphincter deficiency. *Urology* 2003; **61**: 936-941 [PMID: 12736011 DOI: 10.1016/S0090-4295(02)02558-X]

**P- Reviewer**: Francesco C, Tsai HH
**S- Editor**: Qiu S **L- Editor**: A **E- Editor**: Jiao XK

World Journal of Radiology

Submit a Manuscript: http://www.wjgnet.com/esps/
Help Desk: http://www.wjgnet.com/esps/helpdesk.aspx
DOI: 10.4329/wjr.v7.i11.405

*World J Radiol* 2015 November 28; 7(11): 405-414
ISSN 1949-8470 (online)


ORIGINAL ARTICLE

Case Control Study

# Partial correlation analyses of global diffusion tensor imaging-derived metrics in glioblastoma multiforme: Pilot study

David Cortez-Conradis, Camilo Rios, Sergio Moreno-Jimenez, Ernesto Roldan-Valadez

David Cortez-Conradis, Magnetic Resonance Unit, Medica Sur Clinic and Foundation, Mexico City CP 14050, Mexico

Camilo Rios, Department of Neurochemistry, National Institute of Neurology and Neurosurgery, Mexico City CP 14269, Mexico

Sergio Moreno-Jimenez, Radioneurosurgery Unit, National Institute of Neurology and Neurosurgery, Mexico City CP 14269, Mexico

Ernesto Roldan-Valadez, Faculty of Health Sciences, Panamerican University, Mexico City CP 03920, Mexico

Ernesto Roldan-Valadez, Magnetic Resonance Unit, Medica Sur Clinic and Foundation, Puente de Piedra # 150, Col, Toriello Guerra, Deleg, Tlalpan, Mexico City CP 14050, Mexico

Author contributions: Roldan-Valadez E drafted the manuscript; all authors participated in the literature search, summary and interpretation; all authors edited and approved the final manuscript.

Supported by The Medica Sur Clinic and Foundation (in part); David Cortez-Conradis was research fellow at the MRI Unit of Medica Sur Clinic and Foundation from 2012 to 2014. Ernesto Roldan-Valadez was Coordinator of Research at the MRI Unit of Medica Sur Clinic and Foundation from 2010 to April 2015.

Institutional review board statement: The protocol for this study was previously accepted by the institutional review board of Medica Sur Clinic and Foundation (Project #2011-EXT-05).

Informed consent statement: Because this was a retrospective study using exclusively, quantitative parameter of MRI postprocessed images, the approved protocol included a waiver of informed consent statement.

Conflict-of-interest statement: The authors have no conflicts of interests to declare.

Data sharing statement: The dataset of this study is available from the corresponding author at Dryad repository.



Correspondence to: Ernesto Roldan-Valadez, MD, MSc, PhD, Magnetic Resonance Unit, Medica Sur Clinic and Foundation, Puente de Piedra # 150, Col, Toriello Guerra, Deleg, Tlalpan, Mexico City CP 14050, Mexico. ernest.roldan@usa.net
Telephone: +52-55-54247230
Fax: +52-55-54244429

Received: April 20, 2015
Peer-review started: April 21, 2015
First decision: June 9, 2015
Revised: August 31, 2015
Accepted: October 12, 2015
Article in press: October 13, 2015
Published online: November 28, 2015

## Abstract

**AIM:** To determine existing correlates among diffusion tensor imaging (DTI)-derived metrics in healthy brains and brains with glioblastoma multiforme (GBM).

**METHODS:** Case-control study using DTI data from brain magnetic resonance imaging of 34 controls (mean, 41.47; SD, ± 21.94 years; range, 21-80 years) and 27 patients with GBM (mean, SD; 48.41 ± 15.18 years; range, 18-78 years). Image postprocessing using FSL software calculated eleven tensor metrics: fractional (FA) and relative anisotropy; pure isotropic (p) and anisotropic diffusions (q), total magnitude of diffusion (L); linear (Cl), planar (Cp) and spherical tensors (Cs); mean (MD), axial (AD) and radial diffusivities (RD). Partial correlation analyses (controlling the effect of age

and gender) and multivariate Mancova were performed.

**RESULTS:** There was a normal distribution for all metrics. Comparing healthy brains *vs* brains with GBM, there were significant very strong bivariate correlations only depicted in GBM: [FA↔Cl (+)], [FA↔q (+)], [p↔AD (+)], [AD↔MD (+)], and [MD↔RD (+)]. Among 56 pairs of bivariate correlations, only seven were significantly different. The diagnosis variable depicted a main effect [F-value (11, 23) = 11.842, $P \leqslant 0.001$], with partial eta squared = 0.850, meaning a large effect size; age showed a similar result. The age also had a significant influence as a covariate [F (11, 23) = 10.523, $P < 0.001$], with a large effect size (partial eta squared = 0.834).

**CONCLUSION:** DTI-derived metrics depict significant differences between healthy brains and brains with GBM, with specific magnitudes and correlations. This study provides reference data and makes a contribution to decrease the underlying empiricism in the use of DTI parameters in brain imaging.

**Key words:** Brain neoplasms; Diffusion tensor imaging; Magnetic resonance imaging; Software tools; Statistics as topic



**Core tip:** Diffusion tensor imaging (DTI)-derived metrics depict specific magnitudes and correlations; and significant differences between healthy brains and brains with glioblastoma multiforme (GBM). For example, only 5 bivariate correlations in GBM depicted significant very strong association: [FA↔Cl (+)], [FA↔q (+)], [p↔AD (+)], [D↔MD (+)], and [MD↔RD (+)]. Among 56 pairs of correlations, only seven were significantly different. Diagnosis showed a main effect [F-value (11, 23) = 11.842, $P \leqslant 0.001$], with a large effect size (partial eta squared = 0.850); a similar result was observed for age. This study makes a contribution to decrease the empiricism in the use of DTI parameters in brain imaging.

Cortez-Conradis D, Rios C, Moreno-Jimenez S, Roldan-Valadez E. Partial correlation analyses of global diffusion tensor imaging-derived metrics in glioblastoma multiforme: Pilot study. *World J Radiol* 2015; 7(11): 405-414 Available from: URL: http://www.wjgnet.com/1949-8470/full/v7/i11/405.htm DOI: http://dx.doi.org/10.4329/wjr.v7.i11.405

## INTRODUCTION

In the last decade, advanced magnetic resonance (MR) techniques have been adopted for the diagnosis and follow-up of intra-axial brain tumors[1], with a rising interest in novel diffusion tensor imaging (DTI)-derived metrics showing clinical applicability either in a tumor-region assessment (ROIs measurements in the cystic cavity, enhancing rim, edema, and normal-appearing white matter regions)[2-4]; or in a global approach (whole-brain selected values of DTI-derived biomarkers are able to assemble a predictive model for the diagnosis of glioblastoma multiforme)[4].

Conventional MR evaluation of glial tumors reporting qualitative and quantitative findings in the $T_1$-w post gadolinium, Flair and $T_2$-w sequences represents a caveat in the pathologic and regional evaluation of astrocytomas grades Ⅱ to Ⅳ, as evidence suggest these tumors should received a global instead of regional brain assessment: glial tumors can depict manifold regions with different histologic grading, conditioning that biopsies reviewed by the neuropathologist may not reflect higher malignancy degrees in supplemental tumor regions, which may lead to underrating pathology reports[5]. There is a low correlation between visible margins of tumoral areas on conventional MR images with the true areas of tumor infiltration[5] this is due to microscopic invasion of white matter (WM) regions[6,7], extending dozens of millimeters from conspicuous areas of viable tumor[8].

Several combinations of the terms of the diagonalized diffusion tensor, that is, the eigenvalues $\lambda_1$, $\lambda_2$, and $\lambda_3$, have been reported as scalar measures of diffusion, such as: fractional (FA) and relative anisotropy (RA); pure isotropic (p) and anisotropic diffusions (q), total magnitude of diffusion (L); linear (Cl), planar (Cp) and spherical tensors (Cs); mean (MD), axial (AD) and radial (RD) diffusivities[2,3,9-11]; Table 1. However, to best of our knowledge, there is currently neither a clear understanding of the expected measurements among these variables, nor existing studies reporting their correlations; likewise there is a lack of consensus about which of the tensor metrics available should be used in the evaluation of brain tumors.

In this study we (1) used a global approach, that is, a single measure of the whole brain for each metric aimed to determine the normal limits (magnitudes) of previously reported DTI-derived tensor metrics in healthy brains and brains of patients with glioblastoma multiforme (GBM); (2) assessed the statistical significance between DTI values in these groups; and (3) analyzed the DTI-metrics correlates considering the influence of clinical diagnosis (healthy *vs* GBM brains).

## MATERIALS AND METHODS

### *Subjects*

Case-control study design; inclusion criteria considered preoperative brain MR examinations between January 2010 and September 2012 of patients with at first (suspected) diagnosis and later pathology confirmation of astrocytoma grade Ⅳ, GBM according to the World Health Organization. Exclusion criteria applied to corticosteroid or antibiotic treatment, lesions with areas

**Table 1 Diffusion tensor imaging-derived tensor metric formulas**

| |
|---|
| MD |
| $MD = D = (\lambda_1 + \lambda_2 + \lambda_3)/3$ |
| FA |
| $FA = [(3/2) \times (q/L)]^{1/2}$ |
| $= (3/2)^{1/2}\{[(\lambda_1 - D)^2+(\lambda_2 - D)^2+(\lambda_3 - D)^2]/(\lambda_1^2+\lambda_2^2+\lambda_3^2)\}^{1/2}$ |
| RA |
| $RA = q/p = \{[(\lambda_1 - D)^2 + (\lambda_2 - D)^2+(\lambda_3 - D)^2]^{1/2}\}/[3^{1/2}D]$ |
| RD |
| $RD = (\lambda_2 + \lambda_3)/2$ |
| AD |
| $AD = \lambda_1$ |
| Cs |
| $Cs = 3\lambda_3/(\lambda_1 + \lambda_2 + \lambda_3)$ |
| p |
| $p = 3^{1/2}D = (\lambda_1 + \lambda_2 + \lambda_3)/3^{1/2}$ |
| q |
| $q = [(\lambda_1 - D)^2 + (\lambda_2 - D)^2 + (\lambda_3 - D)^2]^{1/2}$ |
| L |
| $L = (p^2 + q^2)^{1/2} = (\lambda_1^2 + \lambda_2^2 + \lambda_3^2)^{1/2}$ |
| Cl |
| $Cl = (\lambda_1 - \lambda_2)/(\lambda_1 + \lambda_2 + \lambda_3)$ |
| Cp |
| $Cp = 2(\lambda_2 - \lambda_3)/(\lambda_1 + \lambda_2 + \lambda_3)$ |

MD: Mean diffusivity; FA: Fractional anisotropy; RA: Relative anisotropy; RD: Radial diffusivity; AD: Axial diffusivity; Cs: Spherical tensor; p: Pure isotropic diffusion; q: Pure anisotropic diffusion; L: Total magnitude of the diffusion tensor; Cl: Linear tensor; Cp: Planar tensor.

related to calcification and/or haemorrhage and previous brain surgery. A control group included young and elderly healthy volunteers recruited among the enrolled interns and medical residents of the hospital as well as elderly subjects from our Geriatric unit. All volunteers received detailed health examinations; exclusion criteria considered major neurological, psychiatric, or cardiovascular diseases. A radiologist interpreted the MR images blinded to the patient's history. MR examinations with other structural abnormalities were excluded. The local Institutional Review Boards approved the study (Project #2011.044), patients and also volunteers gave "informed consent".

### *Brain image acquisition*

MR sequences included conventional axial $T_2$-w imaging, axial FLAIR, axial SPGR, DWI and axial $T_1$-w imaging, using 0.1 mmol/kg of Magnevist (Schering, Berlin, Germany); healthy volunteers did not received endogenous contrast. DTI was performed using a SS SE EPI sequence. DTI sequence was acquired with 25 directions, a b-value of 1000 s/mm$^2$ and with b-value of 0 s/mm$^2$; axial plane included 40 contiguous slices with 2.4 mm thickness, no intersection gap, TR 17000, TE 80 ms, with parallel imaging to reduce off-resonance artifacts (PI factor was 2); FOV 25 cm × 25 cm, and matrix size 128 × 128. Images were acquired using a 3T clinical scanner (GE Healthcare, HDxt Signa, Waukesha, WI, United States); and a 8-channels head coil (Invivo, Gainesville city, Florida).

### *Image postprocessing and data analysis*

The methodology for calculation of global DTI-derived tensor metrics has been recently described[4]; each one of the eleven metrics in this study (Cl, Cp, Cs, RA, AD, RD, MD, FA, p, q, L) represent a single global measure of a whole-brain taking into account the higher (λ1), medium (λ2), and lower (λ3) eigenvalues of DTI[12].

### *Statistical analysis*

**Sample size:** With the intention to run a Mancova analysis to investigate whether mean differences between healthy brains and brains of patients with GBM (combining different variables) occurred randomly, we followed Pallant's recommendation for sample size[13], the absolute minimum of cases to have in each cell must equal at least the number of dependent variables; in our study, we had twenty-two cells (two levels of our independent variable: healthy brains/brains with GBM, and eleven dependent variables for each). The study was run in 34 controls and 27 patients; this numbers also follow the recommendation of Tabachnick and Fidell[14], for whom a minimum of 20 cases in each cell should ensure a "robustness" analysis. Assumptions testing included normality, multicollinearity and homogeneity tests[13,15]. We performed a partial correlation analysis to calculate association values between each pair of parameters. Considering the age range and the gender of the subjects in our study, this method allowed us to calculate correlations among tensor metrics without the effect of age and gender; independent analyses were carried out for each group (healthy brains *vs* brains with GBM). Each correlation coefficient was interpreted as very strong (at least of 0.8), moderately strong (0.6 up to 0.8), fair (0.3 up to 0.6) and poor (less than 0.3). Squaring *r*-values represented the coefficient of determination, the proportion of variance that each two compared variables had in common[16]. We additionally tested the statistical significance of the difference between *r* coefficients from both groups by converting each pair of *r*-values into a standard z scores, then using the formula proposed by Pallant[17]: Observed *Z* value $\leqslant$ -1.96 or $\geqslant$ 1.96 were considered statistically significantly different.

A two-way Mancova identified diagnosis and gender differences in tensor metrics measurements[18]. The eleven tensor-metrics represented the dependent variables used; independent variables were the diagnosis and gender; the effect of age was controlled. The effect size was obtained using the Eta squared value[19]: 0.01 to 0.06 represents small effect, 0.06 to 0.14 medium and > 0.14 shows a large effect[20]. A *P*-value < 0.05 depicted a significant difference.

**Software:** All analyses were carried out using the IBM® SPSS® Statistics software (version 22.0.0.0 IBM Corporation; Armonk, NY).

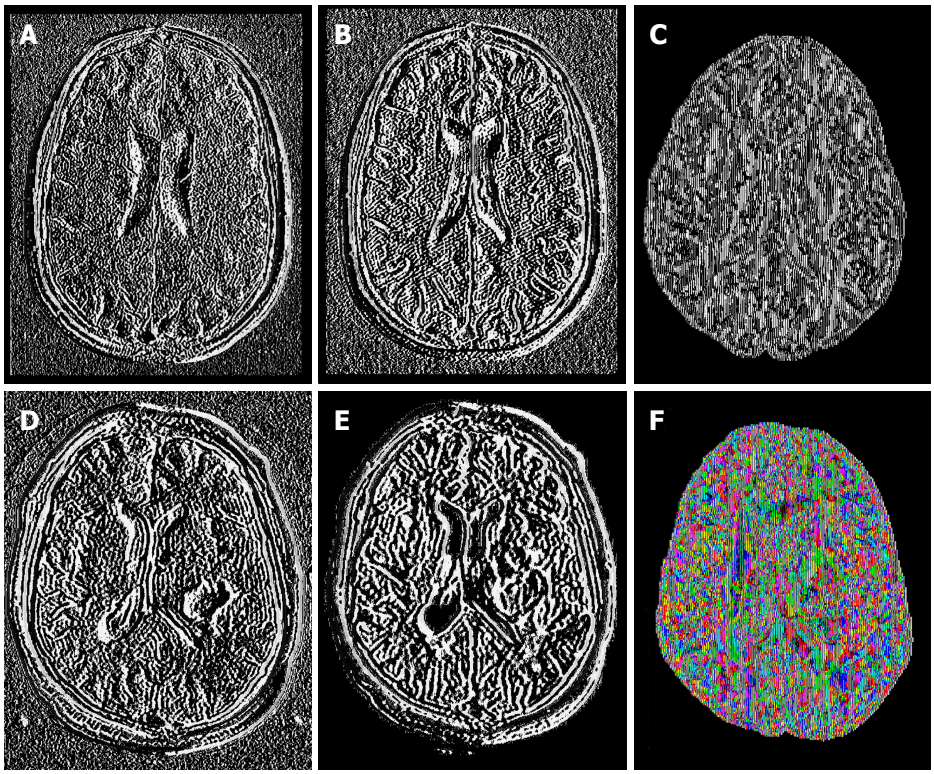


**Figure 1 Example of some sequences and diffusion tensor imaging maps from healthy brains (upper row) and brains with glioblastoma multiforme (lower row): T1-postgadolinium images (A and D), Flair sequence (B and E); pure isotropic diffusion (C), color map of the V1-vector (F).**

## RESULTS

### *Demographic data and quantitative DTI tensor maps*

The study was conducted in 61 subjects; 27 patients: 13 females (mean age 50.0 ± 15.4 years, range 31-73 years) and 14 males (mean age 46.93 ± 15.4 years, range 18-78 years); and 34 controls: 26 females (mean age 41.04 ± 22.3 years, range 21-80 years) and 8 males (mean age 42.88 ± 21.89 years, range 24-72 years). Tensor maps generated using the FSL software, added up to 671 tensor-metrics measurements. Figure 1 shows an example of some of the MR sequences and tensor-metric maps included in the data analyses.

### *Normality tests, magnitudes of means and SD*

There was a normal distribution for all metrics. In order to understand the corresponding magnitudes of each DTI biomarker (previously not reported), we counted the number of decimal places to the right of the decimal point: five tensor metrics reported mean values within the tenths place: Cs, FA, RA, Cp and Cl; none tensor measurement fell in the hundredths place; five tensors values fell in the thousandths place: L, p, AD, MD and RD; and one tensor metrics had values in the ten thousandths place: q. Table 2 shows the means and SD ordered by descending means.

### *Partial correlation analyses*

A scatterplot for each group showed no serious violation of the assumptions of linearity, homoscedasticity, and outliers (Figure 2). In healthy brains, significant very strong bivariate correlations were observed for: [Cs↔RA (-)], [Cs↔Cp (-)], [Cs↔L (-)], [RA↔Cp (+)], [RA↔Cl (+)], [Cp↔Cl (+)], [L↔p (+)], [L↔AD (+)], [L↔MD (+)], [L↔RD (+)], [p↔MD (+)], [p↔RD (+)] and [MD↔RD (+)]; and moderately strong significant correlations were calculated for: [FA↔q (+)], [p↔AD (+)], [AD↔MD (+)] and [AD↔RD (+)].

In brains with GBM, the corresponding significant very strong bivariate correlations included: [Cs↔RA (-)], [Cs↔Cp (-)], [Cs↔L (-)], [FA↔Cl (+)], [FA↔q (+)], [RA↔Cp (+)], [RA↔Cl (+)], [Cp↔Cl (+)], [L↔p (+)], [L↔AD (+)], [L↔MD (+)], [p↔AD (+)], [p↔MD (+)], [p↔RD (+)], [AD↔MD (+)], and [MD↔RD (+)]; the moderately strong significant correlations were observed in: [Cl↔q (+)], [AD↔RD (+)] and [AD↔q (+)]. Table 3 present the correlations among the global tensor-metrics controlled for the effect of age and gender.

From the 55 pairs of bivariate correlations in each a group, statistical significances of the difference between *r* coefficients were observed in only seven pairs of variables: [Cs↔Cp], [FA↔Cl], [FA↔q], [RA↔q], [C↔q], [L↔p] and [L↔MD].

### *Mancova analysis*

After adjusting for age, there was not interaction effect between the gender and clinical diagnosis [F (11, 23) = 1.115, *P* = 0.394]. There was not main affect of gender [F (11, 23) = 2.060, *P* = 0.069]; however, the main effect of diagnosis was statistically significant [F (11, 23)

**Table 2 Means, SD and correlations (controlled for the effect of age and gender) in healthy brains**

| Tensor metric | | | | | | | | | | | | Mean | SD |
|---|---|---|---|---|---|---|---|---|---|---|---|---|---|
| | | Cs | | | | | | | | | | 0.756690 | 0.032259 |
| FA | Pearson's R | -0.456 | | | | | | | | | | 0.284317 | 0.018917 |
| | *P*-value | 0.029 | FA | | | | | | | | | | |
| RA | Pearson's R | -0.992 | 0.434 | | | | | | | | | 0.224873 | 0.029523 |
| | *P*-value | 0.000 | 0.039 | RA | | | | | | | | | |
| Cp | Pearson's R | -0.979 | 0.460 | 0.938 | | | | | | | | 0.133346 | 0.017086 |
| | *P*-value | 0.000 | 0.031 | 0.000 | Cp | | | | | | | | |
| Cl | Pearson's R | -0.946 | 0.442 | 0.978 | 0.855 | | | | | | | 0.111574 | 0.016583 |
| | *P*-value | 0.000 | 0.024 | 0.000 | 0.000 | Cl | | | | | | | |
| L | Pearson's R | 0.372 | -0.115 | -0.416 | -0.317 | -0.186 | | | | | | 0.002275 | 0.000100 |
| | *P*-value | 0.117 | 0.578 | 0.076 | 0.200 | 0.408 | L | | | | | | |
| p | Pearson's R | 0.179 | -0.095 | -0.214 | -0.020 | -0.014 | 0.945 | | | | | 0.002096 | 0.000087 |
| | *P*-value | 0.477 | 0.652 | 0.395 | 0.938 | 0.953 | 0.000 | p | | | | | |
| AD | Pearson's R | 0.322 | -0.012 | -0.348 | -0.287 | 0.019 | 0.804 | 0.761 | | | | 0.001553 | 0.000056 |
| | *P*-value | 0.179 | 0.952 | 0.144 | 0.249 | 0.933 | 0.000 | 0.000 | AD | | | | |
| MD | Pearson's R | 0.181 | -0.096 | -0.215 | -0.022 | -0.014 | 0.945 | 1.000 | 0.762 | | | 0.001210 | 0.000050 |
| | *P*-value | 0.473 | 0.649 | 0.391 | 0.934 | 0.953 | 0.000 | 0.000 | 0.000 | MD | | | |
| RD | Pearson's R | 0.053 | -0.297 | -0.119 | 0.426 | -0.131 | 0.877 | 0.954 | 0.628 | 0.954 | | 0.001046 | 0.000072 |
| | *P*-value | 0.821 | 0.132 | 0.606 | 0.054 | 0.542 | 0.000 | 0.000 | 0.001 | 0.000 | RD | | |
| q | Pearson's R | -0.077 | 0.698 | 0.019 | 0.257 | 0.138 | 0.138 | 0.153 | 0.393 | 0.152 | 0.406 | 0.000445 | 0.000055 |
| | *P*-value | 0.721 | 0.000 | 0.929 | 0.225 | 0.492 | 0.502 | 0.466 | 0.047 | 0.467 | 0.029 | q | |

FA: Fractional anisotropy; RA: Relative anisotropy; Cp: Planar tensor; p: Pure isotropic diffusion; q: Pure anisotropic diffusion; L: Total magnitude of the diffusion tensor; Cl: Linear tensor; MD: Mean diffusivity; RD: Radial diffusivity; AD: Axial diffusivity.

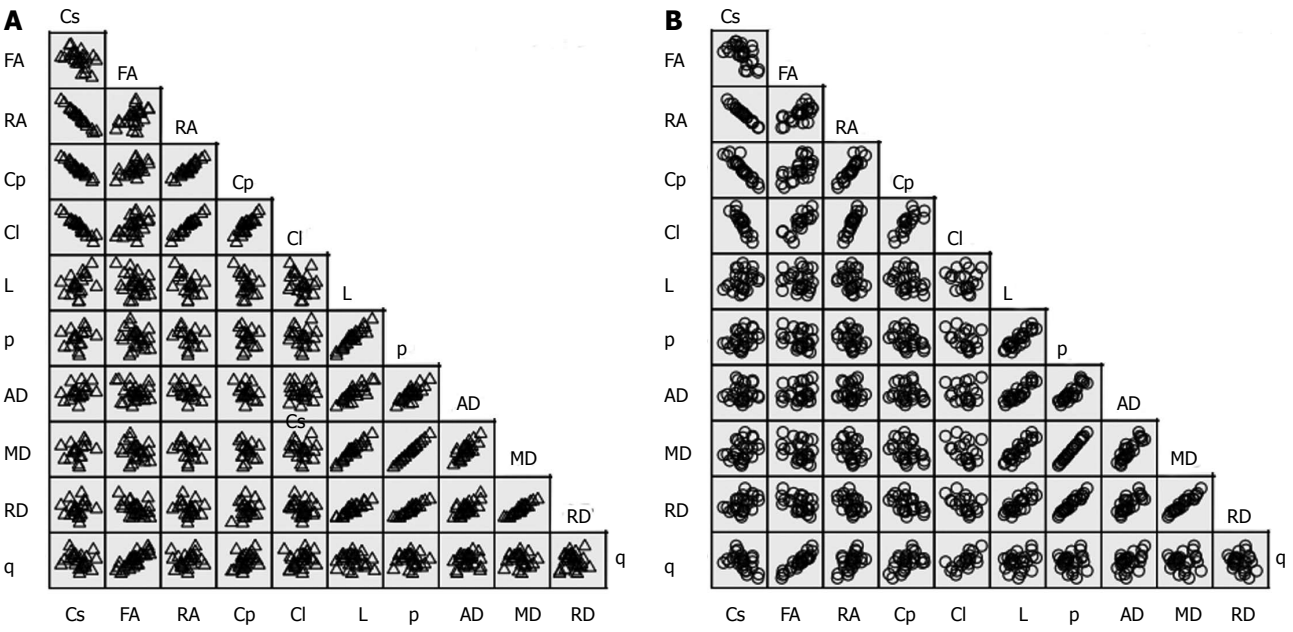


**Figure 2 Scatter matrix of the variable's data grouped by diagnosis.** A: Normal brains; B: Brains with GBM. MD: Mean diffusivity; FA: Fractional anisotropy; RA: Relative anisotropy; RD: Radial diffusivity; AD: Axial diffusivity; Cs: Spherical tensor; p: Pure isotropic diffusion; q: Pure anisotropic diffusion; L: Total magnitude of the diffusion tensor; Cl: Linear tensor; Cp: Planar tensor; GBM: Glioblastoma multiforme.

= 11.842, $P < 0.001$], corresponding to a large effect size (partial $\eta^2 = 0.850$). The age also had a significant influence as a covariate [F (11, 23) = 10.523, $P < 0.001$], and large effect size (partial $\eta^2 = 0.834$). Table 4 and Figure 3 depict the estimated marginal means; the age was controlled at the value of 43.92 years.

## DISCUSSION

It is still not completely understood a priori which are the magnitudes and associations among DTI measurements observed in the evaluation of brain tumors[9]. The clinical relevance of these associations has been supported by several studies in the MR-DTI literature: Cs, Cp, Cl, FA and MD, have been related with brain abscesses, GBM and brain metastasis[2]; p, q and L measurements have also been previously applied to the evaluation of GBM and brain metastasis[3,21]; AD has been reported in encephalomyelitis of the spinal cord[22], AD and RD have been correlated with brain development[23], infantile

**Table 3 Means, SD and correlations (controlled for the effect of age and gender) in brains with glioblastoma multiforme**

| Tensor metric | | | | | | | | | | | | Mean | SD |
|---|---|---|---|---|---|---|---|---|---|---|---|---|---|
| | | Cs | | | | | | | | | | 0.771562 | 0.066812 |
| FA | Pearson's R | -0.570 | | | | | | | | | | 0.253531 | 0.028425 |
| | *P*-value | 0.003 | FA | | | | | | | | | | |
| RA | Pearson's R | -1.000 | 0.592 | | | | | | | | | 0.201778 | 0.053287 |
| | *P*-value | 0.000 | 0.002 | RA | | | | | | | | | |
| Cp | Pearson's R | -0.936 | 0.576 | 0.901 | | | | | | | | 0.133265 | 0.043503 |
| | *P*-value | 0.000 | 0.003 | 0.000 | Cp | | | | | | | | |
| Cl | Pearson's R | -0.904 | 0.819 | 0.969 | 0.803 | | | | | | | 0.098462 | 0.011929 |
| | *P*-value | 0.000 | 0.000 | 0.000 | 0.000 | Cl | | | | | | | |
| L | Pearson's R | 0.096 | 0.151 | 0.009 | -0.159 | 0.182 | | | | | | 0.002111 | 0.000140 |
| | *P*-value | 0.648 | 0.472 | 0.967 | 0.446 | 0.469 | L | | | | | | |
| p | Pearson's R | 0.156 | -0.129 | -0.094 | -0.216 | -0.177 | 0.834 | | | | | 0.001961 | 0.000123 |
| | *P*-value | 0.456 | 0.540 | 0.664 | 0.299 | 0.482 | 0.000 | p | | | | | |
| AD | Pearson's R | -0.111 | 0.343 | 0.191 | 0.053 | 0.173 | 0.871 | 0.881 | | | | 0.001397 | 0.000080 |
| | *P*-value | 0.596 | 0.094 | 0.372 | 0.803 | 0.492 | 0.000 | 0.000 | AD | | | | |
| MD | Pearson's R | 0.154 | -0.125 | -0.090 | -0.215 | -0.173 | 0.837 | 1.000 | 0.883 | | | 0.001132 | 0.000071 |
| | *P*-value | 0.462 | 0.550 | 0.675 | 0.303 | 0.491 | 0.000 | 0.000 | 0.000 | MD | | | |
| RD | Pearson's R | 0.305 | -0.411 | -0.260 | -0.360 | -0.395 | 0.706 | 0.954 | 0.699 | 0.953 | | 0.000999 | 0.000073 |
| | *P*-value | 0.139 | 0.041 | 0.219 | 0.077 | 0.105 | 0.000 | 0.000 | 0.000 | 0.000 | RD | | |
| q | Pearson's R | -0.484 | 0.928 | 0.539 | 0.466 | 0.736 | 0.430 | 0.187 | 0.629 | 0.191 | -0.114 | 0.000363 | 0.000048 |
| | *P*-value | 0.014 | 0.000 | 0.007 | 0.019 | 0.001 | 0.032 | 0.371 | 0.001 | 0.361 | 0.588 | q | |

MD: Mean diffusivity; FA: Fractional anisotropy; RA: Relative anisotropy; RD: Radial diffusivity; AD: Axial diffusivity; Cs: Spherical tensor; p: Pure isotropic diffusion; q: Pure anisotropic diffusion; L: Total magnitude of the diffusion tensor; Cl: Linear tensor; Cp: Planar tensor.

**Table 4 Estimated marginal means SE and CI of diffusion tensor imaging-derived tensor metrics (the effect of age was controlled at the value of 43.92 yr)**

| Tensor metric | Healthy brains | | | | Brains with GBM | | | |
|---|---|---|---|---|---|---|---|---|
| | Mean | SE | 95%CI | | Mean | SE | 95%CI | |
| | | | Lower | Upper | | | Lower | Upper |
| Cs | 0.739511 | 0.009798 | 0.719577 | 0.759446 | 0.766043 | 0.007824 | 0.750126 | 0.781960 |
| FA | 0.290160 | 0.005721 | 0.278520 | 0.301799 | 0.255660 | 0.004568 | 0.246366 | 0.264954 |
| RA | 0.241025 | 0.008008 | 0.224734 | 0.257317 | 0.211498 | 0.006394 | 0.198490 | 0.224506 |
| Cp | 0.141366 | 0.007941 | 0.125210 | 0.157522 | 0.137961 | 0.006341 | 0.125061 | 0.150860 |
| Cl | 0.119041 | 0.003243 | 0.112443 | 0.125638 | 0.099495 | 0.002589 | 0.094227 | 0.104763 |
| L | 0.002287 | 0.000029 | 0.002227 | 0.002347 | 0.002103 | 0.000024 | 0.002055 | 0.002151 |
| p | 0.002122 | 0.000027 | 0.002068 | 0.002177 | 0.001946 | 0.000021 | 0.001903 | 0.001990 |
| AD | 0.001558 | 0.000020 | 0.001518 | 0.001598 | 0.001395 | 0.000016 | 0.001363 | 0.001426 |
| MD | 0.001225 | 0.000015 | 0.001194 | 0.001257 | 0.001124 | 0.000012 | 0.001099 | 0.001149 |
| RD | 0.001059 | 0.000015 | 0.001029 | 0.001089 | 0.000988 | 0.000012 | 0.000964 | 0.001012 |
| q | 0.000454 | 0.000011 | 0.000432 | 0.000476 | 0.000371 | 0.000009 | 0.000354 | 0.000389 |

MD: Mean diffusivity; FA: Fractional anisotropy; RA: Relative anisotropy; RD: Radial diffusivity; AD: Axial diffusivity; Cs: Spherical tensor; p: Pure isotropic diffusion; q: Pure anisotropic diffusion; L: Total magnitude of the diffusion tensor; Cl: Linear tensor; Cp: Planar tensor; GBM: Glioblastoma multiforme.

spasm[24], amyotrophic lateral sclerosis[25], schizophrenia[26], and brain tumors[27]; with only one recent study integrating a tumor-region diagnostic evaluation of 11 DTI-metrics[4]. MD is understood as a synonym of the coefficient of diffusion in different space guidelines[28]. FA measures the directional movement of water molecules in the brain[29], it is an index of anisotropic diffusivity reflecting the integrity of myelinated axons[30].

One advantage of using a global approach is that not the only the size of the viable tumor is included (enhanced regions with Gadolinium), but also the non-apparent regions that undergo microscopic infiltration (edema and increased-size regions). Additionally, by using a global approach, all the inhomogeneity nature of GBM is included in a global measurement, a situation missed in a regional approach.

Some interesting associations are worthy to be noted: for example, there is no consensus of normal parameters between fractional anisotropy and mean diffusivity in a day-to-day basis[3]; traditionally, MD and FA showed negative correlation with increased MD and decreased FA in high signal-intensity perilesional regions when compared with normal axonal areas[31]; we observed a poor-negative non-significant correlation when controlling the effect of age and gender. One explanation might be that, different to MD that quantifies the degree of water molecules motion which is independ of myelinated axons; FA directly measures

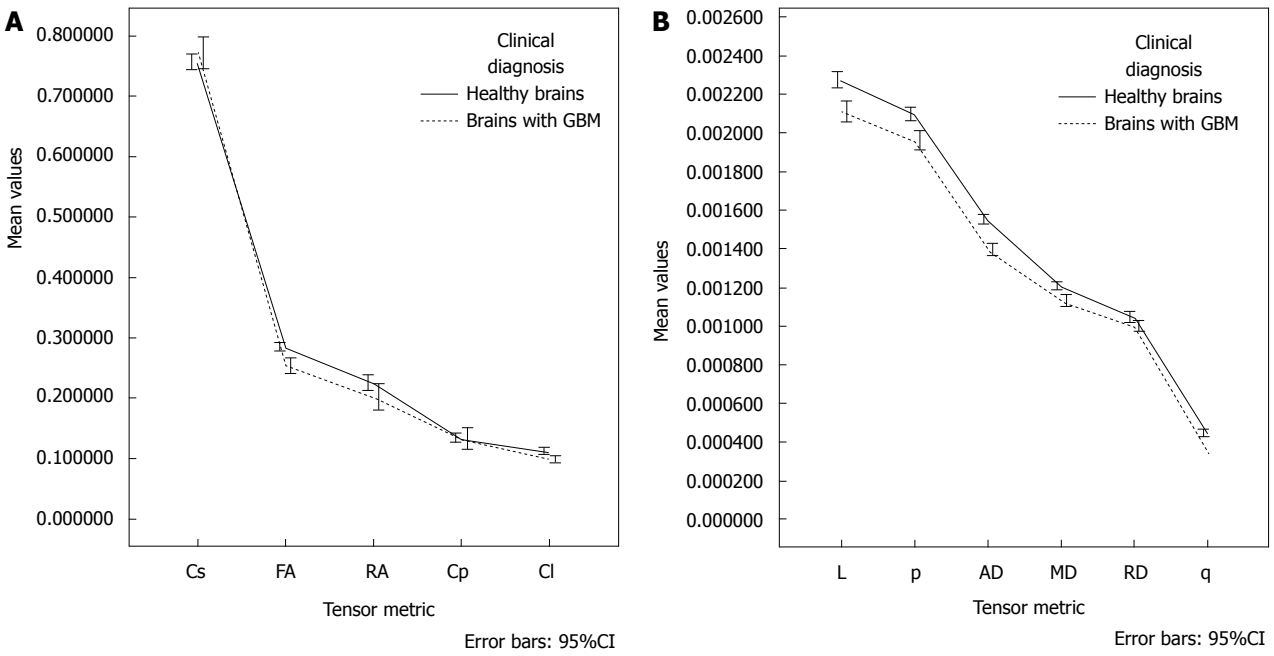


**Figure 3 Graphs of the estimated marginal means for each tensor metric, the influence of age was controlled at the value of 43.92 years.** MD: Mean diffusivity; FA: Fractional anisotropy; RA: Relative anisotropy; RD: Radial diffusivity; AD: Axial diffusivity; p: Pure isotropic diffusion; q: Pure anisotropic diffusion; L: Total magnitude of the diffusion tensor; Cl: Linear tensor; Cp: Planar tensor; GBM: Glioblastoma multiforme.

movement of water molecules along myelinated axons, it is a weighted anisotropic diffusion average[10]. The absence of partial correlation analyses in previous reports could explain some conflicts of diffusivity and anisotropy values characterizing tumoral regions[3,32]. For MD, the highest-significant correlation ($r$ = 1) was observed with p and RD, a positive correlation between RD and MD have been previously observed in human brains[33]. We found an inverse relationship between MD with Cp, which seems opposite to previously suggested direction measuring MD, FA and the shape tensor metrics (Cp, Cs, Cl) between tumoral brain tissue, metastasis and abscesses[2]. FA's mechanisms of decreasing its value in brain tumors are still unclear: it might represents neuronal and axonal infiltration with widening of extracellular space[32]; or tumoral substitution with decrement of extracellular space (this would explain the negative association between fractional anisotropy and tumoral cells)[34]. The FA can also be calculated by dividing q over L[9]; the q parameter could depict a comprehensive profile of brain tumor activity, in our study this parameter showed the highest-significant strength of correlation with FA ($r$ = 0.928) in brains with GBM, it would seem an expected finding from its formula (ratio of q/L); however, our findings differ from other authors who observed no significant changes of q measurements in metastatic regions; this finding suggests that L instead of q, might be the main factor influencing the variability of FA. The inverse correlation between FA and RD observed in our study had been reported[33], although there are not statements of the expected magnitudes among these correlations.

For most of the correlates observed in this study, there was a decrease in the strength of the linear relationship after controlling the effect of age and gender. Poor correlations should be interpreted cautiously; in clinical settings these measurements might have the physiological implication to represent independent biological biomarkers. We do not have an explanation for the differences in the strength and directions of the observed correlations between normal and GBM brains, it is possible that the detailed info from the tumor may be obscured by the global measurement; the gender variable neither had interaction nor main effect in the observed measurements of DTI metrics; however, age did have a significant effect that should be controlled by researchers, as this variable could affect the p-value of the results.

As we mentioned in the results, there where some very strong, significant correlations observed only in brains with GBM (despite we use a global approach): [FA ↔Cl (+)], [FA↔q (+)], [p↔AD (+)], [D↔MD (+)], and [MD↔RD (+)]; these findings were an indicator for us that, these parameters might be among the most useful for clinical diagnosis and/or treatment planning.

Comparing healthy brains *vs* brains with GBM, there were significant very strong bivariate correlations only depicted in GBM: [FA↔Cl (+)], [FA↔q (+)], [p↔AD (+)], [D↔MD (+)], and [MD↔RD (+)].

Our data might represent useful information for radiologist and/or bio imaging researchers trying to explain the relationships between tensor metrics to clinicians (neurologists, neurosurgeons, psychiatrist, neuro-oncologists, *etc.*) as well as in the preparation of prospective studies with clinical application. Further studies should address the significant differences we found in the correlations between healthy brains and brains with GBM, none of these results have been

previously reported. It will be interesting to know the data analyses from other research groups that help validate and support the clinical significance of the results presented in this study.

Several limitations in our study and factors that influence the clinical application of DTI-metrics need to be addressed: our decision to evaluate a single, global measure for each tensor-metric relationships came up from reports depicting absence of $P < 0.05$ differences in fractional anisotropy between enhanced and not enhanced tumoral areas[35]; not significant differences between FA and MD measurements in tumor regions with distinct $T_2$-w signal-intensities[36], and findings of increased variability of FA measurements amont diverse brain areas[3], making all them a patent lack of agreement between investigators. Also, some studies have evaluated only selected ROIs within the tumors, missing major components of viable tumor and perilesional infiltration zones; other studies reporting ROIs only of the whole viable tumor mass, excluded many times peritumoral regions, wasting the opportunity to identify areas of severe infiltration within axons[3].

Although conventional sequences for the evaluation of GBM include the use of contrast enhancement agents (gadolinium), two situations could be observed in the managing assessment of these tumors: some regions of GBM could not depict enhancement because the tumor has not damaged enough the blood brain barrier, and second, there might be patients not able to receive gadolinium because chronic kidney failure; in both cases a global measurement of brain tissue would take into account non-evident abnormalities of the brain architecture.

Nowadays, there is still scarce evidence regarding the potential of these DTI biomarkers, for example, besides the clinical acceptance of FA; some studies have showed a significant increment of p (mean 68%) with evident decrement of q (mean 42%) in infiltrated axons[37]. Also, some proved parameters, for example, the increase of RD as a marker of demyelination and axonal loss has not had generalization in its use[33]. These facts reflect the limited acceptance of DTI by the medical community; it has not attained the same anatomic validation of structural myelin studies and so far does not discrimiante individual tracts or complex functional linkages among synapses[38]. DTI-derived tensor metrics intricacies to characterize brain tissue in health and disease might be affected among other variables by the quotient of extracellular to intracellular compartments; blood vessels density, abnormal accumulation of fluid in the interstitium, microscopic cysts, and the extracellular meshwork of proteins and carbohydrates that binds cells together[39]. The clinical value of our findings has yet to be determined, and the biological impact of the different metrics should be explained in more detail in clinical journals.

In conclusion, a comprehensive understanding of the currently available DTI-derived parameters will help researchers in the decision of which one to include in the diagnosis and treatment planning of brain tumors, researchers could know a priori expected relationships in a prospective analysis decreasing the underlying empiricism in this area. It is possible that several tensor metrics answer different questions; also, variations in DTI measures are not specific of one histologic type of tumor, which broaden the application of these biomarkers to a wider variety of intracranial pathologies. Given the increased availability of open source software in MRI units around the world, it is anticipated that measurements of DTI-derived tensor metrics may become a low-cost and common used approach.

## COMMENTS

### Background

In the last decade, advanced magnetic resonance techniques have adopted the use of diffusion tensor imaging (DTI)-derived metrics in the evaluation of glioblastoma multiforme. However, to best of our knowledge, there is currently neither a clear understanding of the expected measurements among these variables, nor existing studies reporting their correlations; likewise there is a lack of consensus about which of the tensor metrics available should be used in the evaluation of brain tumors.

### Research frontiers

This study reports measurement of eleven DTI-derived tensor metrics which have only recently been described in the litarature: fractional (FA) and relative anisotropy (RA); pure isotropic (p) and anisotropic diffusions (q), total magnitude of diffusion (L); linear (Cl), planar (Cp) and spherical tensors (Cs); mean (MD), axial (AD) and radial (RD) diffusivities.

### Innovations and breakthroughs

Compared with previous studies, this report provides novel quantitative data of DTI-derived metrics in normal brains and brain with glioblastoma multiforme, its main aim is to decrease the underlying empiricism involving these parameters. Additionally, innovation is depicted in the use of a global approach (whole-brain) instead of the conventional tumor-region assessment; this approach warrants the inclusion of all tumor regions (ROIs measurements in the cystic cavity, enhancing rim, edema, and normal-appearing white matter regions).

### Applications

Data in this study might represent useful information for radiologist and/or bio imaging researchers trying to explain the relationships between tensor metrics to clinicians (neurologists, neurosurgeons, psychiatrist, neuro-oncologists, *etc.*) as well as in the preparation of prospective studies with clinical application. The authors believed that the very strong, significant correlations observed only in brains with glioblastoma multiforme (GBM) (despite the authors use a global approach): [FA↔Cl (+)], [FA↔q (+)], [p↔AD (+)], [D↔MD (+)], and [MD↔RD (+)]; might be among the most useful parameters for clinical in diagnosis and/or treatment planning. Furthermore, the gender variable neither had interaction nor main effect in the observed measurements of DTI metrics; however, age did have a significant effect that should be controlled by researchers, as this variable could affect the *P*-value of the results. One advantage of using a global approach is that not the only the size of the viable tumor is included (enhanced regions with Gadolinium), but also the non-apparent regions that undergo microscopic infiltration (edema and increased-size regions). As this DTI-derived metrics do not require the use of a constrat agent (gadolinium), the proposed global approach takes into account non-evident abnormalities of the brain architecture which occurs in some regions of GBM without enhancement because the tumor has not damaged enough the blood brain barrier, and also, this approach can be used in patients not able to receive gadolinium because chronic kidney failure.

### Terminology

The DTI-derived metrics reported in this study were calculated from the below

described formulas:

MD = D = $(\lambda_1 + \lambda_2 + \lambda_3)/3$

FA = $[(3/2)(q/L)]^{1/2}$

= $(3/2)^{1/2}\{[(\lambda_1 - D)^2+(\lambda_2 - D)^2+(\lambda_3 - D)^2]/(\lambda_1^2 + \lambda_2^2 + \lambda_3^2)\}^{1/2}$

RA = q/p = $\{[(\lambda_1 - D)^2 + (\lambda_2 - D)^2 + (\lambda_3 - D)^2]^{1/2}\}/[3^{1/2}D]$

RD = $(\lambda_2 + \lambda_3)/2$

AD = $\lambda_1$

Cs = $3\lambda_3/(\lambda_1 + \lambda_2 + \lambda_3)$

Pure Isotropic Diffusion (p)

p = $3^{1/2}D = (\lambda_1 + \lambda_2 + \lambda_3)/3^{1/2}$

Pure Anisotropic Diffusion (q)

q = $[(\lambda_1 - D)^2+(\lambda_2 - D)^2+(\lambda_3 - D)^2]^{1/2}$

Total Magnitude of the Diffusion Tensor (L)

L = $(p^2 + q^2)^{1/2} = (\lambda_1^2 + \lambda_2^2 + \lambda_3^2)^{1/2}$

Linear Tensor (Cl)

Cl = $(\lambda_1 - \lambda_2)/(\lambda_1 + \lambda_2 + \lambda_3)$

Planar Tensor (Cp)

Cp = $2(\lambda_2 - \lambda_3)/(\lambda_1 + \lambda_2 + \lambda_3)$

### *Peer-review*

The authors studied the relationships of 11 DTI-derived tensor metrics between healthy brains and brains with GBM. They used a noval technique, *i.e.*, a single global measure of the whole brain for each metric rather than a conventional approach of measuring the entire tumor or some regions.

## REFERENCES


1 **Young GS**. Advanced MRI of adult brain tumors. *Neurol Clin* 2007; **25**: 947-973, viii [PMID: 17964022 DOI: 10.1016/j.ncl.2007.07.010]

2 **Toh CH**, Wei KC, Ng SH, Wan YL, Lin CP, Castillo M. Differentiation of brain abscesses from necrotic glioblastomas and cystic metastatic brain tumors with diffusion tensor imaging. *AJNR Am J Neuroradiol* 2011; **32**: 1646-1651 [PMID: 21835939 DOI: 10.3174/ajnr.A2581]

3 **Wang W**, Steward CE, Desmond PM. Diffusion tensor imaging in glioblastoma multiforme and brain metastases: the role of p, q, L, and fractional anisotropy. *AJNR Am J Neuroradiol* 2009; **30**: 203-208 [PMID: 18842762 DOI: 10.3174/ajnr.A1303]

4 **Roldan-Valadez E**, Rios C, Cortez-Conradis D, Favila R, Moreno-Jimenez S. Global diffusion tensor imaging derived metrics differentiate glioblastoma multiforme vs. normal brains by using discriminant analysis: introduction of a novel whole-brain approach. *Radiol Oncol* 2014; **48**: 127-136 [PMID: 24991202 DOI: 10.2478/raon-2014-0004]

5 **Rees JH**, Smirniotopoulos JG, Jones RV, Wong K. Glioblastoma multiforme: radiologic-pathologic correlation. *Radiographics* 1996; **16**: 1413-1438; quiz 1462-1463 [PMID: 8946545]

6 **Scherer HJ**. A critical review: the pathology of cerebral gliomas. *J Neurol Psychiatry* 1940; **3**: 147-177 [PMID: 21610973]

7 **Johnson PC**, Hunt SJ, Drayer BP. Human cerebral gliomas: correlation of postmortem MR imaging and neuropathologic findings. *Radiology* 1989; **170**: 211-217 [PMID: 2535765]

8 **DeAngelis LM**. Brain tumors. *N Engl J Med* 2001; **344**: 114-123 [PMID: 11150363 DOI: 10.1056/NEJM200101113440207]

9 **Peña A**, Green HA, Carpenter TA, Price SJ, Pickard JD, Gillard JH. Enhanced visualization and quantification of magnetic resonance diffusion tensor imaging using the p: q tensor decomposition. *Br J Radiol* 2006; **79**: 101-109 [PMID: 16489190 DOI: 10.1259/bjr/24908512]

10 **Le Bihan D**, Mangin JF, Poupon C, Clark CA, Pappata S, Molko N, Chabriat H. Diffusion tensor imaging: concepts and applications. *J Magn Reson Imaging* 2001; **13**: 534-546 [PMID: 11276097]

11 **Koch K**, Wagner G, Schachtzabel C, Schultz CC, Güllmar D, Reichenbach JR, Sauer H, Schlösser RG. Neural activation and radial diffusivity in schizophrenia: combined fMRI and diffusion tensor imaging study. *Br J Psychiatry* 2011; **198**: 223-229 [PMID: 21357881 DOI: 10.1192/bjp.bp.110.081836]

12 **Tugcu B**, Postalci LS, Gunaldi O, Tanriverdi O, Akdemir H. Efficacy of clinical prognostic factors on survival in patients with glioblastoma. *Turk Neurosurg* 2010; **20**: 117-125 [PMID: 20401838 DOI: 10.5137/1019-5149.JTN.2461-09.4]

13 **Pallant J**. Multivariate analysis of variance. In: Pallant J, editor. SPSS Survival Manual. 4th ed. Crows Nest, NSW, Australia: Allen and Unwin, 2011: 283-296

14 **Tabachnick BG**, Fidell LS. Multivariate Normality. In: Tabachnick BG, Fidell LS, editors. Using Multivariate Statistics. 5th ed. 2007: 251

15 **Pallant J**. Assesing Normality. In: Pallant J, editor. SPSS Survival Manual. 4th ed. Crows Nest, NSW, Australia: Allen and Unwin, 2011: 59-64

16 **Chan YH**. Biostatistics 104: correlational analysis. *Singapore Med J* 2003; **44**: 614-619 [PMID: 14770254]

17 **Pallant J**. Testing the statistical significance of the difference between correlation coefficients. In: Pallant J, editor. SPSS Survival Manual. 4th ed. Crows Nest, NSW, Australia: Allen and Unwin, 2011: 139-141

18 **Pallant J**. Analysis of covariance. In: Pallant J, editor. SPSS Survival Manual. 4th ed. Crows Nest, NSW, Australia: Allen and Unwin, 2011: 297-318

19 **Pallant J**. Calculating effect size. In: Pallant J, editor. SPSS Survival Manual. 4th ed. Crows Nest, Australia: Allen and Unwin, 2011: 254-255

20 **Cohen JW**. Statistical power analysis for the behavioral sciences. 2nd ed. Hillsdale, NJ: Lawrence Erlbaum Associates, 1988: 284-287

21 **Price SJ**, Jena R, Burnet NG, Hutchinson PJ, Dean AF, Peña A, Pickard JD, Carpenter TA, Gillard JH. Improved delineation of glioma margins and regions of infiltration with the use of diffusion tensor imaging: an image-guided biopsy study. *AJNR Am J Neuroradiol* 2006; **27**: 1969-1974 [PMID: 17032877]

22 **Budde MD**, Xie M, Cross AH, Song SK. Axial diffusivity is the primary correlate of axonal injury in the experimental autoimmune encephalomyelitis spinal cord: a quantitative pixelwise analysis. *J Neurosci* 2009; **29**: 2805-2813 [PMID: 19261876 DOI: 10.1523/JNEUROSCI.4605-08.2009]

23 **Kumar R**, Nguyen HD, Macey PM, Woo MA, Harper RM. Regional brain axial and radial diffusivity changes during development. *J Neurosci Res* 2012; **90**: 346-355 [PMID: 21938736 DOI: 10.1002/jnr.22757]

24 **Simao GN**, Zarei Mahmoodabadi S, Snead OC, Go C, Widjaja E. Abnormal axial diffusivity in the deep gray nuclei and dorsal brain stem in infantile spasm treated with vigabatrin. *AJNR Am J Neuroradiol* 2011; **32**: 199-203 [PMID: 20801762 DOI: 10.3174/ajnr.A2224]

25 **Metwalli NS**, Benatar M, Nair G, Usher S, Hu X, Carew JD. Utility of axial and radial diffusivity from diffusion tensor MRI as markers of neurodegeneration in amyotrophic lateral sclerosis. *Brain Res* 2010; **1348**: 156-164 [PMID: 20513367 DOI: 10.1016/j.brainres.2010.05.067]

26 **Seal ML**, Yücel M, Fornito A, Wood SJ, Harrison BJ, Walterfang M, Pell GS, Pantelis C. Abnormal white matter microstructure in schizophrenia: a voxelwise analysis of axial and radial diffusivity. *Schizophr Res* 2008; **101**: 106-110 [PMID: 18262770 DOI: 10.1016/j.schres.2007.12.489]

27 **Chen F**, Zhang X, Li M, Wang R, Wang HT, Zhu F, Lu DJ, Zhao H, Li JW, Xu Y, Zhu B, Zhang B. Axial diffusivity and tensor shape as early markers to assess cerebral white matter damage caused by brain tumors using quantitative diffusion tensor tractography. *CNS Neurosci Ther* 2012; **18**: 667-673 [PMID: 22712656 DOI: 10.1111/j.1755-5949.2012.00354.x]

28 **Mori S**, Barker PB. Diffusion magnetic resonance imaging: its principle and applications. *Anat Rec* 1999; **257**: 102-109 [PMID: 10397783 DOI: 10.1002/(SICI)1097-0185(19990615)257:3<102::AID-AR7>3.0.CO;2-6]

29 **Lu S**, Ahn D, Johnson G, Law M, Zagzag D, Grossman RI. Diffusion-tensor MR imaging of intracranial neoplasia and associated peritumoral edema: introduction of the tumor infiltration index. *Radiology* 2004; **232**: 221-228 [PMID: 15220505 DOI: 10.1148/radiol.2321030653]

30 **Chenevert TL**, Brunberg JA, Pipe JG. Anisotropic diffusion in human white matter: demonstration with MR techniques in vivo. *Radiology* 1990; **177**: 401-405 [PMID: 2217776]
31 **Lu S**, Ahn D, Johnson G, Cha S. Peritumoral diffusion tensor imaging of high-grade gliomas and metastatic brain tumors. *AJNR Am J Neuroradiol* 2003; **24**: 937-941 [PMID: 12748097]
32 **Wieshmann UC**, Clark CA, Symms MR, Franconi F, Barker GJ, Shorvon SD. Reduced anisotropy of water diffusion in structural cerebral abnormalities demonstrated with diffusion tensor imaging. *Magn Reson Imaging* 1999; **17**: 1269-1274 [PMID: 10576712]
33 **Schmierer K**, Wheeler-Kingshott CA, Boulby PA, Scaravilli F, Altmann DR, Barker GJ, Tofts PS, Miller DH. Diffusion tensor imaging of post mortem multiple sclerosis brain. *Neuroimage* 2007; **35**: 467-477 [PMID: 17258908 DOI: 10.1016/j.neuroimage.2006.12.010]
34 **Stadlbauer A**, Ganslandt O, Buslei R, Hammen T, Gruber S, Moser E, Buchfelder M, Salomonowitz E, Nimsky C. Gliomas: histopathologic evaluation of changes in directionality and magnitude of water diffusion at diffusion-tensor MR imaging. *Radiology* 2006; **240**: 803-810 [PMID: 16926329 DOI: 10.1148/radiol.2403050937]
35 **Tsuchiya K**, Fujikawa A, Nakajima M, Honya K. Differentiation between solitary brain metastasis and high-grade glioma by diffusion tensor imaging. *Br J Radiol* 2005; **78**: 533-537 [PMID: 15900059 DOI: 10.1259/bjr/68749637]
36 **van Westen D**, Lätt J, Englund E, Brockstedt S, Larsson EM. Tumor extension in high-grade gliomas assessed with diffusion magnetic resonance imaging: values and lesion-to-brain ratios of apparent diffusion coefficient and fractional anisotropy. *Acta Radiol* 2006; **47**: 311-319 [PMID: 16613314]
37 **Price SJ**, Peña A, Burnet NG, Jena R, Green HA, Carpenter TA, Pickard JD, Gillard JH. Tissue signature characterisation of diffusion tensor abnormalities in cerebral gliomas. *Eur Radiol* 2004; **14**: 1909-1917 [PMID: 15221264 DOI: 10.1007/s00330-004-2381-6]
38 **Jones DK**. Studying connections in the living human brain with diffusion MRI. *Cortex* 2008; **44**: 936-952 [PMID: 18635164 DOI: 10.1016/j.cortex.2008.05.002]
39 **Brunberg JA**, Chenevert TL, McKeever PE, Ross DA, Junck LR, Muraszko KM, Dauser R, Pipe JG, Betley AT. In vivo MR determination of water diffusion coefficients and diffusion anisotropy: correlation with structural alteration in gliomas of the cerebral hemispheres. *AJNR Am J Neuroradiol* 1995; **16**: 361-371 [PMID: 7726086]

**P- Reviewer**: Chen F, Chu JP, Prakash N
**S- Editor**: Ji FF **L- Editor**: A **E- Editor**: Jiao XK

World Journal of Radiology

Submit a Manuscript: http://www.wjgnet.com/esps/
Help Desk: http://www.wjgnet.com/esps/helpdesk.aspx
DOI: 10.4329/wjr.v7.i11.415

*World J Radiol* 2015 November 28; 7(11): 415-420
ISSN 1949-8470 (online)


ORIGINAL ARTICLE

Observational Study

# Pancreatic trauma: The role of computed tomography for guiding therapeutic approach

Marco Moschetta, Michele Telegrafo, Valeria Malagnino, Laura Mappa, Amato A Stabile Ianora, Dario Dabbicco, Antonio Margari, Giuseppe Angelelli

Marco Moschetta, Michele Telegrafo, Valeria Malagnino, Laura Mappa, Amato A Stabile Ianora, Giuseppe Angelelli, Interdisciplinary Department of Medicine, Section of Diagnostic Imaging, University of Bari Medical School, 70124 Bari, Italy

Dario Dabbicco, Antonio Margari, Department of Emergency and Organ Transplantation, University of Bari Medical School, 70124 Bari, Italy

Author contributions: Moschetta M, Telegrafo M, Malagnino V, Mappa L, Stabile Ianora AA, Dabbicco D, Margari A and Angelelli G contributed to study conception and design; Moschetta M, Telegrafo M and Malagnino V contributed to data acquisition, data analysis and interpretation, and writing of article; Moschetta M, Telegrafo M, Malagnino V, Mappa L, Stabile Ianora AA, Dabbicco D, Margari A and Angelelli G contributed to editing, reviewing and final approval of article.

Institutional review board statement: The study was approved by the local ethical committee.

Informed consent statement: Written informed consent for CT examinations was obtained in all cases.

Conflict-of-interest statement: All authors have no conflict of interests nor financial or personal relationships regarding this paper.

Data sharing statement: Patient data and full dataset are available from the corresponding author. The presented data are anonymised without the risk of identification.



Correspondence to: Marco Moschetta, MD, Professor, Interdisciplinary Department of Medicine, Section of Diagnostic Imaging, University of Bari Medical School, Piazza Giulio Cesare 11, 70124 Bari, Italy. marco.moschetta@gmail.com
Telephone: +39-080-5478840
Fax: +39-080-5592911

Received: May 14, 2015
Peer-review started: May 19, 2015
First decision: June 24, 2015
Revised: September 10, 2015
Accepted: October 12, 2015
Article in press: October 13, 2015
Published online: November 28, 2015

## Abstract

**AIM:** To evaluate the role of computed tomography (CT) for diagnosing traumatic injuries of the pancreas and guiding the therapeutic approach.

**METHODS:** CT exams of 6740 patients admitted to our Emergency Department between May 2005 and January 2013 for abdominal trauma were retrospectively evaluated. Patients were identified through a search of our electronic archive system by using such terms as "pancreatic injury", "pancreatic contusion", "pancreatic laceration", "peri-pancreatic fluid", "pancreatic active bleeding". All CT examinations were performed before and after the intravenous injection of contrast material using a 16-slice multidetector row computed tomography scanner. The data sets were retrospectively analyzed by two radiologists in consensus searching for specific signs of pancreatic injury (parenchymal fracture and laceration, focal or diffuse pancreatic enlargement/edema, pancreatic hematoma, active bleeding, fluid between splenic vein and pancreas) and non-specific signs (inflammatory changes in peri-pancreatic fat and mesentery, fluid surrounding the superior mesenteric

artery, thickening of the left anterior renal fascia, pancreatic ductal dilatation, acute pseudocyst formation/peri-pancreatic fluid collection, fluid in the anterior and posterior pararenal spaces, fluid in transverse mesocolon and lesser sac, hemorrhage into peri-pancreatic fat, mesocolon and mesentery, extraperitoneal fluid, intra-peritoneal fluid).

**RESULTS:** One hundred and thirty-six/Six thousand seven hundred and forty (2%) patients showed CT signs of pancreatic trauma. Eight/one hundred and thirty-six (6%) patients underwent surgical treatment and the pancreatic injures were confirmed in all cases. Only in 6/8 patients treated with surgical approach, pancreatic duct damage was suggested in the radiological reports and surgically confirmed in all cases. In 128/136 (94%) patients who underwent non-operative treatment CT images showed pancreatic edema in 97 patients, hematoma in 31 patients, fluid between splenic vein and pancreas in 113 patients. Non-specific CT signs of pancreatic injuries were represented by peri-pancreatic fat stranding and mesentery fluid in 89% of cases, thickening of the left anterior renal fascia in 65%, pancreatic ductal dilatation in 18%, acute pseudocyst/peri-pancreatic fluid collection in 57%, fluid in the pararenal spaces in 45%, fluid in transverse mesocolon and lesser sac in 29%, hemorrhage into peri-pancreatic fat, mesocolon and mesentery in 66%, extraperitoneal fluid in 66%, intra-peritoneal fluid in 41% cases.

**CONCLUSION:** CT represents an accurate tool for diagnosing pancreatic trauma, provides useful information to plan therapeutic approach with a detection rate of 75% for recognizing ductal lesions.

**Key words:** Trauma; Pancreas; Computed tomography; Imaging



**Core tip:** Pancreatic trauma is associated with high morbidity and mortality especially in case of delayed diagnosis. Computed tomography (CT) represents an accurate imaging tool for recognizing direct and indirect signs of pancreatic trauma and provides useful information to plan therapeutic approach. Among the specific signs, the presence of fluid between the splenic vein and the pancreas represents the most common CT finding suggesting pancreatic injury and the potential of CT for detecting ductal lesions have improved as compared to previous studies, with a 75% detection rate.

Moschetta M, Telegrafo M, Malagnino V, Mappa L, Stabile Ianora AA, Dabbicco D, Margari A, Angelelli G. Pancreatic trauma: The role of computed tomography for guiding therapeutic approach. *World J Radiol* 2015; 7(11): 415-420 Available from: URL: http://www.wjgnet.com/1949-8470/full/v7/i11/415.htm DOI: http://dx.doi.org/10.4329/wjr.v7.i11.415

## INTRODUCTION

Pancreatic trauma incidence ranges between 0.2% and 12% and occurs mainly in penetrating injuries with higher prevalence in children and young adults[1,2]. In case of blunt trauma, it is due to the impact of the organ against the adjacent vertebral column being the pancreatic body most commonly involved[3-5].

In 90% of cases, pancreatic lesions are associated with traumatic injuries of other abdominal organs as liver, spleen, stomach and duodenum[1,2].

Pancreatic trauma is associated with high morbidity and mortality especially in case of delayed diagnosis. In fact, the mortality ranges between 10% and 30% and is due to hemorrhagic lesions of the portal vein, splenic vein and inferior vena cava[1,6-20]. The reported morbidity rate is about 30% and mainly associated with pancreatic duct damage, consisting of fistulas, recurrent pancreatitis, pseudocysts, abscess, blood collections, retroperitoneal bleeding and ductal stenosis[6]. The diagnosis of early as late complications greatly increases the mortality rate which is mainly due to sepsis and multi-organ failure[6]. Clinical symptoms and signs of pancreatic injuries are nonspecific and include fever, leukocytosis, and elevated serum amylase or lipase levels.

Computed tomography (CT) represents the imaging technique of choice in hemodynamically stable patients with abdominal trauma, with reported sensitivity and specificity values as high as 80% in detecting pancreatic injuries being able to establish the type and grading of the detected lesions[8-14].

This study aims to evaluate the role of CT for diagnosing pancreatic injuries and guiding the choice of the therapeutic approach.

## MATERIALS AND METHODS

### *Patients*

CT exams of 6740 patients admitted to our Emergency Department between May 2005 and January 2013 for abdominal trauma were retrospectively evaluated. Patients were identified through a search of our electronic archive system by using such terms as "pancreatic injury", "pancreatic contusion", "pancreatic laceration", "peri-pancreatic fluid", "pancreatic active bleeding". The mean time between abdominal trauma and CT examination was about 1-2 h.

### *CT protocol*

All patients were examined in an emergency setting. The CT scanner used was a 16-slice multidetector row CT (TSX - 101A - Aquilion 16, Toshiba Medical System, Tokyo, Japan). In all cases, scans were acquired before and after the intravenous injection of contrast material (120-140 mL injected at a rate of 3-3.5 mL/s), with image acquisition in the arterial phase, generally with a delay of 30-40 s from the beginning of contrast administration, in the portal venous phase, with a delay

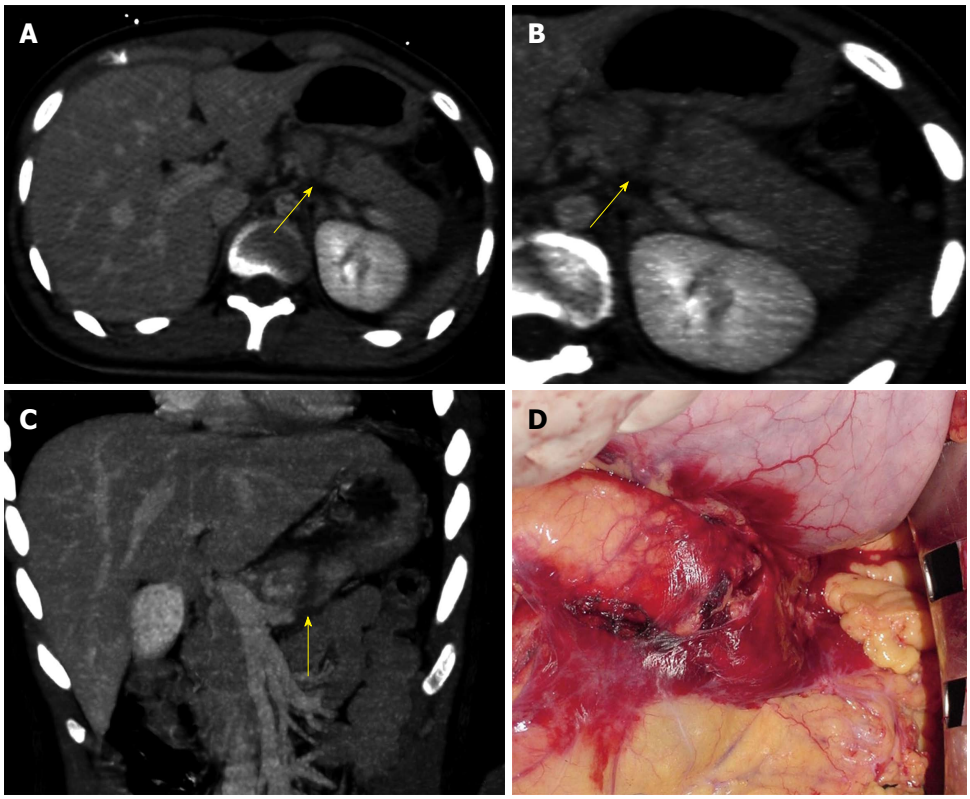


**Figure 1 Computed tomography and intra-operative findings of pancreatic parenchymal fracture.** A: CT image on axial plan showing a complete laceration of the pancreatic body appearing as a low-attenuation line oriented perpendicular to the long axis of the pancreas (arrow); B: CT image on axial plan showing a complete laceration of the pancreatic body appearing as a low-attenuation line oriented perpendicular to the long axis of the pancreas (arrow); C: CT image on coronal plan showing a complete laceration of the pancreatic body appearing as a low-attenuation line oriented perpendicular to the long axis of the pancreas (arrow); D: Intra-operative finding confirming the CT diagnosis of post-traumatic laceration of the pancreas. CT: Computed tomography.

of 60-90 s from the beginning of contrast-agent administration and in delayed phase with a delay of 120-180 s from the beginning of contrast-agent administration[21].

### *Image interpretation*

The data sets were retrospectively analyzed on a workstation (HP XW 6400) equipped with image reconstruction software (Vitrea 4.0, Vital Images, Minneapolis, MN, United States). Multi-planar, Maximum Intensity Projection and Minimum Intensity Projection reconstructions were used.

Two radiologists in consensus assessed all images. Post-processing duration time was approximately 15 min.

CT images were evaluated searching for specific signs of pancreatic injury: parenchymal fracture; laceration; pancreatic edema; hematoma; active bleeding; and fluid between splenic vein and pancreas.

On the other side, non-specific signs were also assessed: peri-pancreatic fat or mesentery stranding; mesenteric fluid; thickening of the left anterior renal fascia; pancreatic ductal dilatation; acute peri-pancreatic fluid collection; fluid in the pararenal spaces; fluid in transverse mesocolon and lesser sac; hemorrhage into peri-pancreatic fat, mesocolon and mesentery; extraperitoneal fluid; and intra-peritoneal fluid[9,22]. Associated injuries to adjacent structures were also evaluated.

## RESULTS

On the basis of CT findings, 136 out 6740 (2%) patients showed signs of traumatic injuries of the pancreas. In this group of patients, 90 patients were male and 46 were female with an average age of 45.4 ± 16.1 years (range: from 30 to 65 years old). Mechanism of injury was blunt motor vehicle collision in 70 patients, bicycle injury in 33, direct blow to the abdomen in 20, falls in 9 cases and sport related injury in 4 patients.

Eight out of 136 (6%) patients underwent surgical treatment within 8-12 h from the diagnosis and the pancreatic injures were confirmed in all cases, represented by 3 cases of parenchymal fracture (Figure 1) and 5 of extensive lacerations. Pancreatic injuries involved the conjunction between the neck and the body of the pancreas in 4 cases. Three patients had pancreatic body injuries and one had pancreatic tail injury. A complete pancreatic fracture line was identified on CT images in all patients and was identified as a linear discontinuity of the glandular parenchyma extending from the anterior to the posterior surface.

In all patients, fluid between splenic vein and pancreas was found.

In 6 out 8 patients treated with surgical approach, pancreatic duct damage was suggested in the radiological reports and surgically confirmed in all cases. In the remaining 2 patients, CT did not suggest a ductal injury

but it was surgically detected.

One hundred and twenty-eight out of 136 (94%) patients underwent non-operative treatment and follow-up CT examination showed a resolution of the pathological findings. CT images showed pancreatic edema in 97 patients, hematoma in 31 patients, fluid between splenic vein and pancreas in 113 patients.

As regard with non-specific CT signs of pancreatic injuries, peri-pancreatic fat stranding and mesenteric fluid occurred in 122 out of 136 (89%) cases, thickening of the left anterior renal fascia in 88 out of 136 (65%), pancreatic ductal dilatation in 25 out of 136 (18%), acute pseudocyst/peri-pancreatic fluid collection in 78 out of 136 (57%), fluid in the pararenal spaces in 61 out of 136 (45%), fluid in transverse mesocolon and lesser sac in 40 out of 136 (29%), hemorrhage into peri-pancreatic fat, mesocolon and mesentery in 90 out of 136 (66%), extraperitoneal fluid in 90 out of 136 (66%), intra-peritoneal fluid in 56 out of 136 (41%) cases.

With regard to associated injuries to adjacent structures, in 27 out of 136 patients (20%) CT detected also extra-pancreatic findings represented by vertebral fracture ($n$ = 11), liver contusion ($n$ = 6), spleen contusion ($n$ = 4), right kidney contusion ($n$ = 3), small bowel injury ($n$ = 2), left kidney contusion ($n$ = 1).

## DISCUSSION

CT represents the gold standard imaging technique for evaluating pancreatic trauma. Variable sensitivity and specificity values have been reported in the medical literature with an overall sensitivity in detecting all grades of pancreatic lesions of about 80%[9]. The specific CT findings of pancreatic injury are represented by parenchymal contusion, laceration, hematoma, active extravasation of contrast medium and fracture. Contusions are defined as areas of diminished density without discontinuity at the surface of the gland, lacerations as low-attenuation lines perpendicular to the long axis of the pancreas and fractures as clear separations of parenchymal fragments[9-11].

In our series specific CT signs of pancreatic trauma have been detected in all cases with the presence of fluid between the splenic vein and the pancreas being the most common and sensitive sign.

Lane *et al*[12] reported that fluid between the splenic vein and the pancreas allows to identify a pancreatic trauma and it is detected in 90% of cases of pancreatic injury.

This data is also confirmed in our series. In fact, fluid between the splenic vein and the pancreas occurred in all cases treated with surgical approach and in 88% of patients treated conservatively, with an overall rate of 89% in our series.

On the other side, peri-pancreatic fat stranding, peri-pancreatic fluid collections represent the most common indirect CT signs of pancreatic trauma occurring in the 89% of cases in our series[9-11].

The American Association for the Surgery of Trauma proposed a grading system mainly based on the site of pancreatic trauma and the integrity of the main pancreatic duct. In fact, a CT grading system has been established for supporting the surgical classification[9,12-15]. Therefore, CT allows to establish a grading of pancreatic injuries by providing important information for management of the gland lesions. Grade Ⅰ lesions include minor contusions or lacerations with no duct injury (less than 50% of the thickness pancreatic), Grade Ⅱ major contusions or lacerations with no duct injury, Grade Ⅲ transections or major lacerations with duct disruption in distal pancreas, Grade Ⅳ transections of proximal pancreas or major lacerations with associated injury to the ampulla of Vater, Grade Ⅴ massive disruption of the pancreatic head. The lesions involving the pancreatic head have a mortality rate almost double (28%) as compared to the tail injuries (16%), because of the inferior vena cava, inferior mesenteric vein and portal vein involvement[9,10,12-17].

Moreover, the most important prognostic factor is the destruction of the pancreatic duct which requires surgical or endoscopic treatment while the lesions which do not involve pancreatic duct can be treated by conservative treatment[16,17]. The rupture of the pancreatic duct is reported to be poorly detectable with CT, even if parenchymal laceration affecting more than 50% of the thickness of the gland are associated with high risk of pancreatic duct damage[18,19,23-25].

In fact, the main limitations of CT reported in the medical literature are represented by a low accuracy in detecting major ductal lesions which is reported to be about 43% and the underestimation of pancreatic injuries, especially in the first 12 h after the traumatic event. For this reason, a second CT examination is required within 24-48 h after admission in suspected pancreatic lesions in case of negative first CT[1,9,13].

In fact, in patients with suspected pancreatic duct lesion magnetic resonance cholangiopancreatography (MRCP) or endoscopic retrograde colangiopancreatography (ERCP) are strongly suggested. The MRCP represents the gold standard in this cases and it is reported to have diagnostic accuracy of 100% for evaluating to evaluate pancreatic duct damage[8]. However, ERCP allows direct imaging guided treatments. In fact, ERCP can guide surgical repair or can be used for stent placement. Many studies showed that mild pancreatic duct injuries may be treated with stent placement rather than surgical repair[19,20,23,24].

In our series, CT detected a ductal injury in 75% of cases. This value seems to be higher than the one reported in the literature; however, further studies in this field with a larger number of enrolled patients are required in order to confirm this data.

Our study presents some limitations represented by the limited number of patient with pancreatic injuries and the related impossibility to apply statistical tests to evaluate our data; the absence of repeated CT examinations in our series in case of negative first CT

examination; the absence of MRI or ERCP evaluation in patient treated with conservative approach confirming pancreatic duct integrity; the lack of an inter-observer agreement evaluation; the retrospective type of the study and the lack of morbidity or mortality data in the current series.

In conclusion, CT represents an accurate imaging tool for recognizing direct and indirect signs of pancreatic trauma and provides useful information to plan therapeutic approach. Among the specific signs, the presence of fluid between the splenic vein and the pancreas represents the most common CT finding suggesting pancreatic injury and the potential of CT for detecting ductal lesions have improved as compared to previous studies, with a 75% detection rate.

## COMMENTS

### Background

Pancreatic trauma incidence ranges between 0.2% and 12% and is associated with high morbidity and mortality especially in case of delayed diagnosis. Computed tomography (CT) represents the imaging technique of choice in hemodynamically stable patients with abdominal trauma with reported sensitivity and specificity values as high as 80% in detecting pancreatic injuries being able to establish the type and grading of the detected lesions.

### Research frontiers

The increasing trend of non-operative management, especially in blunt trauma and stable patients, and the consequences of delayed or missed diagnosis makes CT the imaging modality of choice for evaluating pancreatic lesions.

### Innovations and breakthroughs

CT represents an accurate imaging tool for recognizing direct and indirect signs of pancreatic trauma and provides useful information to plan therapeutic approach. The potential of CT for detecting ductal lesions have improved as compared to previous studies, with a 75% detection rate.

### Applications

CT allows the radiologist to recognize all findings suggestive of severe pancreatic injury and also to detect the main alterations suitable for surgical approach. Therefore, a diagnostic and prognostic role can be given to this imaging tool.

### Peer-review

This a very interesting study about the role of CT for diagnosis of pancreatic trauma, and as we know, pancreatic trauma is associated with high morbidity and mortality especially in case of delayed diagnosis. According to the result of this study, CT represents an accurate imaging tool for recognizing direct and indirect signs of pancreatic trauma, and provides useful information to plan therapeutic approach.

## REFERENCES


1 **Gupta A**, Stuhlfaut JW, Fleming KW, Lucey BC, Soto JA. Blunt trauma of the pancreas and biliary tract: a multimodality imaging approach to diagnosis. *Radiographics* 2004; **24**: 1381-1395 [PMID: 15371615]

2 **Holalkere NS**, Soto J. Imaging of miscellaneous pancreatic pathology (trauma, transplant, infections, and deposition). *Radiol Clin North Am* 2012; **50**: 515-528 [PMID: 22560695 DOI: 10.1016/j.rcl.2012.03.011]

3 **Boffard KD**, Brooks AJ. Pancreatic trauma--injuries to the pancreas and pancreatic duct. *Eur J Surg* 2000; **166**: 4-12 [PMID: 10688209]

4 **Rekhi S**, Anderson SW, Rhea JT, Soto JA. Imaging of blunt pancreatic trauma. *Emerg Radiol* 2010; **17**: 13-19 [PMID: 19396480 DOI: 10.1007/s10140-009-0811-0]

5 **Madiba TE**, Mokoena TR. Favourable prognosis after surgical drainage of gunshot, stab or blunt trauma of the pancreas. *Br J Surg* 1995; **82**: 1236-1239 [PMID: 7552005 DOI: 10.1002/bjs.1800820926]

6 **Bradley EL**, Young PR, Chang MC, Allen JE, Baker CC, Meredith W, Reed L, Thomason M. Diagnosis and initial management of blunt pancreatic trauma: guidelines from a multiinstitutional review. *Ann Surg* 1998; **227**: 861-869 [PMID: 9637549 DOI: 10.1097/00000658-199806000-00009]

7 **Dawson AR**, Webster CH, Howe HC, Theron EJ, Meiring L. Rupture of the head of the pancreas by blunt trauma. A case report. *S Afr Med J* 1985; **67**: 560-562 [PMID: 3992386]

8 **Wong YC**, Wang LJ, Fang JF, Lin BC, Ng CJ, Chen RJ. Multidetector-row computed tomography (CT) of blunt pancreatic injuries: can contrast-enhanced multiphasic CT detect pancreatic duct injuries? *J Trauma* 2008; **64**: 666-672 [PMID: 18332806 DOI: 10.1097/ta.0b013e31802c5ba0]

9 **Venkatesh SK**, Wan JM. CT of blunt pancreatic trauma: a pictorial essay. *Eur J Radiol* 2008; **67**: 311-320 [PMID: 17709222 DOI: 10.1016/j.ejrad.2007.07.003]

10 **Phelan HA**, Velmahos GC, Jurkovich GJ, Friese RS, Minei JP, Menaker JA, Philp A, Evans HL, Gunn ML, Eastman AL, Rowell SE, Allison CE, Barbosa RL, Norwood SH, Tabbara M, Dente CJ, Carrick MM, Wall MJ, Feeney J, O'Neill PJ, Srinivas G, Brown CV, Reifsnyder AC, Hassan MO, Albert S, Pascual JL, Strong M, Moore FO, Spain DA, Purtill MA, Edwards B, Strauss J, Durham RM, Duchesne JC, Greiffenstein P, Cothren CC. An evaluation of multidetector computed tomography in detecting pancreatic injury: results of a multicenter AAST study. *J Trauma* 2009; **66**: 641-646; discussion 646-647 [PMID: 19276732 DOI: 10.1097/ta.0b013e3181991a0e]

11 **Lee WJ**, Foo NP, Lin HJ, Huang YC, Chen KT. The efficacy of four-slice helical CT in evaluating pancreatic trauma: a single institution experience. *J Trauma Manag Outcomes* 2011; **5**: 1 [PMID: 21214900 DOI: 10.1186/1752-2897-5-1]

12 **Lane MJ**, Mindelzun RE, Sandhu JS, McCormick VD, Jeffrey RB. CT diagnosis of blunt pancreatic trauma: importance of detecting fluid between the pancreas and the splenic vein. *AJR Am J Roentgenol* 1994; **163**: 833-835 [PMID: 7503824 DOI: 10.2214/ajr.163.4.7503824]

13 **Teh SH**, Sheppard BC, Mullins RJ, Schreiber MA, Mayberry JC. Diagnosis and management of blunt pancreatic ductal injury in the era of high-resolution computed axial tomography. *Am J Surg* 2007; **193**: 641-643; discussion 643 [PMID: 17434373 DOI: 10.1016/j.amjsurg.2006.12.024]

14 **Lahiri R**, Bhattacharya S. Pancreatic trauma. *Ann R Coll Surg Engl* 2013; **95**: 241-245 [PMID: 23676806 DOI: 10.1308/003588413X13629960045913]

15 **Brandon JC**, Fields PA, Evankovich C, Wilson G, Teplick SK. Pancreatic clefts by penetrating vessels: a potential diagnostic for pancreatic fracture on CT. *Emerg Radiol* 2000; **7**: 283-286 [DOI: 10.1007/pl00011842]

16 **Degiannis E**, Levy RD, Velmahos GC, Potokar T, Florizoone MG, Saadia R. Gunshot injuries of the head of the pancreas: conservative approach. *World J Surg* 1996; **20**: 68-71; discussion 72 [PMID: 8588416 DOI: 10.1007/s002689900012]

17 **Lewis G**, Krige JE, Bornman PC, Terblanche J. Traumatic pancreatic pseudocysts. *Br J Surg* 1993; **80**: 89-93 [PMID: 8428304 DOI: 10.1002/bjs.1800800129]

18 **Wong YC**, Wang LJ, Lin BC, Chen CJ, Lim KE, Chen RJ. CT grading of blunt pancreatic injuries: prediction of ductal disruption and surgical correlation. *J Comput Assist Tomogr* 1997; **21**: 246-250 [PMID: 9071293 DOI: 10.1097/00004728-199703000-00014]

19 **Linsenmaier U**, Wirth S, Reiser M, Körner M. Diagnosis and classification of pancreatic and duodenal injuries in emergency radiology. *Radiographics* 2008; **28**: 1591-1602 [PMID: 18936023 DOI: 10.1148/rg.286085524]

20 **Yang L**, Zhang XM, Xu XX, Tang W, Xiao B, Zeng NL. MR

imaging for blunt pancreatic injury. *Eur J Radiol* 2010; **75**: e97-101 [PMID: 20056369 DOI: 10.1016/j.ejrad.2009.12.017]

21 **Moschetta M**, Stabile Ianora AA, Pedote P, Scardapane A, Angelelli G. Prognostic value of multidetector computed tomography in bowel infarction. *Radiol Med* 2009; **114**: 780-791 [PMID: 19551344 DOI: 10.1007/s11547-009-0422-6]

22 **Daly KP**, Ho CP, Persson DL, Gay SB. Traumatic Retroperitoneal Injuries: Review of Multidetector CT Findings. *Radiographics* 2008; **28**: 1571-1590 [PMID: 18936022 DOI: 10.1148/rg.286075141]

23 **Soto JA**, Alvarez O, Múnera F, Yepes NL, Sepúlveda ME, Pérez JM. Traumatic disruption of the pancreatic duct: diagnosis with MR pancreatography. *AJR Am J Roentgenol* 2001; **176**: 175-178 [PMID: 11133562 DOI: 10.2214/ajr.176.1.1760175]

24 **Chinnery GE**, Krige JE, Kotze UK, Navsaria P, Nicol A. Surgical management and outcome of civilian gunshot injuries to the pancreas. *Br J Surg* 2012; **99** Suppl 1: 140-148 [PMID: 22441869]

25 **Körner M**, Krötz MM, Degenhart C, Pfeifer KJ, Reiser MF, Linsenmaier U. Current Role of Emergency US in Patients with Major Trauma. *Radiographics* 2008; **28**: 225-242 [PMID: 18203940 DOI: 10.1148/rg.281075047]

**P- Reviewer**: Chen F, Fu DL, Kozarek R, Sureka B
**S- Editor**: Ji FF **L- Editor**: A **E- Editor**: Jiao XK

Published by **Baishideng Publishing Group Inc**
8226 Regency Drive, Pleasanton, CA 94588, USA
Telephone: +1-925-223-8242
Fax: +1-925-223-8243
E-mail: bpgoffice@wjgnet.com
Help Desk: http://www.wjgnet.com/esps/helpdesk.aspx
http://www.wjgnet.com